UNIVERSITÀ DEGLI STUDI DI TRIESTE

XXIV CICLO
DEL DOTTORATO DI RICERCA IN
FISICA

Measurement of two-hadron transverse spin asymmetries in SIDIS at COMPASS

Settore scientifico-disciplinare
FISICA NUCLEARE E SUBNUCLEARE (FIS/04)

Dottorando
Carmine Elia

Responsabile Dottorato di Ricerca
prof. Paolo Camerini

Relatore
prof.ssa Anna Martin, Università Degli Studi di Trieste

Tutore
prof.ssa Anna Martin, Università Degli Studi di Trieste

ANNO ACCADEMICO 2010/2011

Contents

Chapter 1

Introduction

The discovery, in 1897, by J.J. Thomson that atoms contain negatively charged electrons whose mass is only about 1/2000 the hydrogen atom mass represents the first evidence of a subatomic structure of matter. In his *plum pudding* model Thomson supposed that the electrons were embedded in a positively charged lump of matter. In 1910, Rutherford realized that the positive electric charge, in an atom, is confined to an area far smaller than the atom itself: the nucleus. In 1919 Rutherford discovered that nuclei contain discrete units of positive charge: the proton. The hypothesis that the nucleus was made only by protons was in contradiction with the observation that the nucleus mass was about twice that due to the protons needed to provide the positive charge. This contradiction was overcome by the discovery of the neutron, a new particle with the same mass of the protons but with neutral charge. Chadwick observed for the first time the neutrons at Cambridge, in 1932. When particles of high energy have been available at the accelerators, new prospects have been opened in the study of the nuclear particles. Electrons with a wavelength comparable with the nucleus radius were first produced in 1953 at Stanford University. From then on the nucleus is not viewed any more as a point-like object. Hofstadter and colleagues studying scattering of electrons from single proton found that also the proton is not a point-like object, but has a size about 0.75×10^{-13} cm and that high energy electrons would scatter from the protons within a larger nucleus, i.e. the electrons could "see" the protons inside the nucleus.

If we can use electrons to "see" protons inside the nucleus, can we also use them to see inside protons?

The availability of beams with higher energy allowed to investigate the structure of the protons by Deep Inelastic Scattering (DIS). The pioneering DIS experiment has been done at Stanford Accelerator Center (SLAC) in 1967. One of the purposes of the experiment was to investigate the inelastic scattering in a kinematic region until then unexplored. Two unexpected features were found. The first one was that the deep inelastic cross sections decreased weakly with increasing four-momentum transfer q as shown in fig.1.1. The second surprising feature in the data was the so called "scaling" behaviour.

When the scaling was observed at SLAC the reason of this feature was not clear and many models were proposed to explain it and the weak dependence of the cross section on q^2. The scaling behaviour can be explained considering the differential cross section for unpolarized electrons scattering from unpolarized nucleons:

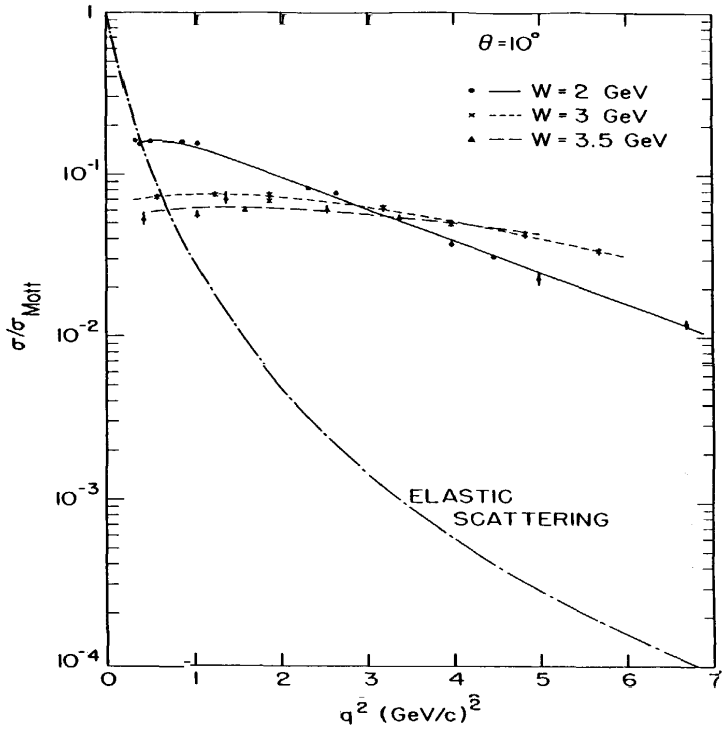

Figure 1.1: The σ/σ_{Mott} ratio versus q^2 is shown for elastic scattering and for inelastic cross-section for W=2,3 and 3.5 GeV/c^2. It's evident the different q^2 dependence in the two case.

$$\frac{d^2\sigma}{d\Omega dE'} = \sigma_{Mott}[W_2 + 2W_1 \tan^2 \frac{\theta}{2}] \tag{1.1}$$

the functions W_1 and W_2 are each expected to depend on q^2 and on the energy loss of the electron ν. In 1968 Bjorken, on the basis of the current algebra, hypothesized that, in the asymptotic limit for q^2 and ν, the structure functions W_1 and W_2 would become functions only of the quantity $x = q^2/2\mathrm{M}\nu$ [1]. This result implied the existence of point-like constituents of hadrons. A similar hypothesis was proposed also by Feynman to explain the scaling feature in his parton model. In this model the nucleon is composed by a collection of free point-like constituents: the partons. At the time, however, it was not yet clear that there were reasonable candidates for the constituents: the quarks theorized by Gell-Mann and Zweig in 1964. In the following years, after the SLAC experiments, many experiments were done to understand the structure of the nucleons and in particular to investigate the origin of the spin of the nucleons.

The quark spin contribution to the nucleon spin has been measured, for the first time, in the early 70's in the Yale-SLAC E-80 experiment [2]. In this DIS experiment, the first with longitudinally polarized beam and target, the $\Delta q(x)$ distribution function, usually called the helicity distribution function has been measured. In the hypothesis in which the nucleon is moving with a very large momentum (infinite momentum frame) and with spin oriented longitudinally to its motion, the helicity distribution is given by

$$\Delta q(x) = \sum_q e_q^2 \left[q^{\uparrow}(x) - q^{\downarrow}(x) \right] \tag{1.2}$$

where e_q is the charge and $q^{\uparrow}$ and $q^{\downarrow}$ are the densities of quarks and antiquarks of a given flavour q with spin parallel and anti-parallel to the nucleon spin; the helicity measures the longitudinal spin of the quarks in the nucleons. In this first Yale-SLAC experiment the results were compatible with the hypothesis that the spin of the nucleon were essentially carried by the u and d quarks. However, a major breakthrough in this field occurred in 1988, when the EMC collaboration [3] found that the contribution of the quarks to the spin of the proton is rather smaller, even compatible with zero. The result obtained in this experiment and confirmed with much higher precision by others DIS experiments with both proton and neutron targets [4] is in contradiction with the naive hypothesis that the nucleon spin is completely due to the quark spin ($\Delta\Sigma = \Delta u + \Delta d + \Delta s = 1$).

Today it's known that the quark helicity accounts for only the 30 % of the nucleon spin. The others contributions which can provide the missing spin are the contributions of the gluons (ΔG), and the contributions of the orbital angular momentum of the quarks (L_q) and gluons (L_g)

$$N_{spin} = \frac{1}{2}\Delta\Sigma + \Delta G + L_q + L_g. \tag{1.3}$$

The contribution ΔG, recently directly measured by the COMPASS experiment [5], turned out to be very small, compatible with zero, leaving room to the contribution due to the orbital angular momentum which is now the goal of several future experiments.

One must add, however, that the unpolarized and the helicity distributions do not exhaust the description of the nucleon structure. At leading twist, a third parton distribution, the transversity distribution, exists, and is different from the other two. It was in 1979 that the transversity distribution function was first introduced by Ralston and Soper [6] to describe the probability of finding a quark with polarization parallel or anti-parallel to the spin of the transversely polarized parent nucleon. Only in the 90's a new generation of proposed experiments included the study of the transverse spin-structure of the nucleon in their experimental programs and COMPASS was one of these.

In this thesis the measurement of the transversity distribution function from deep inelastic scattering of a lepton off a transversely polarized target will be discussed. Data with a transversely polarized deuteron target were collected in COMPASS in the year 2002-2004. The first data with a transversely polarized proton target were taken in 2007. The work done for this thesis manly concerns the data collected with transversely polarized protons in 2010, when the complete data taking was dedicated to the measurement of transverse spin effects.

In chapter 2 the inclusive and semi-inclusive deep inelastic scattering (SIDIS) and the theoretical motivations on which the transversity distribution function measurement is based are discussed.

In chapter 3 it is described how to access transversity from the measurement of azimuthal asymmetries in one-hadron and hadron pair production. The previous

measurements of transverse spin effects, transversity measurement and a general experimental overview are given in the last section of this chapter. The COMPASS experiment is described in chapter 4. The first sections are dedicated to the description of the COMPASS polarized target, the tracking detectors and the particle identification detectors. The data acquisition system, the off-line system and the event reconstruction are discussed in the last sections.

The analysis of the data collected in 2010 is discussed in chapter 5. The selection of SIDIS events is described in the first part of the chapter, while the second part of the chapter is dedicated to the description of the tests performed to evaluate the data quality and reject the "bad data". The methods used to measure the asymmetries and the tests performed to evaluate the systematic effects are described in the last part of the chapter. In chapter 6 the results obtained from the 2010 data are given. The results are compared with the previous results and with the theoretical predictions and a first extraction of the transversity distribution function from two-hadron asymmetries is described. In the last part of the chapter the results for z-ordered hadrons and identified particles are presented. The conclusion and outlook are given in chapter 7.

Chapter 2

Deep inelastic scattering and the transversity distribution

In the following sections we will consider first the inclusive DIS in which only the scattered lepton is detected and then the semi-inclusive DIS in which at least one hadron in the final state is detected, both on unpolarized and polarized targets. The present theoretical description of this iterations in terms of the new functions, transversity and transverse momentum dependent (TMD) parton distribution functions, will be discussed.

2.1 Inclusive deep inelastic scattering

The DIS diagram is illustrated in fig. 2.1. In DIS, at leading order in α_s, a lepton with four-momentum l exchanges a virtual photon with four-momentum q with a nucleon with four-momentum P and mass M; l' is the four-momentum of the scattered lepton and W is the invariant mass of the undetected hadronic system X. The spin of the nucleon is given by the four-vector S with $S^2 = -1$ and $P \cdot S = 0$.

The invariants and the variables used to describe the DIS reaction are summarized in Table 2.1. In the following we will assume $Q^2, P \cdot q >> M^2$ (DIS regime). In a generic frame in which the virtual photon direction is parallel to the z axis, P and q can be parametrized in light-cone coordinates (see appendix A) as:

$$\begin{aligned} P^\mu &= \left[P^+, \frac{M^2}{2P^+}, \mathbf{0}_T \right], \\ q^\mu &= \left[-x_B P^+, \frac{Q^2}{2x_B P^+}, \mathbf{0}_T \right]. \end{aligned} \tag{2.1}$$

The cross-section for longitudinally polarized lepton-nucleon scattering can be obtained by the contraction between a leptonic tensor and a hadronic tensor [7, 8, 9]. The leptonic tensor is described by QED and is given by

$$L_{\mu\nu} = \frac{1}{2}\overline{u}(l')\gamma_\mu u(l)\overline{u}(l')\gamma_\nu u(l) = 2\{l_\mu l'_\nu + l'_\mu l_\nu - g_{\mu\nu}(l \cdot l')\} + 2i\lambda_l\{\epsilon_{\mu\nu\lambda\sigma} l^\lambda l'^\sigma\} \tag{2.2}$$

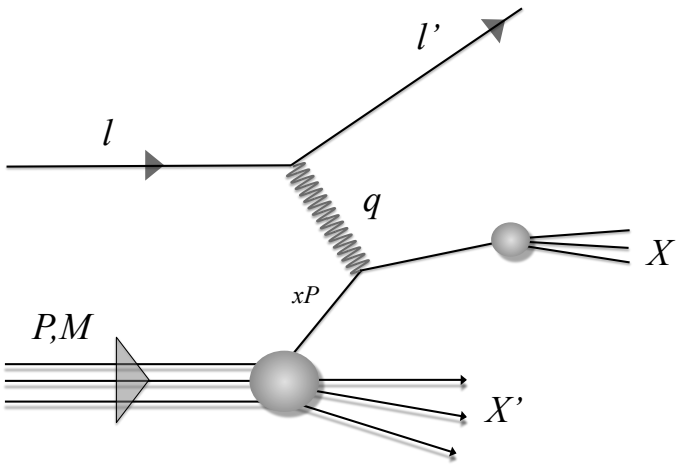

Figure 2.1: Diagram of the inclusive deep inelastic scattering.

Table 2.1: DIS kinematical variables.

Denomination	*Definition*	*Nucleon rest frame*	*Description*
ϑ			lepton scattering angle
ν	$(P \cdot q)/M$	$E - E'$	lepton's energy loss
q	$l - l'$		four-momentum transfer to the target
Q^2	$-q^2$	$\sim 4EE'sin(\vartheta)$	squared momentum transfer
x	$Q^2/(2P \cdot q)$	$Q^2/(2M\nu)$	Bjorken scaling variable
y	$(2P \cdot q)/(P \cdot l)$	ν/E	fractional energy transfer to the nucleon

where λ_l is the lepton polarization.

The hadronic tensor is given by

$$2MW^{\mu\nu}(q,P,S) = \frac{1}{2\pi}\sum_X \int \frac{d^3P_X}{(2\pi)^3 2P_X^0}(2\pi)^4\delta^4(q+P-P_X) \times \langle P,S|J^\mu(0)|X\rangle\langle X|J^\nu(0)|P,S\rangle. \tag{2.3}$$

In this formula P_X represents the total four-momentum of the final state X. In inclusive DIS the final state is undetected so integrating on it in eq. 2.3, Fourier trasforming the delta function and translating one of the current operators one obtains:

$$2MW^{\mu\nu}(q,P,S) = \frac{1}{2\pi}\int d^4\xi e^{iq\cdot\xi}\langle P,S|J^\mu(\xi)J^\nu(0)|P,S\rangle. \tag{2.4}$$

A further specification of the structure of the hadronic tensor requires an understanding of its inner dynamics. However at sufficiently high Q^2 the DIS reaction can be considered as a scattering of a lepton off a free quark. In the QCD-parton model this process can be represented by the so-called handbag diagram shown in fig. 2.2. In this case we can split the final state in a quark with four-momentum k and mass m and a state X' with four-momentum $P_{X'}$. The hadronic tensor becomes

$$2MW^{\mu\nu}(q,P,S) = \frac{1}{2\pi}\sum_q e_q^2 \sum_{X'} \int \frac{d^3P_{X'}}{(2\pi)^3 2P^0_{X'}} \int \frac{d^3k}{(2\pi)^3 2k}(2\pi)^4\delta^4(q+P-k-P_{X'}) \times\left(\langle P,S|\overline{\Psi}_i(0)|X'\rangle\langle X'|\Psi_j(0)|P,S\rangle\gamma^\mu_{ik}(\not{k}+m)_{kl}\gamma^\nu_{lj}\right). \tag{2.5}$$

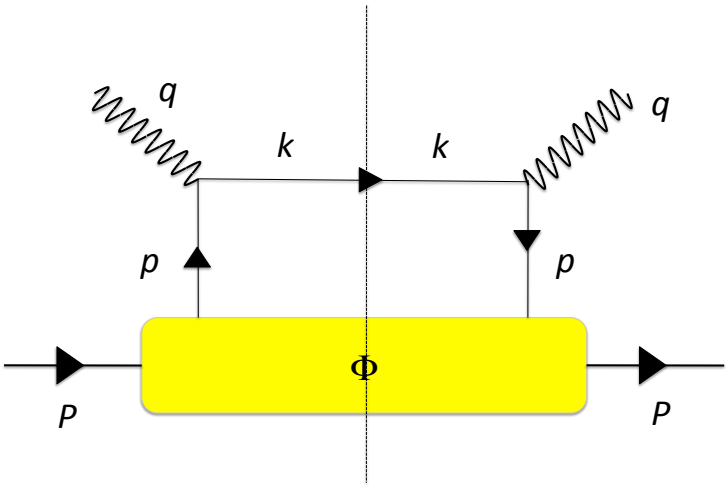

Figure 2.2: handbag diagram of the inclusive deep inelastic scattering.

The sum is extended to all the quark and antiquark flavours. Defining the four-vector $p = k - q$ and introducing the quark-quark correlation function Φ, the hadronic tensor can be written in the compact way:

$$2MW^{\mu\nu}(q,P,S) = \sum_q e_q^2 \int d^4p\,\delta\left((p+q)^2 - m^2\right)\theta(p^0+q^0-m) \times Tr[\Phi^q_{ij}(p,P,S)\gamma^\mu_{ik}(\not{p}+\not{q}+m)_{kl}\gamma^\mu_{lj}], \tag{2.6}$$

where

$$\Phi^q_{ij}(p,P,S) = \frac{1}{(2\pi)^4}\int d^4\xi e^{-ip\cdot\xi}\langle P,S|\overline{\Psi}_i(\xi)\Psi_j(0)|P,S\rangle. \tag{2.7}$$

The four-momentum p can be parametrized as

$$p^\mu = \left[xP^+, \frac{p^2 + |\boldsymbol{p}_T|^2}{2xP^+}, \boldsymbol{p}_T \right], \tag{2.8}$$

where $x = p^+/P^+$. In a hard scale, making an expansion in orders of 1/Q, and neglecting the terms of $\mathcal{O}(1/Q^2)$, the parametrization used implies that the plus components, p^+, P^+, are $\sim Q$, while the minus components, p^-, P^-, are $\sim\ 1/Q$, so the nucleon momentum plus component play a dominant role and eq. 2.1 can be approximated as:

$$\begin{aligned} P^\mu &\approx \left[P^+, 0, \mathbf{0}_T \right], \\ q^\mu &\approx \left[0, \frac{M\nu}{P^+}, \mathbf{0}_T \right], \\ p^\mu &\approx \left[xP^+, 0, \mathbf{0}_T \right], \end{aligned} \tag{2.9}$$

and

$$\delta[(p+q)^2] = \delta(-Q^2 + 2xP\cdot q) = \frac{1}{2P\cdot q}\delta(x - x_B). \tag{2.10}$$

In these conditions x can be interpreted as the fraction of the total longitudinal momentum carried by the quark and the hadronic tensor can be approximated as

$$\begin{aligned} 2MW^{\mu\nu}(q,P,S) &\approx \sum_q e^{q^2} \int d^2p_T dp^- dx \frac{P^+}{2P\cdot q}\delta(x - x_B) Tr[\Phi_{ij}(p,P,S)\gamma^\mu(\not{p} + \not{q} + m)\gamma^\nu] \\ &= \sum_q e^{q^2} \frac{1}{2} Tr\left[\Phi_{ij}(x_B,S)\gamma^\mu \frac{P^+}{P\cdot q}(\not{p} + \not{q} + m)\gamma^\nu \right], \end{aligned} \tag{2.11}$$

where Φ_{ij} is the integrated correlation function:

$$\begin{aligned} \Phi_{ij}(x,S) &= \int d^2p_T dp^- \Phi_{ij}(p,P,S)\Big|_{p^+ = xP^+} \\ &= \int \frac{d\xi^-}{2\pi} e^{-ip\cdot\xi} \langle P,S|\overline{\Psi}_i(\xi)\Psi_j(0)|P,S\rangle\Big|_{\xi^+ = \boldsymbol{\xi}_T = 0}. \end{aligned} \tag{2.12}$$

The correlation function can be parametrized in terms of the Dirac matrices $(\mathbb{I}, \gamma^\mu, \gamma_5, \gamma^\mu\gamma_5, \sigma^{\mu\nu}, \sigma^{\mu\nu}\gamma_5)$ and can be expressed in the collinear approach and at leading order in the twist[1] expansion in terms of three parton distribution functions

[1] The twist classification follows [11]: "an observable is twist-t if its effect is effectively suppressed by $(M/Q)^{t-2}$".

(PDFs):

$$\Phi(x,S) = \frac{1}{2}\left\{ f_1(x) + S_L g_1(x)\gamma_5 + h_1\gamma_5 \not{S}_T \right\}. \tag{2.13}$$

In eq. 2.13 the longitudinal component ($(S_L/M)P^\mu$) and the transverse component (S_T^μ) of the polarization vector of the nucleon have been introduced. The three PDFs can be obtained from $\Phi(x)$:

$$\begin{aligned} f_1(x) &= \frac{1}{2}Tr(\Phi\gamma^+), \\ g_1(x) &= \frac{1}{2}Tr(\Phi\gamma^+\gamma^5), \\ h_1(x) &= \frac{1}{2}Tr(\Phi\gamma^+\gamma_T\gamma^5). \end{aligned} \tag{2.14}$$

The function $f_1(x)$ is the probability density of finding a quark with a fraction x of the nucleon momentum, $g_1(x)$, the helicity PDF, is the difference of the probability densities to find a quark with a fraction x of the longitudinal momentum with the spin parallel or anti-parallel to the nucleon spin in a longitudinally polarized nucleon; $h_1(x)$, the transversity PDF, is the difference of the probability densities to find a quark with a fraction x of the longitudinal momentum with the polarization parallel or anti-parallel to the nucleon spin in a transversely polarized nucleon.

The DIS differential cross-section in terms of the PDFs can be decomposed in a unpolarized part:

$$\frac{d^2\sigma_{unpol}}{dxdy} \propto \sum_q e_q^2 f_1^q(x) \frac{d^2\sigma^{lq\to lq}}{dxdy}, \tag{2.15}$$

and a polarized one:

$$\frac{d^2\sigma_{pol}}{dxdy} \propto P_L\lambda_L \sum_q e_q^2 g_1^q(x) \frac{d^2\sigma^{lq\to lq}}{dxdy}, \tag{2.16}$$

where P_L is the longitudinal polarization of the nucleon and λ_L is the longitudinal polarization of the lepton. The two structure functions

$$\begin{aligned} F_2(x) &= x\sum_q e_q^2 f_1^q(x), \\ g_1^N(x) &= \frac{1}{2}\sum_q e_q^2 g_1^q(x) \end{aligned} \tag{2.17}$$

have been measured in DIS experiments. The measurements of $F_2(x)$ done on proton and deuteron targets are shown in fig. 2.3 as function of Q^2 at different values of x.

Since the trasversity PDF is a chiral-odd function, so it is nondiagonal on the helicity basis, it is not present in the inclusive DIS cross-section, that describes a process in which helicity is preserved. The transversity PDF can be measured only if it's coupled with an other chiral-odd function and in the next chapter it will be

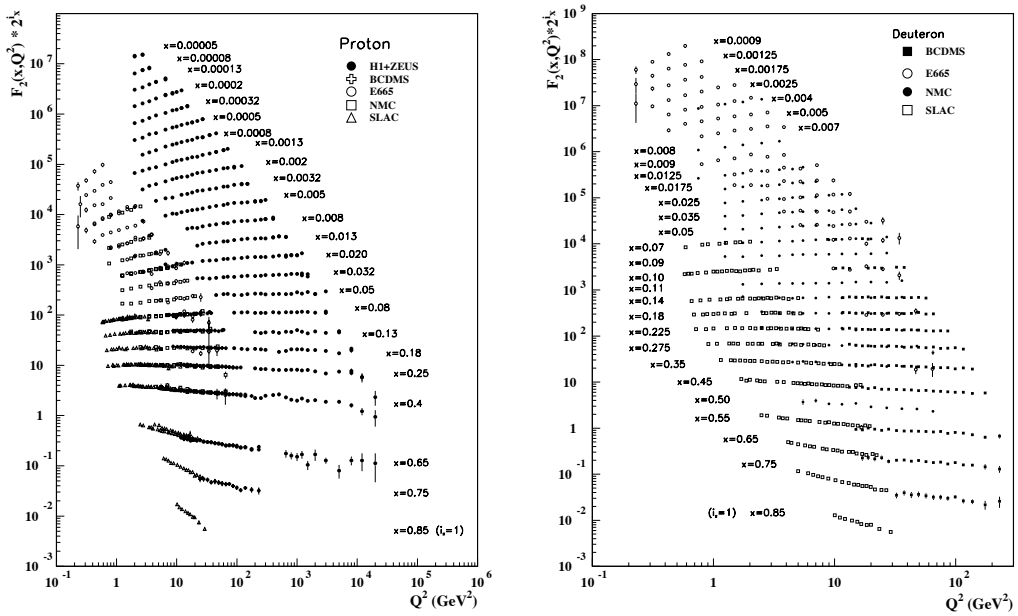

Figure 2.3: The proton structure function F_2^p and the deuteron structure function F_2^d [12].

shown that this is possible in semi-inclusive DIS. Several models presently exist for the transversity distribution. A nice compilation is given in fig. 2.4 [13]. Clearly precise measurements at x >0.4 are needed (and will come from JLab experiments after the upgrade at 12 GeV), but it is also clear that precise measurements in the complementary x range covered by COMPASS are necessary to disantangle the different models and clarify the picture.

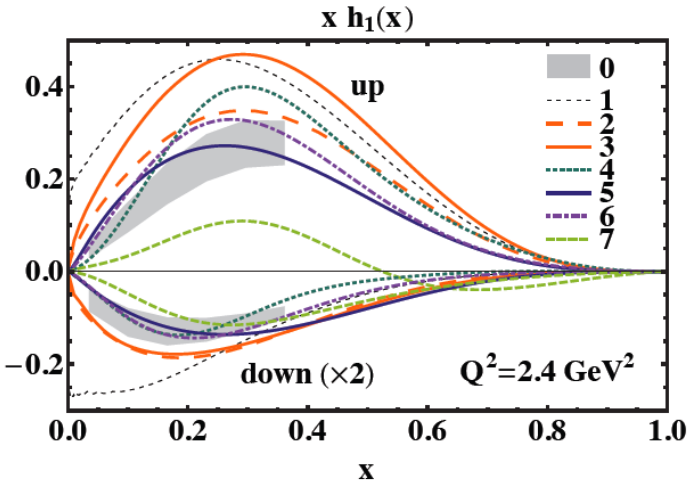

Figure 2.4: Models for the transversity distribution function compared with available parametrization: (0–shaded band) extraction from ref. [14]; (1) saturated Soffer bound [15]; (2) $h_1 = g_1$ [16]; (3-4) chiral quark-soliton models [17, 18]; (5) light-cone constituent quark model [19]; (6-7) quark-diquark models [20, 21].

2.2 Including the transverse momentum of the quark

So far the transverse momentum of the struck quark has been integrated out. If it is considered one obtains the transverse momentum dependent (TMD) correlation function [22, 23]:

$$\begin{aligned}\Phi_{ij}(x,p_T,S) &= \int dp^- \Phi_{ij}(p,P,S)\Big|_{p^+=xP^+} \\ &= \int \frac{d\xi^- d^2\xi_T}{(2\pi)^3} e^{-ip\cdot\xi}\langle P,S|\overline{\Psi}_i(\xi)\Psi_j(0)|P,S\rangle\Big|_{\xi^+=0}.\end{aligned} \tag{2.18}$$

If this function is parametrized using as base the vectors P, q, S, and p_T, eight independent TMD parton distribution functions are obtained:

$$f_1^q,\ f_{1T}^{q\perp},\ g_1^q,\ g_{1T}^q,\ h_1^q,\ h_{1L}^{q\perp},\ h_{1T}^{q\perp},\ h_1^{q\perp}. \tag{2.19}$$

Following the standard convention [24], f refers to the case of unpolarized quarks, g to longitudinally polarized quarks and h to transversely polarized quarks. If the polarization of the parent nucleon spin is indicated by L in the longitudinal case and T in the transverse case it's possible to extract the probabilities to find a quark unpolarized ($\Phi^{[\gamma^+]}$), longitudinally polarized ($\Phi^{[\gamma^+\gamma 5]}$) or transversely polarized ($\Phi^{[i\sigma^{++}\gamma 5]}$) tracing the propagator with the proper Dirac matrix:

$$\begin{aligned}\Phi^{[\gamma^+]} &= f_1^q(x,\boldsymbol{p}_T^2) - \frac{\epsilon_T^{ij} p_{Ti} S_{Tj}}{M} f_{1T}^{q\perp}(x,\boldsymbol{p}_T^2), \\ \Phi^{[\gamma^+\gamma^5]} &= S_L g_1^q(x,\boldsymbol{p}_T^2) + \frac{\boldsymbol{p}_T\cdot\boldsymbol{S}_T}{M} g_{1T}^q(x,\boldsymbol{p}_T^2), \\ \Phi^{[i\sigma^{i+}\gamma 5]} &= S_T^i h_1^q(x,\boldsymbol{p}_T^2) + S_L\frac{p_T^i}{M} h_{1L}^{q\perp}(x,\boldsymbol{p}_T^2) - \frac{p_T^i p_T^j + \frac{1}{2}p_T^2 g_T^{ij}}{m^2} S_{Tj} h_{1T}^{q\perp}(x,\boldsymbol{p}_T^2) \\ &- \frac{\epsilon_T^{ij} p_{Tj}}{M} h_1^{q\perp}(x,\boldsymbol{p}_T^2).\end{aligned} \tag{2.20}$$

The eight TMD parton distribution functions are summarized in table 2.2. If we define

$$h_1^q(x,\boldsymbol{p}_T^2) = h_{1T}^q(x,\boldsymbol{p}_T^2) - \frac{\boldsymbol{p}_T^2}{2M^2} h_{1T}^{q\perp}(x,\boldsymbol{p}_T^2) \tag{2.21}$$

the connection between the distribution functions given in eq. 2.14 and the TMD PDFs is:

$$\begin{aligned}f_1^q(x) &= \int d^2\boldsymbol{p}_T f_1^q(x,\boldsymbol{p}_T^2), \\ g_1^q(x) &= \int d^2\boldsymbol{p}_T g_1^q(x,\boldsymbol{p}_T^2), \\ h_1^q(x) &= \int d^2\boldsymbol{p}_T h_1^q(x,\boldsymbol{p}_T^2).\end{aligned} \tag{2.22}$$

Table 2.2: TMD PDFs at leading twist.

TMD PDF	*Description*
$f_1(x, p_T^2)$	unpolarized distribution
$g_1(x, p_T^2)$	helicity distribution
$h_1(x, p_T^2)$	transversity distribution
$g_{1T}(x, p_T^2)$	Worm-gear 2: distribution of longitudinally polarized quarks in transversely polarized nucleon
$f_{1T}{}^{\perp}(x, p_T^2)$	Sivers: distribution of unpolarized quark in a transversely polarized nucleon
$h_{1L}{}^{\perp}(x, p_T^2)$	Worm-gear 1: quark transverse polarization along quark intrinsic transverse momentum in the longitudinally polarized target
$h_{1T}{}^{\perp}(x, p_T^2)$	Pretzelosity: quark transverse polarization along quark intrinsic transverse momentum in the transverse polarized target
$h_1{}^{\perp}(x, p_T^2)$	Boer-Mulders: quark transverse polarization along normal to the plane defined by quark intrinsic transverse momentum and nucleon momentum in the unpolarized quark

The Boer-Mulders and Sivers functions are T-odd and so they change sign under "naive time reversal" transformation, which is an usual time reversal transformation but without interchange of the initial and final state. This is due to the fact that the application of the time reversal changes the path of the gauge link which enters in the definition of the TMDs. The gauge link depends on the specific process. For example, the gauge link in SIDIS and Drell-Yan processes are related by a time-reversal transformation, implying that the Sivers and Boer-Mulders functions in the two processes differ by a sign.

2.3 Semi-inclusive deep inelastic scattering

In SIDIS at least one hadron (with four-momentum P_h and mass M_h) is detected in the final state. In this section the one-particle DIS, in which at least one hadron is detected, and the two-particles DIS, in which at least two hadrons are detected in the final state, will be considered separately. In both cases one must distinguish the hadrons created from the fragmentation of the struck quark from those coming from the fragmentation of the target remnants. From the experimental point of view this distinction is done by applying a cut on the minimum value of the fraction of energy carried by the single hadron or by the hadron pair.

Hadron production in DIS

The Feynman diagram of one-particle SIDIS in shown in fig. 2.5. To describe this reaction a new relativistic invariant variable, (z_h) is introduced:

$$z_h = \frac{P \cdot P_h}{P \cdot q}, \tag{2.23}$$

which represents the fraction of the total energy available in the reaction carried by the hadron. To describe SIDIS processes it is convenient to introduce a refer-

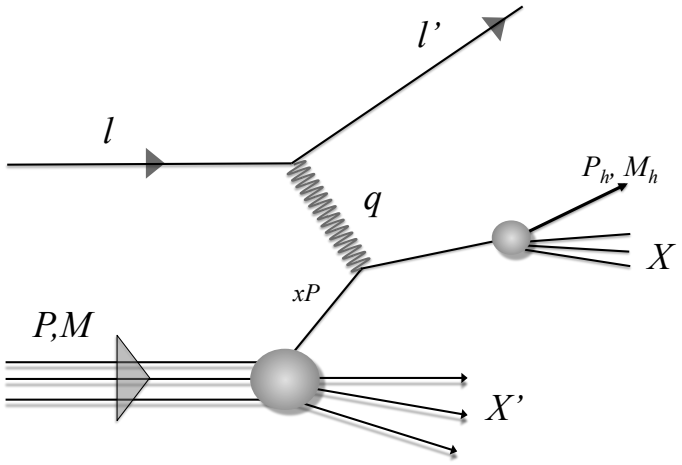

Figure 2.5: Diagram of the One-particle semi-inclusive deep inelastic scattering.

ence frame different from that used in the previous paragraph, in the description of the inclusive DIS, namely a frame in which the target and the outgoing hadron momenta are collinear. In this frame the photon transverse momentum component are different from zero:

$$\begin{aligned} P^\mu &= \left[P^+, \frac{M^2}{2P^+}, \mathbf{0}_T \right], \\ P_h^\mu &= \left[\frac{M_h^2}{2P_h^-}, P_h^-, \mathbf{0}_T \right], \\ q^\mu &\approx \left[-x_B P^+, \frac{P_h^-}{z_h}, \boldsymbol{q}_T \right] \end{aligned} \tag{2.24}$$

$P_h^- \approx Q^2 z_h/(2P^+ x_B)$. The transverse component of the momentum of the quark can be related to the transverse component of the momentum of the hadron, $\boldsymbol{P}_{hT}$, in the frame in which the photon momentum is parallel to the z direction by the following relation:

$$\boldsymbol{q}_T = \frac{\boldsymbol{P}_{hT}}{z_h}. \tag{2.25}$$

The final state X in the hadronic tensor defined in eq. 2.3 can be split in the sum of the hadron state h and the remnant state X'; so the one-particle hadronic tensor can be defined as:

$$\begin{aligned} 2MW^{\mu\nu}(q,P,S) =& \frac{1}{(2\pi)^4}\sum_{X'}\int \frac{d^3P_{X'}}{(2\pi)^3 2P^0_{X'}}(2\pi)^4\delta^4(q+P-P_{X'}-P_h) \\ & \times \langle P,S|J^\mu(0)|P_h,X'\rangle\langle P_h,X'|J^\nu(0)|P,S\rangle. \end{aligned} \tag{2.26}$$

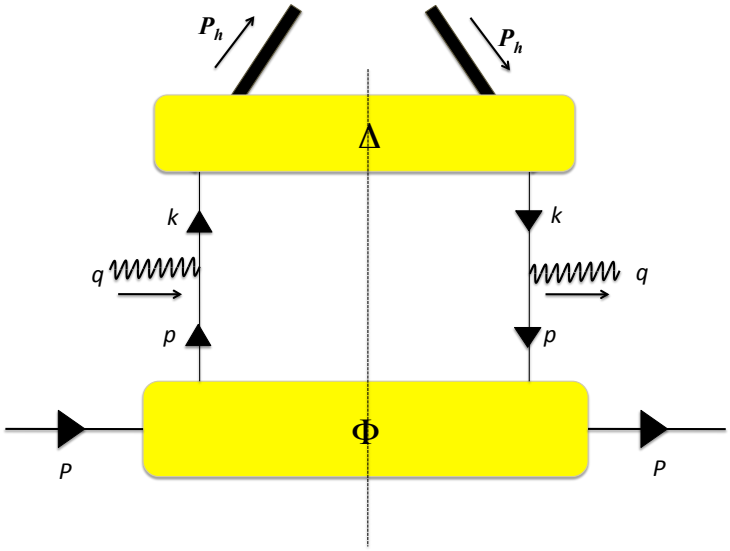

Figure 2.6: handbag diagram of semi-inclusive deep inelastic scattering.

The handbag diagram which describes the one-particle SIDIS process is shown in fig. 2.6. The four-vectors p and k in fig. 2.6 can be parametrized as:

$$\begin{aligned} p^\mu &= \left[xP^+, \frac{p^2+|\boldsymbol{p}_T^2|}{2xP^+}, \boldsymbol{p}_T\right], \\ k^\mu &= \left[\frac{z_h(k^2+|\boldsymbol{k}_T^2|)}{2P_h^-}, \frac{P_h^-}{z_h}, \boldsymbol{k}_T\right]. \end{aligned} \tag{2.27}$$

As evident from fig. 2.6, it is necessary to introduce a new function which describes the fragmentation of the struck quark: the fragmentation function Δ [25]. The hadronic tensor related to this process is given by:

$$
\begin{aligned}
2MW^{\mu\nu}(q,P,S,P_h) &= 2z_h \sum_q e_q^2 \int d^2\boldsymbol{p}_T d^2\boldsymbol{k}_T \delta^2(\boldsymbol{p}_T + \boldsymbol{q}_T - \boldsymbol{k}_T) \\
&\times Tr\left[\int dp^- \Phi^q(p,P)|_{p^+=xP^+}\gamma^\mu \times \int dk^+ \Delta^q(k,P_h)|_{P^-=z_h k^-}\gamma^\nu\right] \\
&= 2z_h \sum_q e_q^2 \int d^2\boldsymbol{p}_T d^2\boldsymbol{k}_T \delta^2(\boldsymbol{p}_T + \boldsymbol{q}_T - \boldsymbol{k}_T)\left[Tr[\Phi^q(x,\boldsymbol{p}_T)\gamma^\mu \Delta^q(z_h,\boldsymbol{k}_T)\gamma^\nu]\right],
\end{aligned}
\tag{2.28}
$$

where $\Phi^q(x,\boldsymbol{p}_T)$ and $\Delta^q(z_h,\boldsymbol{k}_T)$ are the quark-quark correlation function and the fragmentation correlation function, respectively. The correlation function Φ and the fragmentation correlator Δ have been parametrized up to twist-3 level [26] and the SIDIS cross-section obtained in the laboratory frame is given in eq. 2.29 where α is the fine structure function:

$$
\begin{aligned}
\frac{d\sigma}{dxdydz_h d\phi_h dP_{h\perp}^2} &= \frac{\alpha^2}{xyQ^2}\frac{y^2}{2(1-\epsilon)}\left(1+\frac{\gamma^2}{2x}\right) \\
&\times\Bigg\{ F_{UU,T} + \epsilon F_{UU,L} + \sqrt{2\epsilon(1+\epsilon)}cos\phi_h F_{UU}^{cos\phi_h} \\
&+ \epsilon cos(2\phi_h) F_{UU}^{cos2\phi_h} + \lambda_e\sqrt{2\epsilon(1-\epsilon)}sin\phi_h F_{LU}^{sin\phi_h} \\
&+ S_L\left[\sqrt{1-\epsilon^2}F_{LL} + \sqrt{2\epsilon(1-\epsilon)} + \epsilon sin(2\phi_h)F_{UL}^{sin(2\phi_h)}\right] \\
&+ \lambda_e S_L\left[\sqrt{1-\epsilon^2}F_{LL} + \sqrt{2\epsilon(1-\epsilon)}cos\phi_h F_{LL}^{cos\phi_h}\right] \\
&+ S_T\left[sin(\phi_h-\phi_S)(F_{UT,T}^{sin(\phi_h-\phi_S)} + \epsilon F_{UT,L}^{sin(\phi_h-\phi_S)})\right] \\
&+ \epsilon sin(\phi_h+\phi_S)F_{UT}^{sin(\phi_h+\phi_S)} + \epsilon sin(3\phi_h-\phi_S)F_{UT}^{sin(3\phi_h-\phi_S)} \\
&+ \sqrt{2\epsilon(1+\epsilon)}sin\phi_S F_{UT}^{sin\phi_S} \\
&+ \sqrt{2\epsilon(1+\epsilon)}sin(2\phi_h-\phi_S)F_{UT}^{sin(2\phi_h-\phi_S)} \\
&+ \lambda_e S_T\left[\sqrt{1-\epsilon^2}cos(\phi_h-\phi_S)F_{LT}^{cos(\phi_h-\phi_S)}\right. \\
&+ \sqrt{2\epsilon(1-\epsilon)}cos\phi_S F_{LT}^{cos\phi_S} \\
&\left.+ \sqrt{2\epsilon(1-\epsilon)}cos(2\phi_h-\phi_S)F_{UT}^{cos(2\phi_h-\phi_S)}\right\}.
\end{aligned}
\tag{2.29}
$$

A graphical representation of the azimuthal angles ϕ_S and ϕ_h is given in fig. 2.7 in the so called gamma-nucleon-system (GNS) in which the virtual photon direction defines the z axis and the the lepton scattering plane defines the xz plane. In eq. 2.29 λ_e is the helicity of the lepton beam, S_L and S_T are respectively the longitudinal and transverse component of the target polarization with respect to the photon direction.

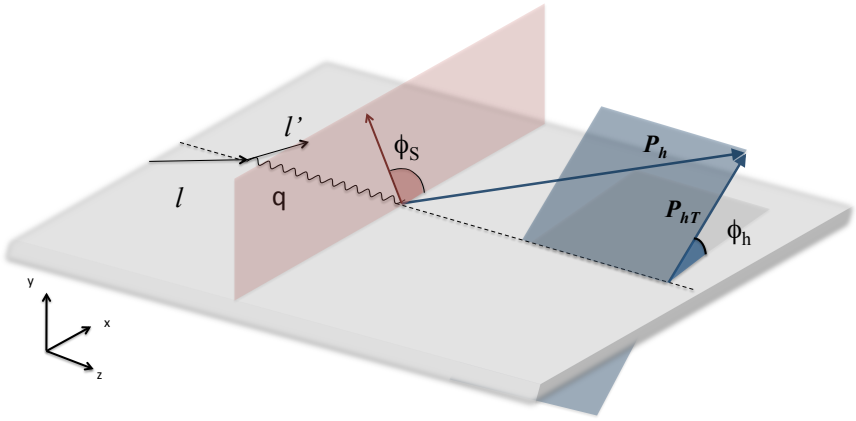

Figure 2.7: Graphical description of the one-particle semi-inclusive deep inelastic scattering.

The cross-section is parametrized with 18 structure functions F_{XY} where X indicates the polarization of the beam and Y the polarization of the target; the further third index specifies the polarization of the virtual photon. Each structure function is coupled with a different modulation which depends by the azimuthal angle of the hadron ϕ_h, the azimuthal angle of the spin of the target ϕ_S or by a combination of both. Each structure function depends also on the ratio between the longitudinal and the transverse photon flux

$$\epsilon = \frac{1 - y - \frac{1}{4}\gamma^2 y^2}{1 - y + \frac{1}{2}y^2 + \frac{1}{4}\gamma^2 y^2} \tag{2.30}$$

where $\gamma = \frac{2Mx}{Q} \approx 0$ will be neglected in the following.

In the next chapter we will describe the mechanism which permits to access the transversity from the $F_{UT}^{sin(\phi_h+\phi_S)}$ structure function in which the transversity PDF is coupled with another chiral-odd function: the Collins fragmentation function [27].

Two hadron production in inclusive DIS

In this paragraph we will consider the case in which at least two hadrons in the final state are detected. In the early 1990, it was suggested for the first time that this process would allow to access transversity in an alternative way with respect to the case of one-particle SIDIS [28, 29, 30]. The Feynman diagram which describes this reaction is shown in fig. 2.8. The two detected hadrons have masses M_1 and M_2 and four-momenta P_1 and P_2. The two-hadron four-momentum of centre of mass will be denoted as P_{2h} and the two-hadron invariant mass will be denote as M_{inv}, $\boldsymbol{R} = (\boldsymbol{P}_1 - \boldsymbol{P}_2)/2$ is the semi-difference of the momenta of the two hadrons while the variable $\xi = P_1^-/P_{2h}^-$ takes into account how the total momentum is shared inside the hadron pair.

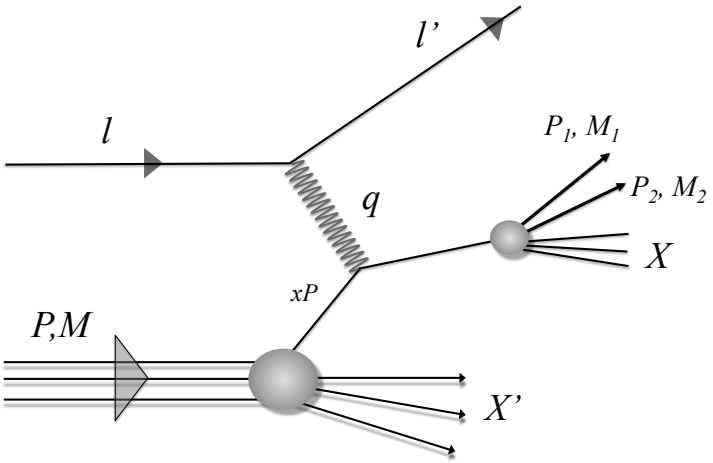

Figure 2.8: Diagram of the two-particle semi-inclusive deep inelastic scattering.

Using the same rules used in the case of one hadron production in SIDIS on can write [31]:

$$\begin{aligned} R^{\mu} &= \left[\frac{(M_1^2 - M_2^2) - (\xi - \frac{1}{2})M_{inv}^2}{2P_{2h}^-}, (\xi - \frac{1}{2})P_{2h}^-, \boldsymbol{R}_T^{\perp}\right], \\ P_1^{\mu} &= \left[\frac{M_1^2 + \boldsymbol{R}_T^{\perp 2}}{2\xi P_{2h}^-}, \xi P_{2h}^-, \boldsymbol{R}_T^{\perp}\right], \\ P_2^{\mu} &= \left[\frac{M_2^2 + \boldsymbol{R}_T^{\perp 2}}{2(1-\xi) P_{2h}^-}, (1-\xi) P_{2h}^-, -\boldsymbol{R}_T^{\perp}\right], \end{aligned} \tag{2.31}$$

where $\boldsymbol{R}_T^{\perp}$ is the transverse component of $\mathbb{R}$ with respect to the $\boldsymbol{P}_{2h}$ direction. The final state can be split in three states with momenta P_1, P_2 and $P_{X'}$ where X' is the remnant state. The hadronic tensor which describes the two-hadron SIDIS is:

$$\begin{aligned} 2MW^{\mu\nu}(q, P, S, P_1, P_2) = \frac{1}{(2\pi)^7} \sum_{X'} \int \frac{d^3\boldsymbol{P_{X'}}}{(2\pi)^3 2P_{X'}^0} \times (2\pi)^4 \delta^4(q + P - P_{X'} - P_1 - P_2) \\ \times \langle P, S|J^{\mu}(0)|P_1, P_2, X'\rangle\langle P_1, P_2, X'|J^{\nu}(0)|P, S|\rangle. \end{aligned} \tag{2.32}$$

The handbag diagram which describes the two-hadron production is shown in fig.2.9. As for the one-particle SIDIS case, at leading order in $1/Q$ the hadronic tensor can be expressed in terms of the quark-quark correlation function Φ and the fragmentation correlation function Δ; by integrating over the transverse component of the centre-of-mass momentum $\boldsymbol{P}_{2hT}$ it's given by:

$$\begin{aligned} 2MW^{\mu\nu}(q, P, S, P_1, P_2) &= z_{2h} Tr[\Phi(x, S)\gamma^{\mu}\Delta(z_{2h}, \xi, M_{inv}^2, \phi_R)\gamma^{\nu}] \\ \Delta(z_{2h}, \xi, M_{inv}^2, \phi_R) &= z_{2h} \int dk^+ d^2\boldsymbol{k}_T \Delta(k, P_{2h}, R)\Big|_{k^- = P_{2h}^-/z_{2h}}, \end{aligned} \tag{2.33}$$

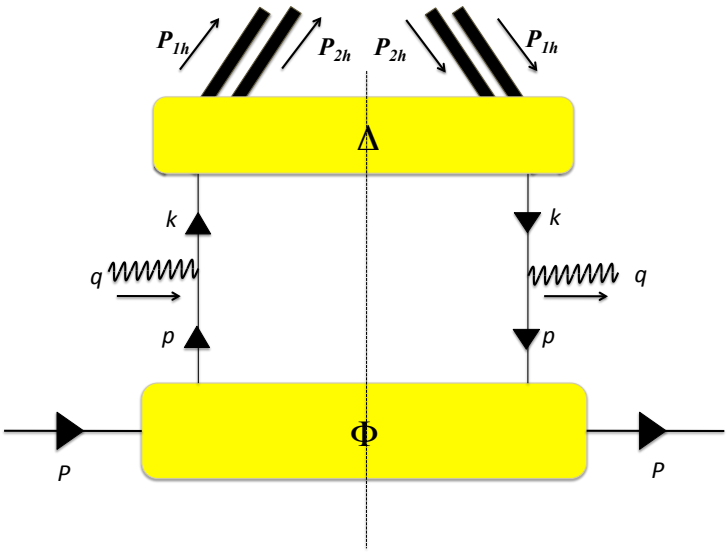

Figure 2.9: handbag diagram of the two-hadron production in semi-inclusive deep inelastic scattering.

where $z_{2h} = z_1 + z_2$. The differential cross-section obtained for the two-hadron pair production at leading twist by integrating over the transverse component of the centre-of-mass momentum P_{2hT} is:

$$\frac{d^7\sigma}{d\xi dM_{inv}^2 d\phi_R dz_{2h} dx dy d\phi_S} = \frac{2\alpha^2}{4\pi s x y^2} \sum_q e_q^2 \Bigg[A(y) f_1^q(x) D_1^q(z_{2h}, \xi, M_{inv}^2) + \lambda_e S_L C(y) g_1^q(x) D_1^q(z_{2h}, \xi, M_{inv}^2) + B(y)|S_\perp| \frac{|\boldsymbol{R}_T^\perp|}{M_{inv}} sin(\phi_R + \phi_S) h_1^q(x) H_1^{\sphericalangle q}(z_{2h}, \xi, M_{inv}^2) \Bigg], \tag{2.34}$$

where $A(y) = (1 - y + y^2/2)$, $B(y) = (1 - y)$ and $C(y) = y(2 - y)$. The two fragmentation functions $D_1^q(z_{2h}, \xi, M_{inv}^2)$ and $H_1^{\sphericalangle q}(z_{2h}, \xi, M_{inv}^2)$ will be discussed in the next chapter. The relevant point, here, is that the Di-hadron FF is a chiral-odd function (very much as the Collins FF) so it can be coupled with transversity to give an observable.

A graphical representation of the quantities involved in the cross-section is given in fig. 2.10 in the GNS and using the definition of $\boldsymbol{R}_T$ given in eq. 2.37. In the GNS the azimuthal angles ϕ_S and ϕ_R are defined as:

$$cos\phi_S = \frac{(\hat{\boldsymbol{q}} \times \boldsymbol{l})}{|\hat{\boldsymbol{q}} \times \boldsymbol{l})} \cdot \frac{(\hat{\boldsymbol{q}} \times \boldsymbol{S})}{|\hat{\boldsymbol{q}} \times \boldsymbol{S}|}, \qquad sin\phi_S = \frac{(\boldsymbol{l} \times \boldsymbol{S}) \cdot \hat{\boldsymbol{q}}}{|\hat{\boldsymbol{q}} \times \boldsymbol{l}||\hat{\boldsymbol{q}} \times \boldsymbol{S}|} \tag{2.35}$$

$$cos\phi_R = \frac{(\hat{\boldsymbol{q}} \times \boldsymbol{l})}{|\hat{\boldsymbol{q}} \times \boldsymbol{l})} \cdot \frac{(\hat{\boldsymbol{q}} \times \boldsymbol{R}_T^\perp)}{|\hat{\boldsymbol{q}} \times \boldsymbol{R}_T^\perp|}, \qquad sin\phi_R = \frac{(\boldsymbol{l} \times \boldsymbol{R}_T^\perp) \cdot \hat{\boldsymbol{q}}}{|\hat{\boldsymbol{q}} \times \boldsymbol{l}||\hat{\boldsymbol{q}} \times \boldsymbol{R}_T^\perp|}. \tag{2.36}$$

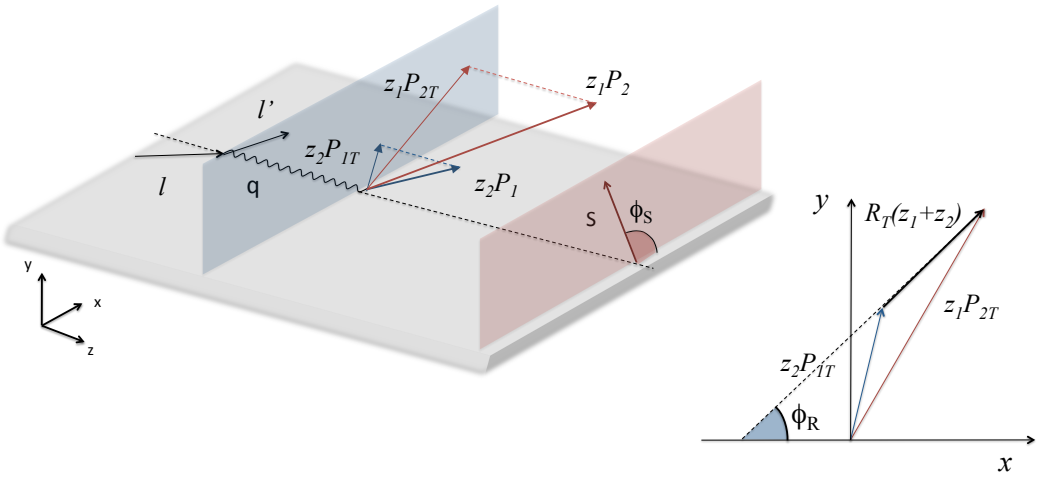

Figure 2.10: Graphical representation of the two-hadron production in semi-inclusive deep inelastic scattering.

Consideration on R definition

The vector $\boldsymbol{R} = (\boldsymbol{P}_1 - \boldsymbol{P}_2)/2$ is not invariant against boosts in direction of the virtual photon. For this reason in the eq. 2.36 the $\boldsymbol{R}_T^{\perp}$ will be replaced by [30]:

$$\boldsymbol{R}_T = \frac{z_2\boldsymbol{P}_{1T} - z_1\boldsymbol{P}_{2T}}{z_1 + z_2} \tag{2.37}$$

where $\boldsymbol{P}_{1T}$ and $\boldsymbol{P}_{2T}$ are the transverse components of the hadron momentum with respect to the direction of the virtual photon. The $\boldsymbol{R}_T$ vector is orthogonal to the virtual photon direction ($\hat{q}$) and so it is invariant with respect to boosts along $\hat{q}$. In the GNS the azimuthal angle ϕ_R is the same if one use the vector $\boldsymbol{R}_T$ or $\boldsymbol{R}_T^{\perp}$ in the eq. 2.36.

Chapter 3

Measuring the transversity PDF in SIDIS

In the previous chapter we have seen that three parton distribution functions are necessary at leading-twist in the collinear case to describe the nucleon: the unpolarized, the helicity and the transversity PDFs. The first two PDFs can be measured in DIS while the third one, the transversity PDF h_1^q is chiral-odd and cannot be measured in inclusive DIS because in this process the chirality is conserved. So, to access transversity, we need to couple it with an other chiral-odd function. This is possible in Semi-Inclusive DIS (SIDIS) of a lepton off a transversely polarized target where h_1^q can be coupled with three different chiral-odd functions: the Collins FF in the one hadron production, the Di-hadron FF in the hadrons pair production and the transverse spin dependent fragmentation function of a quark in a Λ particle [32, 30]. All these three channels have been and are studied in COMPASS.

A possible alternative process to measure the transversity PDF is the Drell-Yan (DY) process [6, 33, 34]. In this process, shown in fig. 3.1, a quark and an antiquark belonging to the initial state hadrons h_1 and h_2, annihilate producing a virtual photon γ^* which decays into two leptons. The cross-section of the DY process in

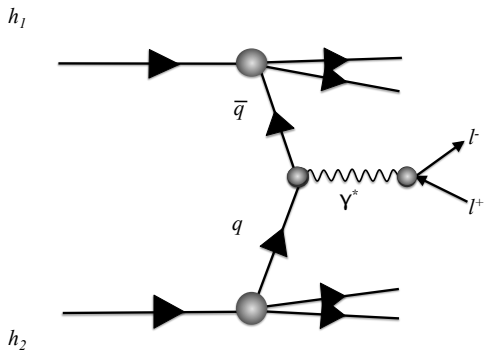

Figure 3.1: Schematic representation of the DY process.

the case of unpolarized beam off a transversely polarized target consists of different

modulations, one of which has an amplitude proportional to the convolution of the transversity PDF with the prezelosity PDF (see table 2.2). The measurement of this amplitude allows to access transversity in a channel which differs from that considered in SIDIS because in this case h_1^q is coupled with an other PDF and not with a fragmentation function. Particularly interesting would be the measurement of the DY process in transversely polarized $p\overline{p}$ interactions [35, 36]. Feasibility studies for polarizing anti-protons are ongoing but it is a very channelling goal. Precise measurements in polarized pp interactions will be performed at RHIC [37, 38]. In the following we will only concentrate on the transversity measurement through one hadron and hadron pair production in SIDIS off transversely polarized targets. In the last section the relevant existing data will be reviewed.

3.1 The Collins asymmetry

The $\Delta^q(z_h, \boldsymbol{k}_T)$ FF defined in eq. 2.28 can be parametrized in terms of the Dirac structures $(\mathbb{1}, \gamma^\mu, \gamma_5, \gamma^\mu\gamma_5, \sigma^{\mu\nu}, \sigma^{\mu\nu}\gamma_5)$ in the same way used to parametrize the correlation function $\Phi_{ij}(x, S)$ [26, 39] . For a spinless final state hadron at leading twist $\Delta^q(z_h, \boldsymbol{k}_T)$ is the combination of two fragmentation functions (FFs), the unpolarized FF $D_1^q(z_h, k_T^2)$ and the Collins FF $H_1^{\perp q}(z_h, k_T^2)$:

$$\Delta^q(z_h, \boldsymbol{k}_T) = \frac{1}{2}\left[D_1^q(z_h, \boldsymbol{k}_T^2) + iH_1^{\perp q}(z_h, \boldsymbol{k}_T^2)\frac{\not{\boldsymbol{k}}_T}{2M_h}\right]. \tag{3.1}$$

The unpolarized FF describes the fragmentation of an unpolarized quark into an unpolarized hadron while the Collins FF is the difference between the FF of a quark with a transverse polarization upwards into an unpolarized hadron and the FF of a quark with a transverse polarization downwards into an unpolarized hadron. The unpolarized and Collins FFs can be obtained considering the distribution of hadrons produced from quarks with opposite polarization:

$$\begin{aligned} D_{h/q^\uparrow} &= \frac{1}{2}\left[D_1^q(z_h, \boldsymbol{k}_T^2) + H_1^{\perp q}(z_h, \boldsymbol{k}_T^2)\frac{(\hat{p}\times\boldsymbol{k}_T)\cdot\boldsymbol{S'}_{qT}}{z_h M_h}\right], \\ D_{h/q^\uparrow} + D_{h/q^\downarrow} &= D_1^q(z_h, \boldsymbol{k}_T^2), \\ D_{h/q^\uparrow} - D_{h/q^\downarrow} &= H_1^{\perp q}(z_h, \boldsymbol{k}_T^2)\frac{(\hat{p}\times\boldsymbol{k}_T)\cdot\boldsymbol{S'}_{qT}}{z_h M_h}. \end{aligned} \tag{3.2}$$

Where $\hat{p}$ is the versor in the direction of the quark three-momentum and $\boldsymbol{S'}_{qT}$ is the spin vector of the fragmenting quark. As anticipated in the last paragraph, the Collins FF is a chiral-odd function that can be coupled with transversity PDF in SIDIS. If we consider the one-hadron cross-section given in eq. 2.29 and we indicate with $\sigma^\uparrow$ and $\sigma^\downarrow$ the cross-sections with opposite transverse polarizations, in the difference $\sigma^\uparrow - \sigma^\downarrow$ all the terms which do not depend by the transverse polarization of the target drop out. Only nine of the eighteen structure functions in eq. 2.29

survive in the transverse spin asymmetries given by:

$$\begin{aligned}\frac{\sigma^{\uparrow}-\sigma^{\downarrow}}{\sigma^{\uparrow}+\sigma^{\downarrow}} = \frac{S_T}{F_{UU}}\Bigg\{ & (F_{UT,T}^{sin(\phi_h-\phi_S)} + \epsilon F_{UT,L}^{sin(\phi_h-\phi_S)}) sin(\phi_h-\phi_S) \\ & + \epsilon F_{UT}^{sin(\phi_h+\phi_S)} sin(\phi_h+\phi_S) \\ & + \sqrt{2\epsilon(1+\epsilon)} F_{UT}^{sin(2\phi_h-\phi_S)} sin(2\phi_h-\phi_S) \\ & + \epsilon F_{UT}^{sin(3\phi_h-\phi_S)} sin(3\phi_h-\phi_S) \\ & + \sqrt{2\epsilon(1+\epsilon)} F_{UT}^{sin(\phi_S)} sin(\phi_S) \\ & + S_T\lambda\sqrt{1-\epsilon^2} F_{LT}^{cos(\phi_h-\phi_S)} cos(\phi_h-\phi_S) \\ & + S_T\lambda\sqrt{2\epsilon(1-\epsilon)} F_{LT}^{cos(2\phi_h-\phi_S)} cos(2\phi_h-\phi_S) \\ & + S_T\lambda\sqrt{2\epsilon(1-\epsilon)} F_{LT}^{cos(\phi_S)} cos(\phi_S) \Bigg\}. \end{aligned} \tag{3.3}$$

In this expression λ is the incoming lepton helicity. All the modulations in eq. 3.3 are orthogonal so each term can be extracted independently from the same data by integrating over all the other terms.

The generic structure functions in eq. 3.3 is given by convolutions of the type:

$$\mathcal{C}[wfD] = x\sum_q e_q^2 \int d^2\boldsymbol{p}_T^2 d^2\boldsymbol{k}_T^2 \delta^2(\boldsymbol{p}_T - \boldsymbol{k}_T - \frac{\boldsymbol{P}_{hT}}{z_h}) w(\boldsymbol{p}_T,\boldsymbol{k}_T) f^q(x,\boldsymbol{p}_T^2) D^q(z_h,\boldsymbol{k}_T^2) \tag{3.4}$$

where f^q is a TMD PDF, D^q is a fragmentation function, $w(\boldsymbol{p}_T,\boldsymbol{k}_T)$ is a weight function of the transverse momenta, and the summation runs over quark and antiquark flavours.

Four of the nine transverse structure functions can be expressed via leading twist PDFs [26]:

$$\begin{aligned} F_{UT}^{sin(\phi_h+\phi_S)} &= \mathcal{C}\left[-\frac{\hat{h}\cdot\boldsymbol{k}_T}{M_h} h_1^q H_1^{q\perp} \right], \\ F_{UT,T}^{sin(\phi_h-\phi_S)} &= \mathcal{C}\left[-\frac{\hat{h}\cdot\boldsymbol{p}_T}{M} f_{1T}^{q\perp} D \right], \\ F_{UT}^{sin(3\phi_h-\phi_S)} &= \mathcal{C}\left[\frac{2(\hat{h}\cdot\boldsymbol{p}_T)(\boldsymbol{p}_T\cdot\boldsymbol{k}_T) + \boldsymbol{p}_T^2(\hat{h}\cdot\boldsymbol{k}_T) - 4(\hat{h}\cdot\boldsymbol{p}_T)(\hat{h}\cdot\boldsymbol{k}_T)}{2M^2 M_h} h_{1T}^{\perp} H_1^{\perp} \right], \\ F_{LT}^{cos(\phi_h-\phi_S)} &= \mathcal{C}\left[\frac{(\hat{h}\cdot\boldsymbol{p}_T)}{M} g_{1T} D \right]. \end{aligned} \tag{3.5}$$

Where $\hat{h} = \frac{\boldsymbol{P}_{hT}}{|\boldsymbol{P}_{hT}|}$. If we consider only the $sin(\phi_h+\phi_S)$ modulation in eq. 3.3, integrating over all the other angles, and defining the Collins angle $\phi_C = \phi_h + \phi_S - \pi$[1]

[1]This convention is adopted in the COMPASS collaboration and implies a change of the sign for the final asymmetry with respect to the result obtained without subtracting an angle π.

we obtain:

$$\frac{\sigma^{\uparrow}-\sigma^{\downarrow}}{\sigma^{\uparrow}+\sigma^{\downarrow}} = S_T D_{NN} A_{Coll} sin(\phi_C), \tag{3.6}$$

where

$$A_{Coll} = \frac{\sum_q e_q^2 \mathcal{C}\left[-\frac{\hat{h}\cdot \boldsymbol{k}_T}{M_h} h_1^q(x,\boldsymbol{p}_T) H_1^{q\perp}(z_h,\boldsymbol{k}_T)\right]}{\sum_q e_q^2 \mathcal{C}\left[f_1^q(x,\boldsymbol{p}_T) D_1^q(z_h,\boldsymbol{k}_T)\right]}, \tag{3.7}$$

and

$$D_{NN} = \frac{1-y}{1-y+\frac{1}{2}y^2}. \tag{3.8}$$

From eq. 3.7 it is clear how it's possible to access transversity measuring A_{Coll} and the Collins FF. SIDIS gives acces to the A_{Coll} asymmetry. Combinations of the Collins FFs can be measured in e^+e^- collision in which two hadrons produced in the reaction $e^+e^- \to h_1 h_2 X$ are detected. Two methods can be used to perform this measurement. The first method is based on the $cos(\phi_1+\phi_2)$ modulation of the azimuthal angle of the two hadrons as depicted in fig. 3.2. In this case the azimuthal asymmetry is given by:

$$A(z_1,z_2,\vartheta,\phi_1+\phi_2) = \\ 1+\frac{1}{8}\frac{sin^2\vartheta}{1+cos^2\vartheta} cos(\phi_1+\phi_2) \frac{\sum_q e_q^2 \mathcal{C}\left[w(\boldsymbol{k}_{1T},\boldsymbol{k}_{2T}) H_1^{q\perp}(z_1,\boldsymbol{k}_{1T}^2) H_1^{\overline{q}\perp}(z_2,\boldsymbol{k}_{2T}^2)\right]}{\sum_q e_q^2 \mathcal{C}\left[D_1^q(z_1,\boldsymbol{k}_{1T}^2) \overline{D}_1^q(z_2,\boldsymbol{k}_{2T}^2)\right]}, \tag{3.9}$$

where ϕ_1 and ϕ_2 are the azimuthal angles of h_1 and h_2 with respect to the scattering plane while ϑ is the angle between the e^+ direction and the axis of production of the hadrons and $w(\boldsymbol{k}_{1T},\boldsymbol{k}_{2T})$ is a weight function. As evident by measuring $A(z_1,z_2,\vartheta,\phi_1+\phi_2)$ one can access only the product of the two Collins fragmentation functions. This measurement has been performed at Belle [40], the results will be shown in sec. 3.3.

3.2 Two hadrons asymmetry

The fragmentation function introduced in eq. 2.33 can be parametrized in the same way used for the fragmentation function in the one hadron production in SIDIS discussed in the last paragraph. At leading twist and integrating over the $\boldsymbol{P}_{2hT}$, the transverse momentum of the hadron pair, $\Delta(z_{2h},\xi,M_{inv}^2,\phi_R)$ is given by:

$$\Delta(z_{2h},\xi,M_{inv}^2,\phi_R) = \frac{1}{8\pi}\left(D_1^{q\to h_1 h_2}(z_{2h},\xi,M_{inv}^2) + i H_1^{\sphericalangle q}(z_{2h},\xi,M_{inv}^2) \frac{\boldsymbol{R}_T}{M_{inv}}\right), \tag{3.10}$$

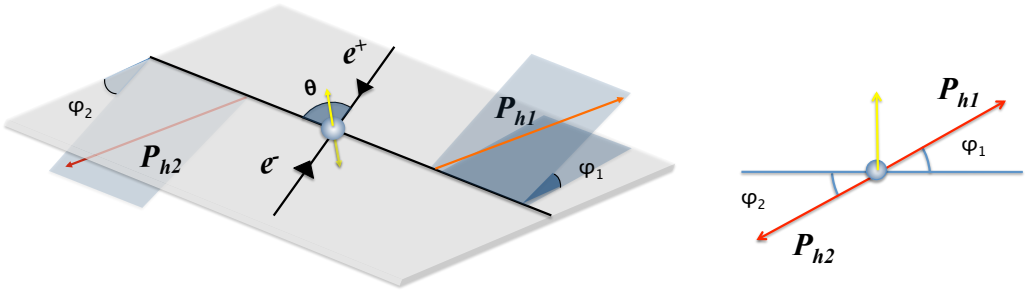

Figure 3.2: Graphical representation of the $e^+e^-\rightarrow h_1h_2$X reactions and definition of ϕ_1 and ϕ_2.

i.e. it is the combination of two terms: the unpolarized FF $D_1^q(z_{2h},\xi,M_{inv}^2)$ and the spin-dependent di-hadron FF $H_1^{\sphericalangle q}(z_{2h},\xi,M_{inv}^2)$. The unpolarized FF gives the probability for an unpolarized quark to fragment into two unpolarized hadrons while the di-hadron FF is the probability difference for a transversely polarized quark with opposite chiralities to fragment into the hadron pair. The di-hadron FF is chiral-odd and, as discussed in the previous paragraphs, is one of the three functions which can couple to transversity in SIDIS.

If we introduce the quantity:

$$A_{2h}=\frac{\sum_q e_q^2\frac{|R_T|}{M_{inv}}h_1^q(x)H_1^{\sphericalangle q\rightarrow h^+h^-}(z_{2h},\xi,M_{inv}^2)}{\sum_q e_q^2 f_1^q(x)D^{q\rightarrow h^+h^-}(z_{2h},\xi,M_{inv}^2)}, \tag{3.11}$$

and we indicate with $\sigma^{\uparrow}$ and $\sigma^{\downarrow}$ the cross-sections for opposite transverse polarizations of the quarks, from eq. 2.34 we obtain:

$$\frac{\sigma^{\uparrow}-\sigma^{\downarrow}}{\sigma^{\uparrow}+\sigma^{\downarrow}}=S_T D_{NN}A_{2h}sin(\phi_{RS}), \tag{3.12}$$

where $D_{NN}=(1-y)/(1-y+y^2/2)$ is the spin transfer coefficient from the initial to the struck quark, $\phi_{RS}=\phi_R+\phi_S-\pi$ [2] and ϕ_R and ϕ_S are defined in eq. 2.35 and eq. 2.36.

The measurement of A_{2h} permits to measure transversity. The advantage to using the di-hadron asymmetry instead of the Collins asymmetry is that the di-hadron FF does not depend on the partonic transverse momentum. This permits to integrate over the transverse component of the center-of-mass momentum $\boldsymbol{P}_{2hT}$ of the hadron pair, and the asymmetry depends on the product of the transversity PDF and di-hadron FF and not on their convolution. This feature permits to avoid the criticism due to the modelling of the $\boldsymbol{p}_T$ dependence in the PDFs and FFs needed to evaluate the convolution of eq. 3.4.

[2] This convention is adopted in the COMPASS collaboration and implies a change of the sign for the final asymmetry with respect to the result obtained without subtracting an angle π.

As for the Collins asymmetry also for the two hadron asymmetry in SIDIS it is necessary to measure the di-hadron FF to access transversity. This measurement has been performed for the first time at Belle with the same method described in the last section to evaluate the Collins FF. In this case the process $e^+e^- \to h_1h_2h_3h_4X$ is investigated and 4 hadrons are detected each with four-momentum P_i. If we consider the quantities $R_1{=}P_1 - P_2$ and $R_2{=}P_3 - P_4$ and the azimuthal angles of $\boldsymbol{R_1}$ and $\boldsymbol{R_2}$, ϕ_{R1} and ϕ_{R2} depicted in fig. 3.3, the number of pairs produced has an azimuthal dependence of the type $cos(\phi_{R1} + \phi_{R2})$. The azimuthal asymmetry is given by:

$$A(z_1, z_2, \theta, \phi_{R1} + \phi_{R2}, M^2_{1,2}, M^2_{3,4}) = \frac{1}{2}\frac{sin^2\theta}{1 + cos^2\theta} cos(\phi_{R1} + \phi_{R2}) \frac{\left[\sum_{q,\overline{q}} e_q^2 z_1^2 z_2^2 H_1^{\sphericalangle q}(z_1, M^2_{1,2}) H_1^{\sphericalangle \overline{q}}(z_2, M^2_{3,4})\right]}{\left[\sum_{q,\overline{q}} e_q^2 z_1^2 z_2^2 D_1^{q}(z_1, M^2_{1,2}) D_1^{\overline{q}}(z_2, M^2_{3,4})\right]}. \quad (3.13)$$

where z_1 is the fraction of the total energy carried by the h_1h_2 hadron-pair and z_2 is the fraction of the total energy carried by the h_3h_4 hadron pair. The invariant mass of the pair h_1h_2 is $M_{1,2}$ and the invariant mass of the pair h_3h_4 is given by $M_{3,4}$.

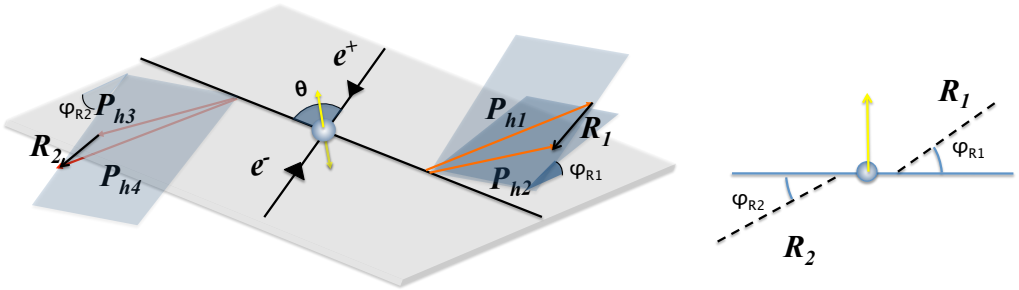

Figure 3.3: Graphical representation of the $e^+e^- \to h_1h_2h_3h_4$X reactions and definition of ϕ_{R1} and ϕ_{R2}.

The measurement of the asymmetry given in eq. 3.13 is fundamental for the extraction of the transversity PDF, note that from this measurement is not possible to extract the di-hadron fragmentation function because the asymmetry depends on their product and the unpolarized fragmentation functions are unknown. Several model calculations exist for the di-hadron FF. The first model for the two pion di-hadron FF was presented in [41], where the phase difference between s and p waves was taken from $\pi\pi$ phase shifts in elastic scattering. The resulting fragmentation function changes sign around the ρ mass. A more recent model has been presented in [42] in which the fragmentation functions are expanded in Legendre polynomials of cos θ. The θ angle is defined in the centre-of-mass system frame of the two hadrons

as the angle between the direction of the positive hadron and the direction of the total momentum of the hadron pair $\boldsymbol{P}_{2h}$ (see fig. 3.4). The $\boldsymbol{R}_T$ and ξ variables in eq. 3.10 are related to the θ angle by the relations $|\boldsymbol{R}_T|=|\boldsymbol{R}|\sin\theta$ and $\xi = 2(|\boldsymbol{R}|/M_{inv})\cos\theta$. The two FFs in eq. 3.10, keeping only the first few terms (the truncation is expected to be legitimate for not very large hadron pair invariant mass), become:

$$\begin{aligned} D_1(z_{2h}, cos\theta, M^2_{inv}) &= D_1^0(z_{2h}, M^2_{inv}) + D_1^{sp}(z_{2h}, M^2_{inv})cos\theta + D_1^{pp}(z_{2h}, M^2_{inv}) \\ &\quad \times \frac{1}{4}(3cos^2\theta - 1), \\ H_1^{\sphericalangle}(z_{2h}, cos\theta, M^2_{inv}) &= H_1^{\sphericalangle sp}(z_{2h}, M^2_{inv}) + H_1^{\sphericalangle pp}(z_{2h}, M^2_{inv})cos\theta. \end{aligned} \tag{3.14}$$

In these equations D_1^0 represents a diagonal component which takes into account all the contributions from s and p waves of the di-hadron system separately, D_1^{sp} and $H_1^{\sphericalangle sp}$ originate from the interference of a s and p wave; D_1^{pp} and $H_1^{\sphericalangle pp}$ arise from the interference of two p waves. In this model the main contributions to the production of a $\pi^+\pi^-$ pair come from: (1) incoherent fragmentation, $q \to \pi^+\pi^-$X; (2) fragmentation via a ρ resonance, $q \to \rho$X$\to \pi^+\pi^-$X; (3) fragmentation via a ω resonance decaying into three pions, $q \to \omega$X$\to \pi^+\pi^-\pi^0$X. Pions in channel 1 are expected to be mostly produced in s wave; pions in channel 2 come from the two-body decay of a vector meson and are in a relative p wave; pions in channel 3 are prevalently in p wave, but a fraction of them may also be in s wave. The functions D_1^{sp} and $H_1^{\sphericalangle,sp}$ arise from the interference of channels 1-2 and 1-3. A model based on a more sophisticated analysis of the fragmentation channels [43] predicts a behaviour for $H_1^{\sphericalangle,sp}$, with a peak at the ρ mass and a broader maximum at the ω mass, a further development of the model in [43] can be found in [44]. The comparison of our results with the predictions obtained using this model will be shown and discussed in sec. 6.3.

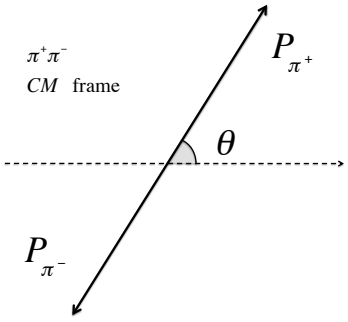

Figure 3.4: Definition of the θ angle which is defined, in the hadron pair centre-of-mass, as the angle between $\boldsymbol{P}_{\pi^+}$ and the total momentum of the hadron pair $\boldsymbol{P}_{2h}$.

A simple qualitative model of the one-hadron and two-hadron production is provided by the "recursive string model" [45, 46, 47] which is illustrated in fig. 3.5. With reference to the figure the massive initial string breaks and a pair is produced. The pair is assumed to be in the $^3P_0$ state, which has the vacuum quantum number L=1.

This process can be interpreted as the fragmentation of the initial quark q_0, polarized in the $+\hat{y}$ direction, into a pion which contains the antiquark $\overline{q}_1$ created by the string breaking. Due to the angular momentum conservation the pion, inheriting the transverse momentum of $\overline{q}_1$, moves in the $+\hat{x}$ direction. The quark q_1, with the sub-leading pion that contains it, moves in opposite direction. This model predicts opposite Collins asymmetries for π^+ and π^- assuming u dominance and a positive (negative) sign for the favoured (unfavoured) Collins function. "Favoured" refers to the fragmentation of a quark or an antiquark belonging to the valence component of the final hadron, e.g. $u \to \pi^+, d \to \pi^-, \overline{d} \to \pi^+$, etc. As shown in fig. 3.5, the process is recursive and the Collins asymmetries are of opposite sign for a sequence of pseudiscalar mesons. The transverse component of the momentum of the quarks k_T decrease along the string, therefore the signal is carried by the hadrons with higher trasverse momentum. This fact suggests to evaluate the asymmetries considering the hadrons with larger z. This model can be applied to the two-hadron production, considering that also in this case the signal is carried by the pairs with larger trasverse momentum. However for this case no quantitative calculations exist yet.

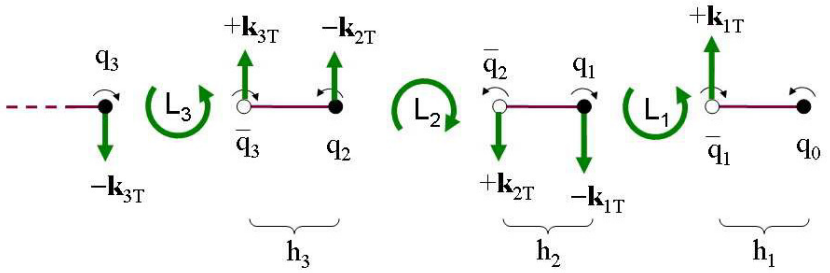

Figure 3.5: The fragmentation process in the recursive string model. The $+\hat{y}$ direction is out of the page and the $+\hat{z}$ direction is along the string [47].

3.3 Experimental overview

3.3.1 Collins Asymmetry

The measurement of the Collins asymmetry in SIDIS has been performed by the HERMES (DESY), COMPASS (CERN), and HallA (JLab) experiments. These experiments cover different kinematical ranges and the measurements have been performed with different targets. In the following, to simplify the notation, we will use z to indicate z_h, in the case of one-hadron production processes, and z_{2h} in the case of two-hadron production processes.

The HERMES collaboration has taken data with a transversely polarized proton target from 2002 to 2005 and published the first results in 2005 [48]. HERMES has used a positrons beam of 27.6 GeV and a gaseous polarized hydrogen target. The HERMES mean $\langle Q^2 \rangle$ value is 2.5 $(\mathrm{GeV/c})^2$. The Collins asymmetries measured for charged π and K are shown in fig. 3.6 [49]. The results show a clear positive signal for π^+ and a negative signal for π^- as a function of x, z and the transverse momentum

of the hadron $\boldsymbol{P}_{hT}$. This trend is confirmed for K^+ but with a strength which increases by a factor of two with respect to that obtained for positive pions. The trend of asymmetry for K^- seems to be opposite with respect to that obtained for negative pions but, due to the large statistical error, it is not possible to conclude that the signal is different from zero. The HERMES results represented the first indication for a non zero transversity PDF and Collins FF.

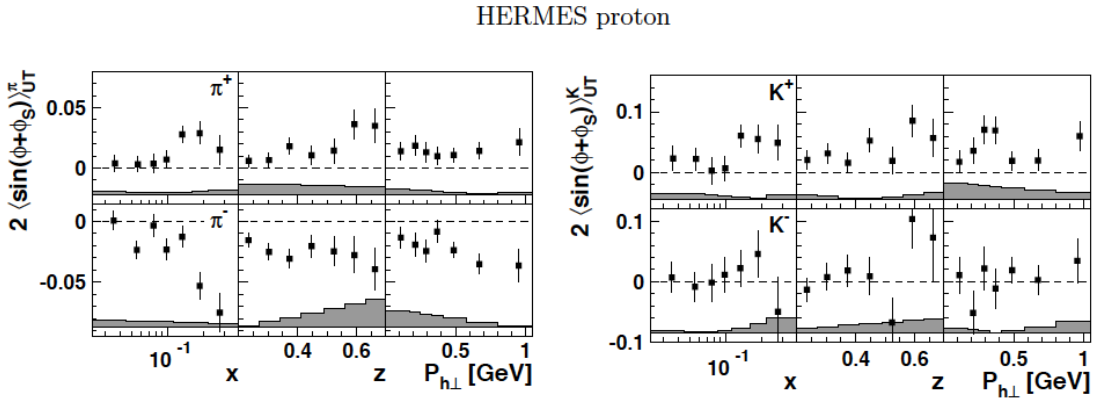

Figure 3.6: Collins asymmetry measured by HERMES ($\langle Q^2\rangle$ =2.5 (GeV/c)^2) for π^+,π^- (left), K^+ and K^- (right) on transversely polarized proton target as function of x, z and $P_{h\perp}$ (P_{hT} in the conventions of this thesis) [49].

In 2002, 2003 and 2004 COMPASS collected data with positive muon beam of 160 GeV off a transversely polarized deuteron target (^{6}LiD). The COMPASS mean $\langle Q^2\rangle$ value is 3.8 (GeV/c)^2. The Collins asymmetries on deuteron [50, 51, 52], shown in fig. 3.7 have been found to be compatible with zero for charged hadrons, for pions and for kaons. The product of the Collins FFs has been measured by Belle collaboration [40]. The Belle mean $\langle Q^2\rangle$ value is 100 (GeV/c)^2. The measurement has been performed using two different methods namely $cos(\phi_1 + \phi_2)$, discussed in the last section, and $cos(2\phi)$. The results shown in fig. 3.8 exhibit a signal different from zero for both methods.

The COMPASS deuteron and the HERMES proton results can be explained as a transversity function different from zero, with opposite sign for the u and d quark and a favoured and unfavoured Collins FF with opposite sign. In fact these first data, together with the Belle results, have been used to extract with a global fit the transversity and the Collins functions [53, 54]. The first results obtained for transversity PDF are shown in fig. 3.9 and the results obtained for the Collins FF are shown in fig. 3.10. As can be seen, the transversity PDFs for the u and d quark have opposite sign as for the helicity, and are well inside the Soffer band. The Collins FFs have almost the same size and again opposite sign.

In spite of the relevance of this first extraction, which is a milestone in this new field, the question of the different Q^2 range of the COMPASS and HERMES measurements was still an open point.

Clearly, a measurement on a transversely polarized proton target at COMPASS

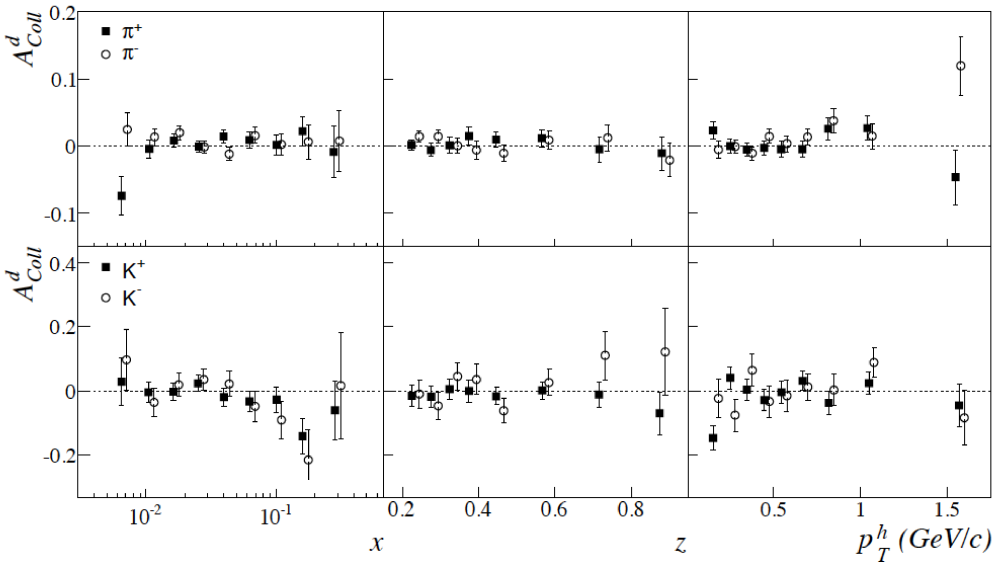

Figure 3.7: Collins asymmetry measured by COMPASS ($\langle Q^2 \rangle$ =3.8 (GeV/c)^2) for π^+,π^- (top) ,K^+ and K^- (bottom) on deuteron transversely polarized deuteron target as function of x, z and P_{hT} [52]. The error bars are the statistical errors.

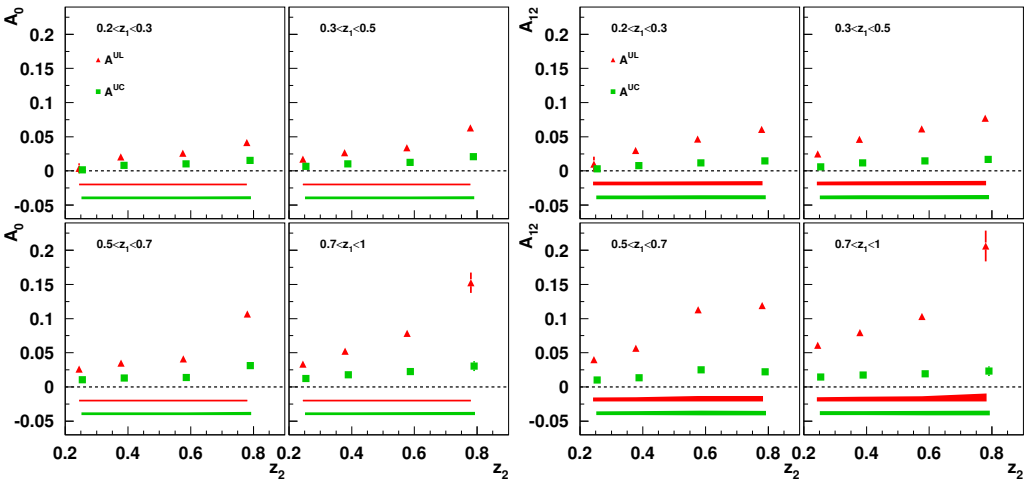

Figure 3.8: The Collins asymmetries in e^+e^- measured by Belle ($\langle Q^2 \rangle$ =100 (GeV/c)^2) [40] as function of z_2 in different bins of z_1 with the $cos2\phi$ (left) and $cos(\phi_1 + \phi_2)$ (right) method.

was needed to investigate the possible relevance of higher twist effect at HERMES.

COMPASS has collected the first data with a transversely polarized proton target (NH_3) in 2007 . The results were published in 2010 [57] and part of this thesis work was dedicated to the finalization of that analysis. The Collins asymmetry is shown in fig. 3.11 as function of x, z and P_{hT} for positive and negative hadrons. It is clearly different from zero in agreement with the hypothesis of an *up-down* quarks cancellation in the deuteron target.

The asymmetries measured by COMPASS and HERMES have the same ampli-

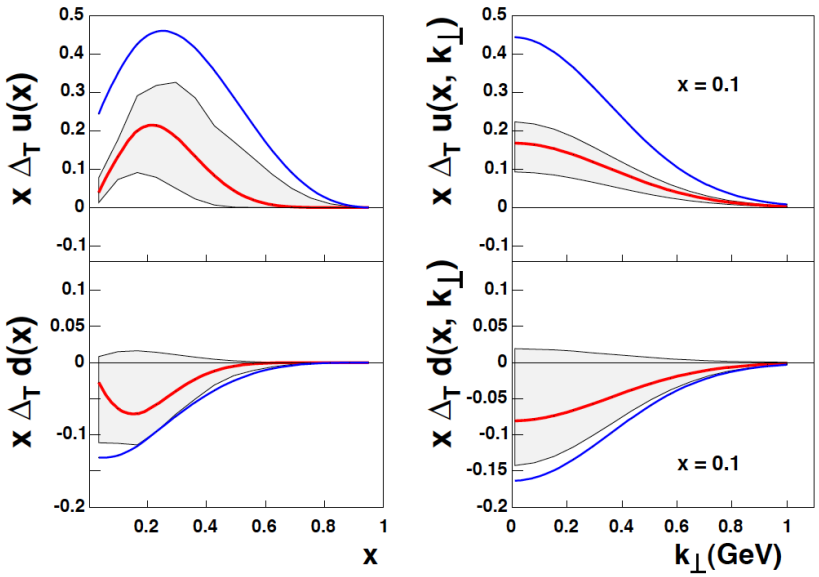

Figure 3.9: The transversity distribution functions $\Delta_T q(x)$ ($h_1^q(x)$ in the conventions of this thesis) for u (top) and d (bottom) quarks integrated over $k_\perp$ (p_T in the conventions of this thesis) (left) and unintegrated (right) and evaluated at $Q^2 = 2.4$ $(\mathrm{GeV/c})^2$. The bold blue line represents the Soffer bound [56] and the shaded area represents the uncertainty due to the uncertainty in the determination of the free parameters [53].

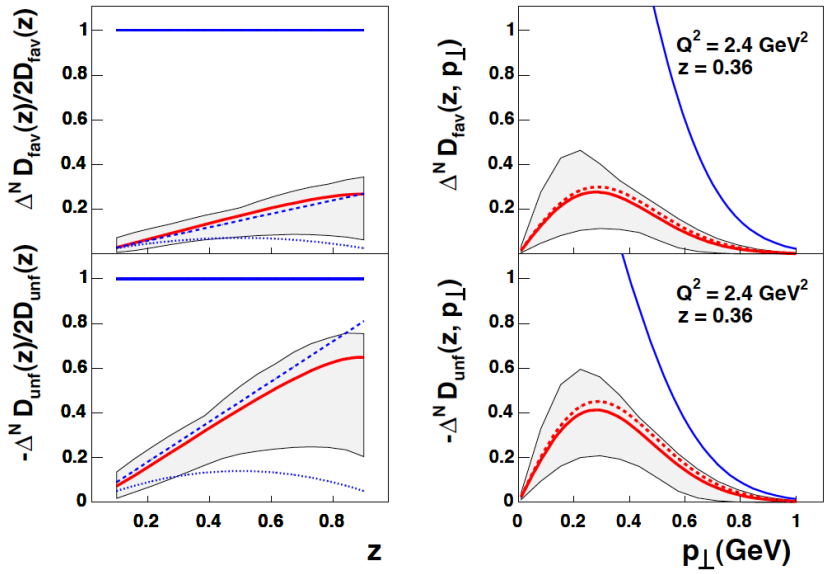

Figure 3.10: In the left are shown the favored and unfavored Collins FFs $\Delta^N D(z)$ ($H_1^q(z)$ in the conventions of this thesis) as function of z and normalized to twice the corresponding unpolarized fragmentation functions. The results are compared with the results of [54] (dashed line) and [55] (dotted line). In the right are shown the $p_\perp$ (k_T in the conventions of this thesis) dependence of the Collins functions at a fixed value of z and at $Q^2 = 2.4$ $(\mathrm{GeV/c})^2$ [53]. The solid lines show the results obtained considering the $cos2\phi$ Belle results while the dashed ones show the results obtained considering the $cos(\phi_1 + \phi_2)$ Belle results [40] .

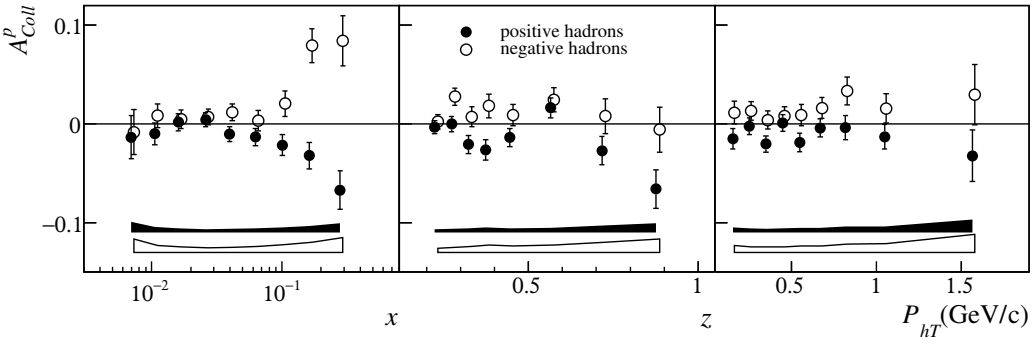

Figure 3.11: Collins asymmetry measured by COMPASS ($\langle Q^2 \rangle$ =3.8 (GeV/c)^2) for unidentified particles (mainly π^+,π^-) on transversely polarized proton target from the 2007 data [57] as function of x, z and P_{hT}. The error bars are the statistical errors and the bands show the systematic errors .

tude once the HERMES data are corrected for the D_{NN} factor, and the difference in sign is due to the different convention used in the definition of the Collins angle. This result give important information on the kinematical dependencies of the transversity PDF and Collins FF. An even more precise measurement has been performed by COMPASS in 2010 [58]. It confirms the measurement of the 2007 data, and will be described in the next chapters.

Very recently the JLab-HallA experiment E06-010 has measured single spin asymmetries with a 6 GeV electron beam off a polarized Helium target for positive and negative pions [59]. The Collins asymmetries on Helium, shown in fig. 3.12, are compatible with zero as expected from the fit of the HERMES proton and the COMPASS deuteron data.

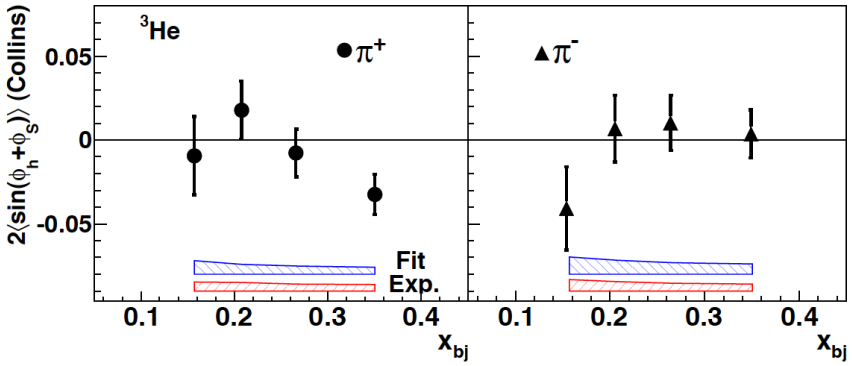

Figure 3.12: ^{3}He Collins asymmetry for π^+ and π^- as function of x measured by JLab-HallA experiment [59].

3.3.2 Two-hadron Asymmetries

The two-hadron asymmetry measurement has been performed by HERMES [60] for π^+ π^- pairs using the data collected in 2002-2005 off the transversely polarized

proton target. The results shown in fig. 3.13 gave evidence for a non zero di-hadron FF . The statistical errors are large and no particular trend can be seen as function of x, z and M_{inv} for $\pi^+\pi^-$ pairs in the measured range. These results have been used in [61] to tune the di-hadron FF calculations, and a very good agreement was obtained. Still, there was the need for more precise data in order to test the model caluclations and investigate the possibility to extract the transversity PDF from this channel.

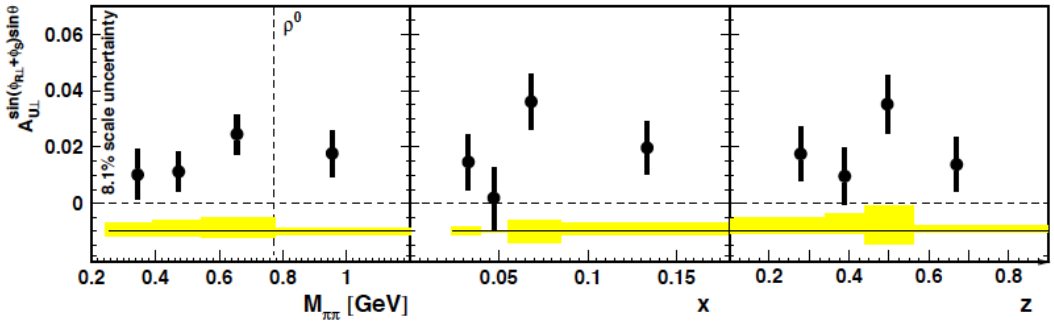

Figure 3.13: Two-hadron asymmetry measured by HERMES ($\langle Q^2\rangle$ =2.5 (GeV/c)^2) for π^+,π^- pairs on a transversely polarized proton target as function of x, z and $M_{\pi\pi}$ (M_{inv} in the conventions of this thesis)[60].

COMPASS measured the two-hadron asymmetry from the deuteron data collected in 2002, 2003 and 2004. Preliminary results have been produced [62] and they are about to be published just now. All the measured asymmetries obtained for all opposite charged hadron pairs, for identified charged hadrons, ordering the hadron by increasing z_i and P_{Ti}, turned out to be compatible with zero within the few percent statistical errors. Also in this case, the small asymmetries on deuteron can be explained as cancellation between the u and d quark contributions. The results obtained for unidentified charged particles as function of x,z and M_{inv} are shown in fig. 3.14.

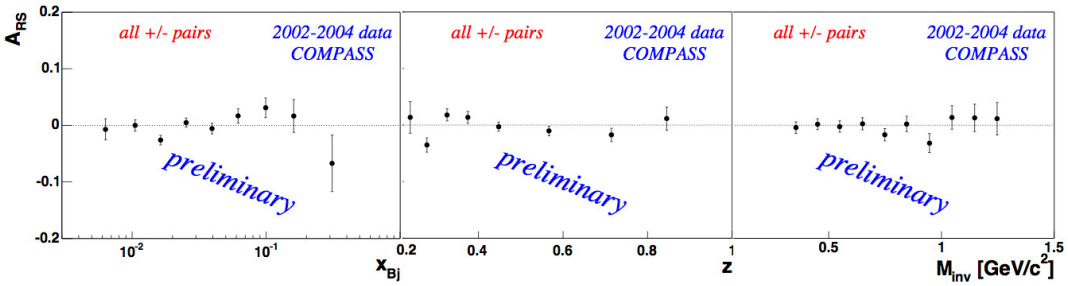

Figure 3.14: Two-hadron asymmetries from the COMPASS ($\langle Q^2\rangle$ =3.8 (GeV/c)^2) 2002, 2003 and 2004 deuteron data for charged particles as function of x,z and M_{inv} [62]. The error bars are the statistical errors.

The two hadron asymmetries from the 2007 COMPASS data [63] collected with the transversely polarized proton target are shown in fig. 3.15. As can be seen, as

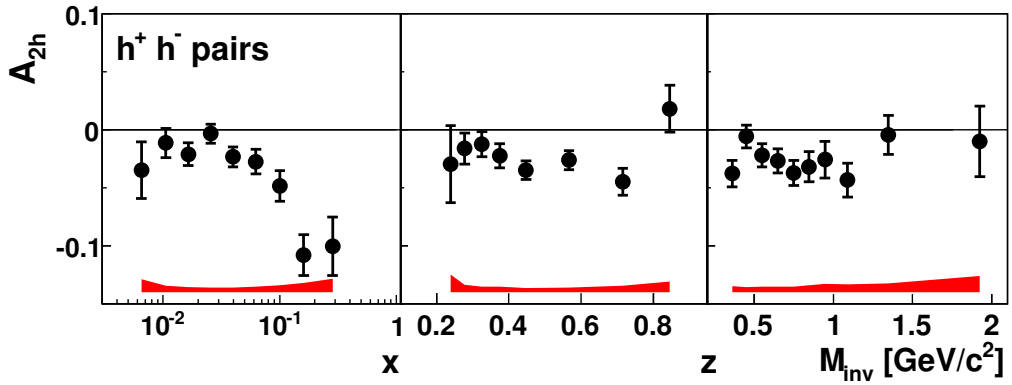

Figure 3.15: Two-hadron asymmetries from COMPASS ($\langle Q^2 \rangle$ =3.8 (GeV/c)^2) 2007 proton data for charged particles as function of x,z and M_{inv} [63]. The error bars are the statistical errors and the bands show the systematic errors.

in the case of the deuteron data, the measurement has a high precision over a large x, z and M_{inv} range and improves considerably the experimental situation. These results show a large asymmetry up to 5-10% in the valence x-region, as large as the Collins asymmetry [63, 57]. The z and invariant mass dependences are not really clear. More informations comes from the COMPASS measurement in the 2010. The analysis of these data is the central part of this thesis, and the results will be presented and discussed in chapter 6.

The measurement of the azimuthal asymmetries for charged pion pairs in $e^+e^- \rightarrow h_1h_2h_3h_4X$ (see eq. 3.13) has been performed at Belle [64]. The results of this measurement (obtained with the $cos(\phi_1 + \phi_2)$ method) as function of z_1 in different z_2 bins (where z_1 is the fraction of energy carried by the h_1 - h_2 hadron pair and z_2 is the fraction of energy carried by the h_3 - h_4 hadron pair) are shown in fig. 3.16. As can be seen the asymmetries are clearly different from zero and increase almost linearly with z_i.

The results for the 8×8 M_1,M_2 binning (where M_1 is the invariant mass of the h_1 - h_2 hadron pair and M_2 is the invariant mass of the h_3 - h_4 hadron pair) as a function of M_2 for the M_1 bins (obtained with the $cos(\phi_1 + \phi_2)$ method) are shown in fig. 3.17. As function of M_i the asymmetries increase from 0.4 GeV/c^2 to 0.8 GeV/c^2 and they are constant for higher invariant mass.

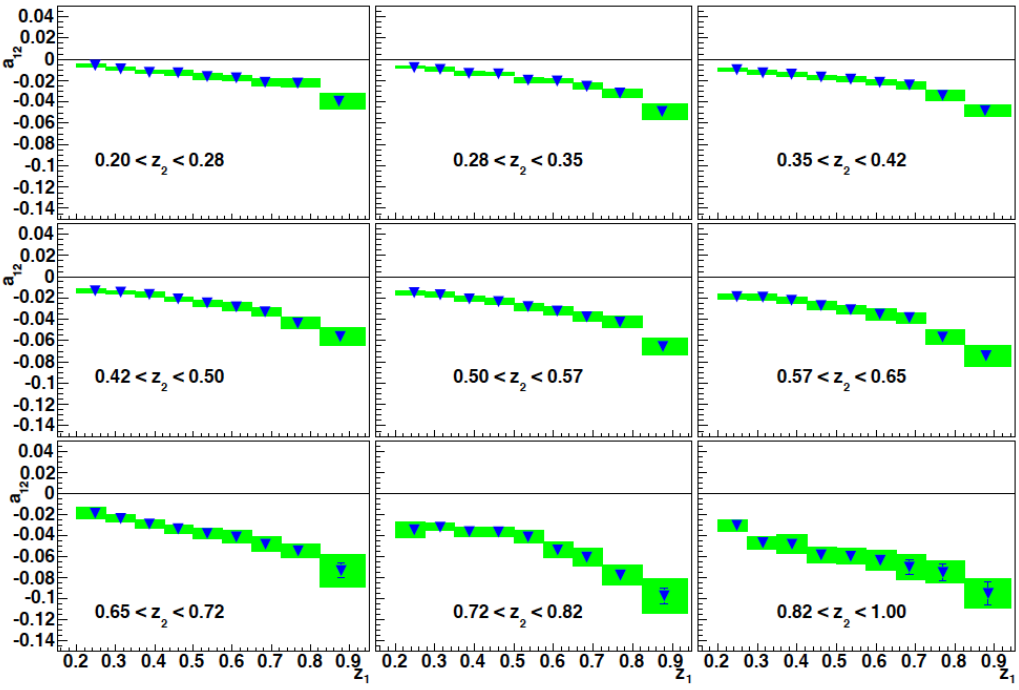

Figure 3.16: $a_{12}(z_1,z_2)$ ($A(z_1,z_2)$ in the conventions of this thesis) asymmetries measured at Belle ($\langle Q^2\rangle$ =100 (GeV/c)^2) for the 9 × 9 z_1, z_2 binning as a function of z_1 for the z_2 bins. The shaded (green) areas correspond to the systematic uncertainties.

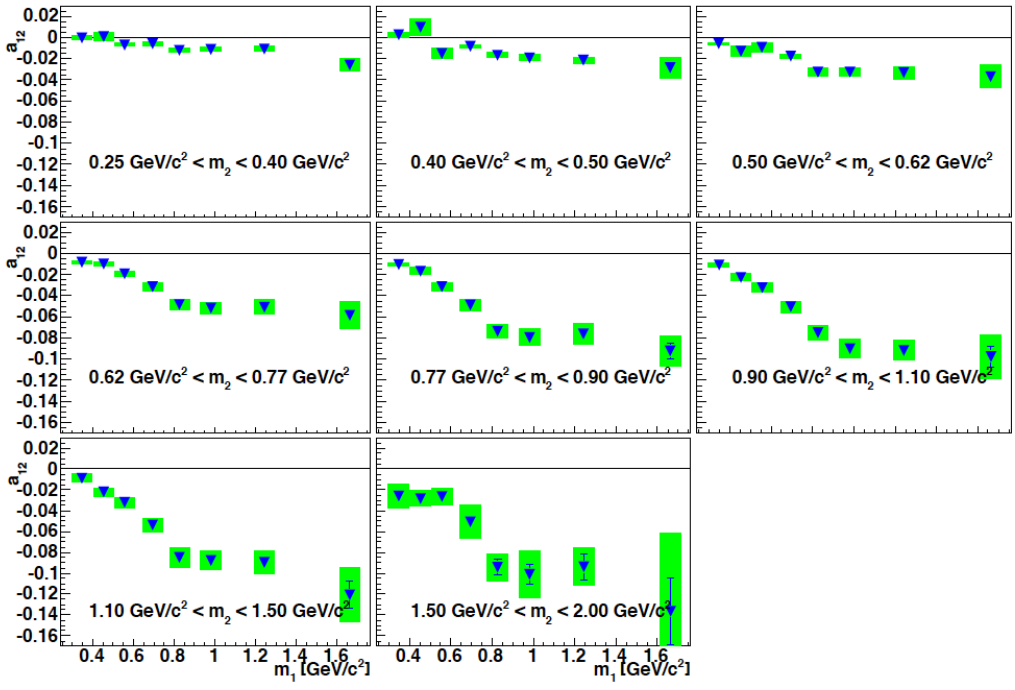

Figure 3.17: $a_{12}(m_1,m_2)$ ($A(M_1, M_2)$ in the conventions of this thesis) asymmetries measured at Belle ($\langle Q^2\rangle$ =100 (GeV/c)^2) for the 8 × 8 m_1,m_2 binning as a function of m_2 for the $m_1$bins. The shaded (green) areas correspond to the systematic uncertainties.

Chapter 4

The COMPASS experiment

The COMPASS experiment is a fixed target experiment of the CERN SPS whose main purpose is the investigation of the nucleon spin structure and the hadron spectroscopy. The projects for the measurements of the nucleon structure and hadron spectroscopy were initially proposed independently in 1995 as two different experiments [65]. Thanks to the existence of the CERN M2 beam line, that can deliver either muons or hadrons beams of high quality, these two initiatives have been merged into a unique project. This merging process required to approach many technical and conceptual difficulties and resulted in a very flexible and versatile setup [66]. The COMPASS spectrometer (fig. 4.1) consists of three main parts: the detectors upstream the target, the Large Angle Spectrometer(LAS) and the Small Angle Spectrometer (SAS). In this chapter the 2010 setup will be described, when a muon beam has been used impinging on a transversely polarized proton target. In the last two sections the off-line system and the event reconstruction will be described.

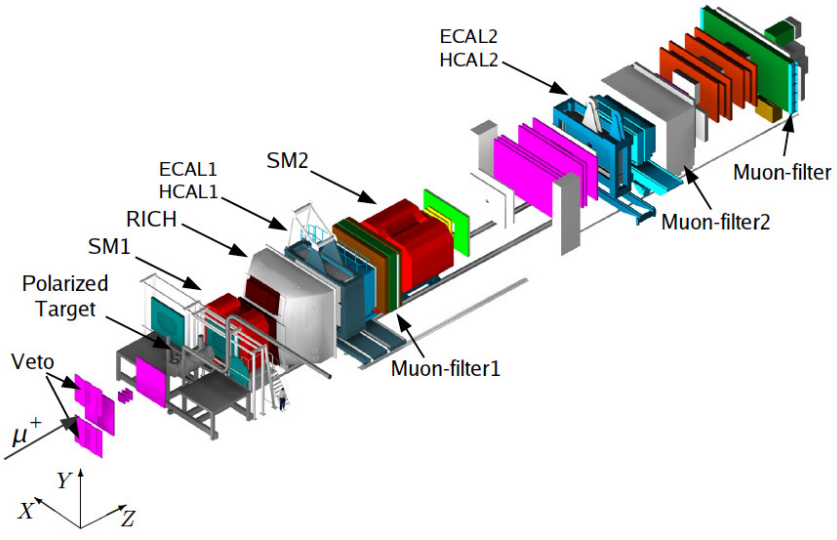

Figure 4.1: Artistic view of the COMPASS spectrometer.

4.1 General overview

The muon beam is transported to the experimental hall in a long ($\sim$ 1 Km) beam line. This first part of the spectrometer is composed by different elements that are used for three fundamental tasks: the beam momentum measurement, the beam tracks reconstruction and the rejection of the beam-halo. The momentum measurement is done event by event by the Beam Momentum Station (BMS) located along the beam line 100 m upstream of the experimental hall. The beam tracks reconstruction is provided by fast trackers located upstream of the target. Scintillator veto counters define the beam spot size and separate the beam by the beam-halo. The second part of the spectrometer,the Large Angle Spectrometer, is built around the SM1 magnet and is planned to ensure 180 mrad polar acceptance. SM1 is a dipole magnet located 4m downstream of the target centre; it is 110 cm long with a vertical size that matches the required angular acceptance of $\pm$180 mrad. The magnet field is vertical in the medium plane, and downward oriented. It has a bending power of 1.0Tm, that corresponds to a deflection of 300 mrad for particles with a momentum of 1 GeV/c. The deflection imposes an angular acceptance of the detectors located downstream of SM1 of $\pm$250 mrad in the horizontal plane. The SM1 magnet is preceded and followed by detectors for the track reconstruction and is followed by a RICH detector with a large transverse dimensions to match the LAS acceptance requirement. The RICH is used to identify charged particles with a momentum from a few GeV/c to $\sim$50 GeV/c. The LAS is completed by a large hadron calorimeter (HCAL1) with a central hole matching the second spectrometer acceptance, and an electromagnetic calorimeter (ECAL1) to select low energy π^0. The HCAL1 is used to detect the outgoing hadrons and to trigger the events. The last detector of the LAS is the muon filter. The third part of the spectrometer, the SAS, has been designed to detect particles at small angles ($\pm$30 mrad) and large momenta, at least 5 GeV/c. The central element of the SAS is SM2, a dipole magnet 4 m long located 18 m downstream of the target centre and preceded and followed by telescopes of trackers. As for SM1 the SM2 main field component is in the vertical direction, with a bending power of 4.4Tm. The downstream part of the SAS includes electromagnetic and hadron calorimeters and a muon filter. The electromagnetic calorimeter (ECAL2) is used to detect gammas and neutrals pions, while the SAS hadron calorimeter is used, as for LAS, to detect and characterize hadrons. In the following the laboratory system described in fig. 4.1, with the z-axis parallel to the nominal beam direction, will be take into account. In fig. 4.2 is shown the COMPASS spectrometer in detail.

4.2 The beam line

To produce the beam in the M2 beam line the very intense primary proton beam is extracted from the CERN SPS at 400 GeV/c momentum, and a Beryllium target with 500 mm thickness (T6). The secondary hadrons produced in these interactions are mainly pions with a contamination of Kaons of about 3.6%. The pions are transported along 600 m through focusing and defocusing (FODO) quadrupoles. Along this way a fraction of pions decays in a muon and a neutrino.The muons produced in this decay are polarized due to the the parity violating nature of the

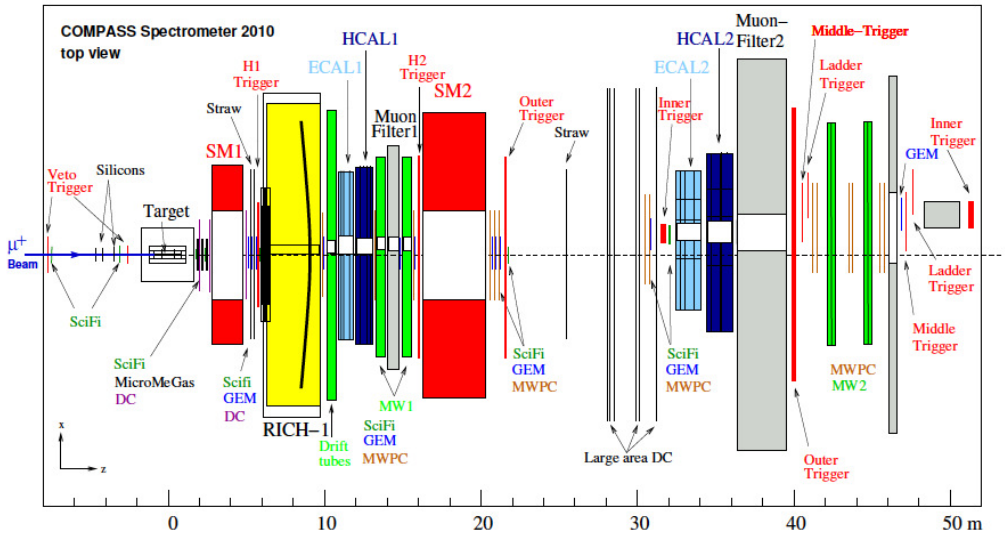

Figure 4.2: COMPASS spectrometer in 2010 setup.

decay; the average polarization of the beam is $\sim 80\%$. At the end of the transport line 9 motorised modules of Beryllium, 1.1 m long each, absorb all the pions which had not decayed. The filtered muons are deflected by 24 mrad by many magnets for a good momentum definition. After a further cleaning and momentum selection the muon beam is transported to the surface level by a second 250 m long FODO channel. The final part of the beam line is used to focus the beam on the polarised target and to measure the beam momentum. This part consists of three dipole magnets, 4 hodoscopes and 2 scintillating fibers, as well as several quadrupoles and dipoles used to fine-steer the beam and to compensate the horizontal deflection due to the 0.42 T transverse dipole field of the polarized target. The momentum of the muon can be at most 190 GeV/c with a momentum spread usually between $\pm 3\%$ and $\pm 5\%$ RMS. The choice of the beam momentum value is related to the statistical figure of merit of COMPASS experiment which is proportional to the beam intensity and to the square of the muon polarization. The radio-protection guidelines impose a maximum beam flux of $2 \cdot 10^8$ per spill. All momenta between 80 and 160 GeV/c achieve this flux value, as visible in fig. 4.3, so for standard COMPASS data taking has been selected a beam momentum of 160 GeV/c. The primary beam is extracted from the SPS for 4.8 s, each extraction interval is called *spill*. The muon beam intensity of $2{\cdot}10^8$ muons per spill is obtained with a proton flux of $1.2 \cdot 10^{13}$ protons per spill. The momentum of each individual muon is measured by the Beam Momentum Station (BMS) (fig. 4.4) that is a detector composed by three consecutive dipole magnets (B6) surrounded by a system of four quadrupoles, four scintillator hodoscopes (BM01-BM04) and two scintillating fibre hodoscopes (BM05-BM06). The BMS measures the beam momentum with a precision $<1\%$ and with a track reconstruction efficiency of 93%. The muon beam has a large halo-beam component. The outer part of the halo is measured by a large veto counter with a surface of 2.50×3.20 m^2 and a hole of 30×30 cm^2 in the middle. It amounts to about 7% of the nominal muon beam. A second veto counter, the inner veto, has

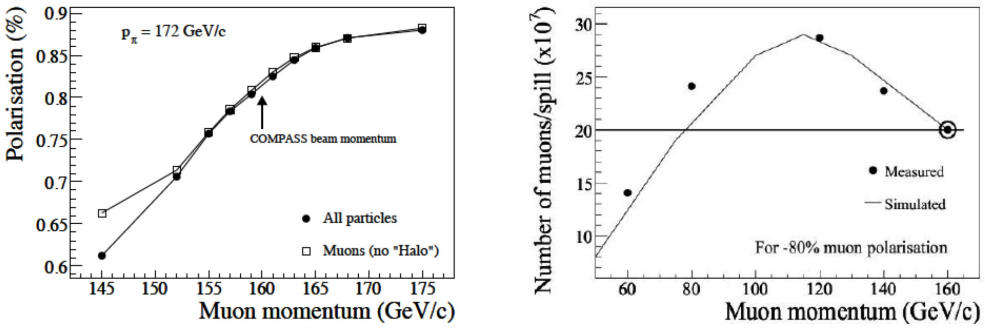

Figure 4.3: The muon beam polarization as a function of the muon beam momentum, assuming a central hadron momentum of 172 GeV/c (left). The maximum muon flux per SPS cycle as a function of the muon momentum, assuming a p_μ/p_πratio corresponding to -80% positive muon polarisation.

a smaller surface (30 × 30 cm^2) and a hole of 4 cm of diameter in the middle, and detects the tails of the beam distribution. It counts about 16 % of the muon beam. The beam tracks are reconstructed by the detectors located in front of the target and back-propagate from the target region to the BMS. The spatial correlation between the extrapolated tracks and the BMS hits is used to resolve eventual ambiguities when there is more than one beam candidate.

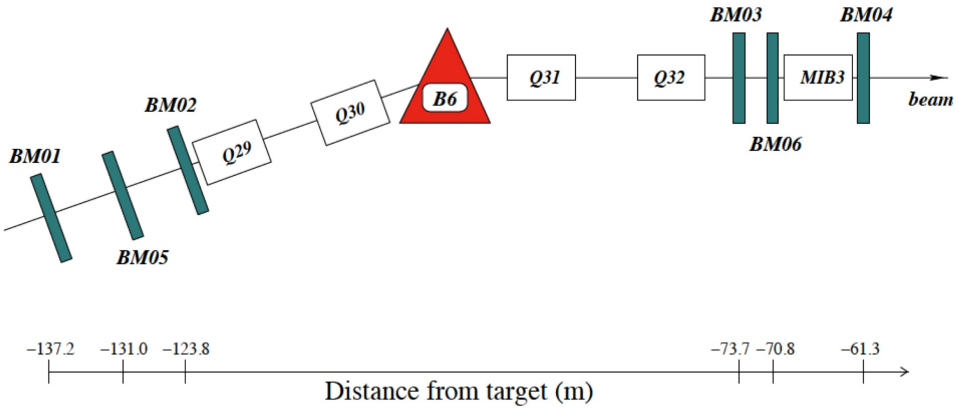

Figure 4.4: Layout of the Beam Momentum Station for the COMPASS muon beam.

4.3 The polarised target

The measurement of cross section asymmetries is the aim of the muon program. The corresponding observable is $A \propto P_T\ f\ \Delta\sigma$ where $\Delta\sigma$ is the difference between

the cross sections of a process for two different spin configurations, P_T is the target polarization and f is the dilution factor, i.e. the fraction of polarizable material inside the target. The use of polarized target is mandatory to obtain two different spin configurations and the factors P_T and f must be as large as possible to optimize the statistical significance of the measurements. Due to the smallness of the nucleon magnetic moment, the nucleon spin polarization is not so easy to be obtained. While the electron spins can be aligned in a strong magnetic field and for a low enough temperature, only a negligible nuclear spin polarisation can be reached. This is the reason why the dynamic nuclear polarisation (DNP) method is used to polarize solid state targets. In this process the electron polarisation is transferred to the nuclear spins by means of a microwave field [67]. This process requires a material containing some amount of paramagnetic centres ($\sim 10^{-5}$ created for instance by irradiation), a temperature below 1 K and a strong (typically 2.5 T) and homogeneous magnetic field. Taking into account the degree of polarization which can be achieved, the dilution factor and also some additional characteristics as the density of the material, the packing factor of the target material in the target cell, and the spin relaxation time of the spin polarized system, the deuterated lithium (^{6}LiD) and the irradiated ammonia (NH_3) have been chosen as target materials for polarized deuteron and polarized proton targets, respectively, for COMPASS muon program experiments. In deuterated lithium (^{6}LiD), used until 2006, a degree of polarization higher than 40 % can be reached with a very favourable value for f, of the order of 0.35. The irradiated ammonia NH^3 which is used since 2007 as a polarized proton target in COMPASS experiments has a less favourable dilution factor f, about 0.15, but can be polarized to a value higher than 80 %. The target is divided in three cells with diameter of 4 cm (see fig. 4.5). The length of the central cell is 60 cm and the length of each of the two external cells, upstream and downstream cell, is 30 cm. The cells are separated by 5 cm gaps. The central cell material is polarized in opposite direction in comparison with external cells. At COMPASS experiment the spin asymmetries are measured either in the so called " transverse mode", in which the target polarization is orthogonal with respect to the direction of the beam, or in the "longitudinal mode" with the target polarization parallel or anti-parallel to the direction of the beam. To avoid systematic effects due to different geometrical acceptance of the cells the polarization is reversed frequently. The target polarization is monitored with a continuous-wave nuclear magnetic resonance (NMR) system. Several NMR coils are distributed along the target cells to probe different parts of the cells.

The dilution refrigerator

A powerful dilution ^{3}He/^{4}He refrigerator, originally designed and constructed for CERN SMC experiment [68] is used in COMPASS to cool the large amount of polarized target material down to the temperature of about 50 mK and to keep this temperature as long as necessary for the experiment. The large cooling power of the refrigerator can cope with the high amount of microwave power during the DNP process where more than 350mW are used for polarization build up. When the desired polarization is achieved the microwave system is switched off. The temperature of the target decreases to about 50 mK, at which temperature the

spin relaxation time increases considerably (frozen-spin mode).

The COMPASS magnet system

The superconducting magnet system consists of the superconducting solenoid and the dipole coils. The superconducting solenoid has been designed to ensure ± 180 mrad acceptance for the most upstream edge of the polarized target. The solenoid produces a 2.5 T magnetic field along the beam direction. Sixteen correction coils are used to trim the magnetic field and guarantee the required field uniformity inside the whole of the target volume. The solenoid magnetic field is used for longitudinal target polarization . The transverse holding field of 0.62 T is produced by the two dipole saddle shaped coils. This transverse magnetic field is used to keep the target transversely polarized in the transverse mode data taking. Both magnets have their own control systems allowing to set the solenoid and the dipole currents remotely and to perform the rotation of resulting field on the target automatically. The transverse magnetic field is used also to change the target spin orientation in the longitudinal mode. In this case the solenoid field is reversed and the transverse field is used to rotate adiabatically the target polarization. The spin reversal in the longitudinal mode can be achieved in about 33 min. The spin reversal in the transverse mode cannot be performed with the same method used in the longitudinal mode (reversing the holding magnetic field would completely change the geometrical acceptance of the spectrometer) so the polarization is destroyed and the target is polarized again, but in the opposite direction. Of course this process needs more time and is performed in about 36 hours. The difference of time needed to reverse the spin explains why in the transverse mode the polarization is reversed every week while in the longitudinal mode is reversed every day.

4.4 The tracking detectors

The choice of the tracking detector is based on the particle flux expected in its active region and on the requirement that the amount of material along the beam path has to remain a minimum in order to minimise multiple scattering and secondary interactions. These requests are particularly severe in the region upstream of the SM1 magnet where a lot of secondary particles come from the target region. The particle flux per unit transverse surface decreases by five orders of magnitude going from the region closest to the beam to the largest angles accepted by the spectrometer. For this reason, along the beam and close to the target the detectors have a high particle rate capability (MHz/channel) with an excellent space resolution (100 μm), while far from the beam the resolution constraint is relaxed but larger areas must be covered. Different kinds of detectors are employed at different distance from the beam axis and they can be grouped as: Very Small Area Trackers (VSAT), which cover the beam region up to a radial distance of 2.5–3 cm, Small Area Trackers (SAT), which cover the intermediate region at a radial distance of 2.5 cm to 30 – 40 cm and the Large Area Trackers (LAT) which cover the outermost regions.

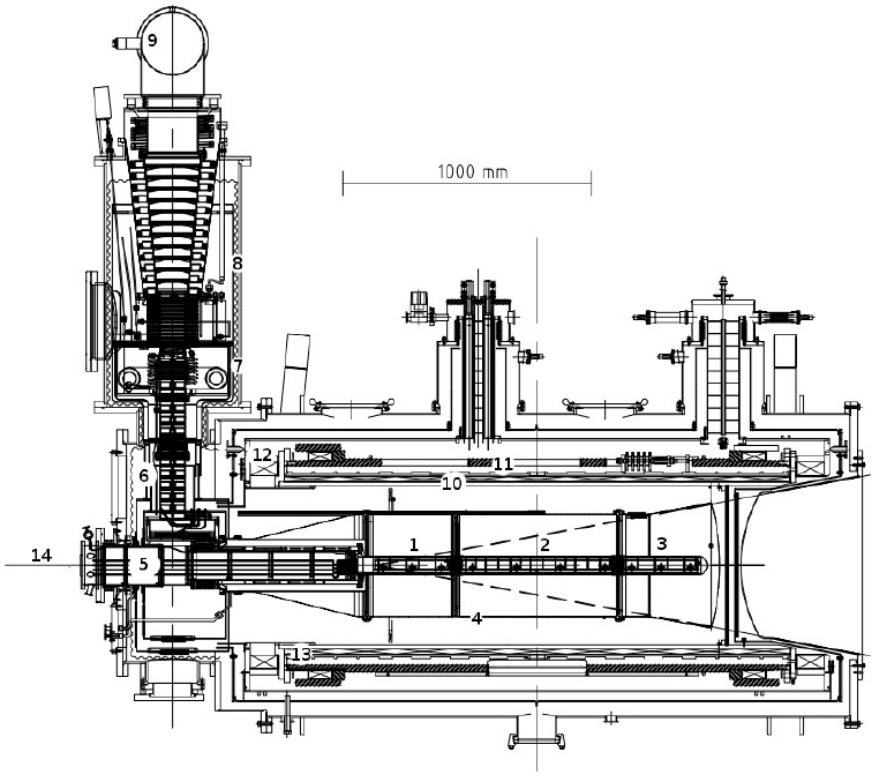

Figure 4.5: Side view of the COMPASS polarized target: upstream (1), central (2) and downstream (3) target cells inside mixing chamber, microwave cavity (4), target holder (5), ^{3}He evaporator (6), 4He evaporator (7), ^{4}He liquid/gas phase separator (8), ^{3}He pumping port (9), solenoid coil (10), correction coils (11), end compensation coil (12), dipole coil (13), muon beam entrance (14). The tree halves of the microwave cavity are separated by a thin microwave stopper.

The Very Small Area Trackers

The detectors used to cover this area must combine high flux capabilities (a flux up to about 10^5 s^{-1} mm^{-2} is expected in the centre of the muon beam) and excellent space resolution: Scintillating Fibres and Silicon Micro-strips have been chosen. Eight scintillating fibre stations are used to detect incoming and scattered beam particles as well as all other charged particles produced in the target; two pairs of stations are placed upstream and downstream of the target, two pairs are placed upstream and downstream of SM2. Each scintillating fibre plane contains several layers of fibres to increase the number of photo-electrons; the geometrical configuration is shown in fig. 4.6. All the fibres on the same "column" are grouped in the same photomultiplier channel. Each station has at least the vertical projection (Y) and the horizontal projection (X). Three stations comprise also an additional projection (U) which is inclined by 45^o with respect to the X axis. The spatial resolution depends on the fibre diameter and varies from 130μm to 210 μm. The time resolution has an r.m.s. value between 350 ps and 450 ps.

Three silicon micro-strip stations are used for the incoming muon beam track

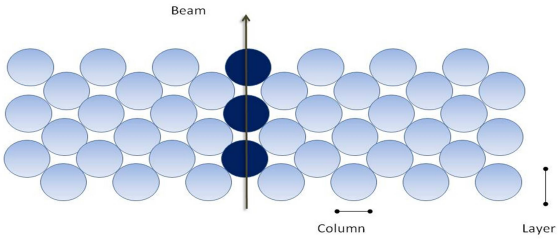

Figure 4.6: Fibre configuration of a SciFi plane.

reconstruction upstream of the target. These detectors consists of an n-type wafer with an active area of 5 × 7 cm^2 and 300 μm thick. The 1280 strips on the n-side (54.6 μm pitch) are perpendicular to the 1024 strips on the p-side (51.7 μm pitch) and give a two dimensional information on the particle position using only one wafer. Each silicon station consists of two detectors which are mounted back-to-back such that one detector measures the horizontal (X) and vertical (Y) coordinates and the other two additional projection (U) and (V) which are rotated by 5^o around the Z axis. The spatial resolution of these detectors is 8 μm on the p-side and 11 μm on the n-side. The average time resolution is 2.5 ns.

The Small Area Trackers

In the SAT three Micromegas (Micromesh Gaseous Structure) stations and 11 GEM (Gas Electron Multiplier) are installed. COMPASS is the first high energy experiment using Micromegas and GEMs. All the three Micromega stations are located in the 1 m long region between the polarised target magnet and the SM1 magnet. Each Micromegas detector plane has an active area of 40 × 40 cm^2 and a central dead zone with 5 cm diameter. The Micromega station is composed by four detector planes assembled in a parallel plate electrode structure. Each detector reconstructs one the four track projections X,Y,U,V where the U and V planes are rotated of +45^o (the U-plane) and -45^o the V-plane respect to the X(Y) plane. Each detector consists of 1024 strips with a strip pitch of 360 μm for the central part of the detector (512 strips) and 420 μm for the outer part (2× 256 strips). The special feature of this detector is the separation of the conversion region from the amplification region by a micromesh. The conversion gas is 3.2 mm thick while the amplification gap is 100 μm thick (fig. 4.7) so the electrical field in the conversion gap is much lower than the electrical field in the amplification gap. The particle ionizes the gas present in the conversion gap and the ions produced drift "slowly" until the mesh where they are accelerate by the high field and form the avalanche. The ions produced in the avalanche are stopped by the mesh so they can drift a maximum distance of 100 μm and the width of the signal induced by the ions by the ions cannot exceed the 100 ns (the drift time corresponding to that distance). The small drift of the ions, the reduced transverse diffusion of the electrons and the high granularity of the detector result in a high rate capability. The mean time resolution is 9.3 ns with a spatial resolution of the order of 90 μm.

Each GEM station consists of two detectors with an active area of 31 × 31 cm^2 and the 11 GEM stations cover a region from the downstream of SM1 to the far end

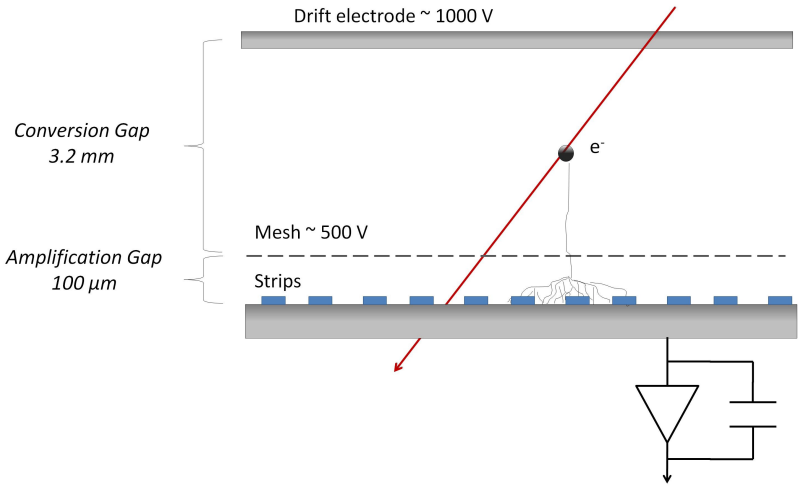

Figure 4.7: Principle of a Micromegas detector.

of COMPASS setup. The GEM consists of a 50 μm thin Polyimide foil which has a large number of micro-holes (about $10^4/\text{cm}^2$) with a diameter of 70 μm. Inserting these foils between the parallel plate electrodes of a gas-filled chamber,an avalanche multiplication is achieved when primary electrons pass across the holes . The electric field guides the electrons until they arrive to the readout anode. As shown in fig. 4.8 the COMPASS GEM detector is composed by three GEM foils separated by 2 mm gaps. The electron avalanche in the last stage of the GEM detector generates a fast signal on the readout anode which consists in two sets of 768 strips with a pitch of 400 μm. Two consecutive plate, each perpendicular to each other and separated by an insulating layer, detect two projections of the track trajectory. Any GEM station is composed by two GEM detector planes whose axis differ by 45 ^{o}. This configuration permits measurements of a charged particle trajectory in four projections. During normal data taking the central zone with a diameter of 5 cm is deactivated lowering the potential across the last GEM foil in order to avoid high occupancies due to the beam flux. This region is activated during the alignment runs, for which the intensity of the beam is lower. The time resolution is about 12 ns and the spatial resolution is 66.4 μm with an average efficiency of 97.2%.

The Large Area Trackers

In the LAS, particles with a large polar angle are detected by three Drift Chambers (DC), three stations of straw drift tubes, fourteen Multi-Wire Proportional Chambers (MWPC) and, in the outer region of the COMPASS setup, two additional straw stations and six very large area drift chambers. Two DC stations are located upstream of SM1 and one downstream of it. All the DCs have an active area of 2.48 $\times$ 2.08 m^2 with a central dead zone of 30 cm diameter. Each DC station is composed by eight layers that measure four different projections of the particle trajectory: vertical (Y), horizontal (X), and rotated of +20^o (U) and -20^o (V) with respect to the vertical direction. Each layer consists of two cathode foil, perpendicular to the beam direction, of 25 μm thickness cladded with 10 μm of graphite and

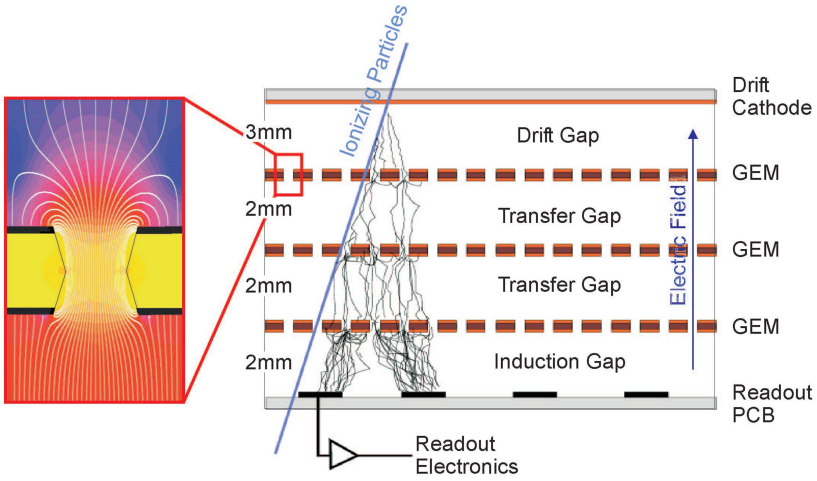

Figure 4.8: Schematic cross section of a triple GEM detector.

filled with gas. Into this layer there are 176 sensitive wires with a diameter of 20 μm alternated with 177 potential wires with a diameter of 100 μm defining a gas gap of 8 mm width. As shown in fig. 4.9 two consecutive layers are staggered by 3.5 mm to avoid the left-right ambiguity on the trajectory of the particle. Each cell is delimited by potential wires and cathode foils and has a size of 8 $\times$ 7 mm^2. The cathode foil, sensitive wires and potential wires are fixed at -1700 V, 0 V and -1700 V, respectively. During data taking, to avoid higher rate near the beam, a central zone with a diameter of 30 cm is deactivated using an independent high voltage supply that vanishes the efficiency in the dead zone. This central area is activated in the alignment runs. The spatial resolution of a single DC wire layer is $\pm$ 270 μm with an efficiency of 95%.

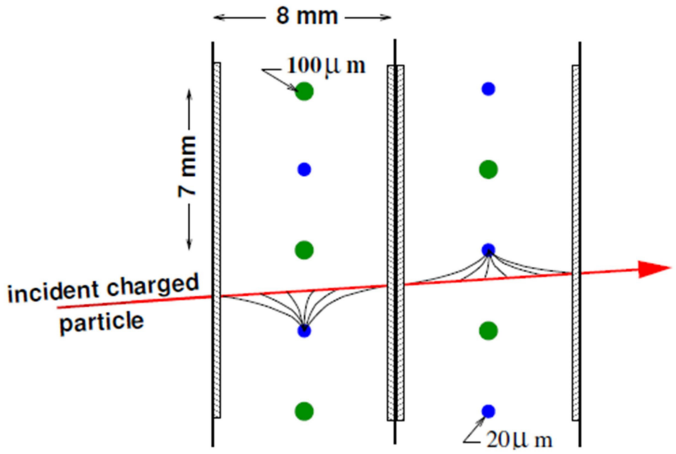

Figure 4.9: Drift cell geometry.

Two stations of straw drift chambers are located upstream of the RICH and one

downstream of the RICH. The polar angle acceptance of these detectors is (15–200 mrad). A carbon layer of 40 μm is glued onto an aluminised foil of 12 μm thickness to made the straw tubes, which have 6 mm diameter in the central part of the detector, and 8 mm diameter in the outer part. The anode consists of a gold-plated tungsten wire with 30 μm diameter. Four small plastic spacers position the anode wire in the centre of the straw tube. Each detector is made by a plane that consists of two layers of straws staggered to avoid the left-right ambiguity. Each station is composed by two planes of size 323 $\times$ 280 cm ^{2} and one plane of size 325 $\times$ 243 cm^2, all with a central dead zone of 20 $\times$20 cm^2; the third plane is rotated of 10^o respect to the vertical. The average resolution of one straw detector (two layers) is 190 μm with an efficiency larger than 99%.

The detection of particles with a large polar angle in the SAS region is done mainly by the MWPC. Each wire is 1 m long and has a diameter of 20 μm; the wire pitch is 2 mm with a cathode/anode gap of 8 mm. The total number of layers installed is 34 corresponding to 25000 detector channels. Three different types of MWPC are present in the COMPASS spectrometer and they are labelled as A, A* and B type. The type-A detectors, with an active area of 178 $\times$ 120 cm^2, have three anode wire layers, one vertical (Y), one tilted by +10.14^o (U) and one by -10.14^o (V) with respect to the vertical axis. The type-A* detectors differ from the type-A detectors only by an additional layer with the wires parallel to the horizontal direction (X). The active area of the type-B is smaller (178 $\times$ 80 cm^2) and they are composed only by two layers, one vertical (Y) and the other rotated of $\pm$10,14 ^{o} (U or V) with respect to the vertical. All wire layers are enclosed from both sides by 10 μm thick graphite coated cathode foil. The central dead zone size of the MWPC depends by the distance of the detector from the target and it is realized removing the graphite coating from the foils; its diameter is included between 16 and 22 mm. The average spatial resolution of the MWPC is 0.6 mm.

The six large area drift chambers installed in the outer region of the spectrometer provide tracking for charged particles which have been deflected by a large angle in the SAS. The active area is 5 $\times$ 2.5 m^2. Each chamber consists of four layers coupled in two planes. Four are composed by X layers coupled with Y,V or U layers, where U and V are tilted respectively of +30^o and -30^o; the other two chambers are of YV-type and YU-type.The dead zone has a diameter of 0.5 m for the XY-type and 1 m for the other all chambers. The average layer efficiency has been measured to be 93 % with a spatial resolution of 0.5 mm.

4.5 Particle identification

The COMPASS spectrometer contains several particle identification detectors. A RICH counter is designed to separate pions, protons and kaons. Two hadron calorimeters are a complementary element in the hadrons triggering process. The measurement of the energy of the photons and electrons is provided by two electromagnetic calorimeters. Finally two muon wall systems are used to identify the scattered muons. Each consists of a hadron absorber enclosed by tracking detectors.

4.5.1 The RICH detector

The COMPASS Ring Imaging Cherenkov (RICH) detector [69] is used to identify particles with momentum between 5 GeV/c and 43 GeV/c. Its large size permits to cover the whole angular acceptance of the LAS ±250mrad in the horizontal plane and ±180 in the vertical plane. The radiator gas used to fill the RICH is C_4F_{10}. The Cherenkov photons are reflected by two spherical mirror surfaces and are detected by MWPCs. The photon detectors are placed outside the spectrometer acceptance and far from the beam line. The two reflecting surfaces, that form the mirror system, are located off beam axis, such that the Cherenkov ring images are focused outside the LAS as shown in fig. 4.10. The photon detector surface (5.6 m^2) is covered by eight special MWPCs whose cathodes have been coated with CsI photon converter layers. CsI have a very good efficiency only for wavelengths smaller than 200 nm so the system is sensitive in the very UV (VUV) domain. The radiator gas and the photon detectors regions are separated by quartz windows. The quartz optical features impose the lower limit of the useful wavelength at ≈ 165 nm.The internal pressure and gas composition are kept constant by a dedicated radiator gas system.

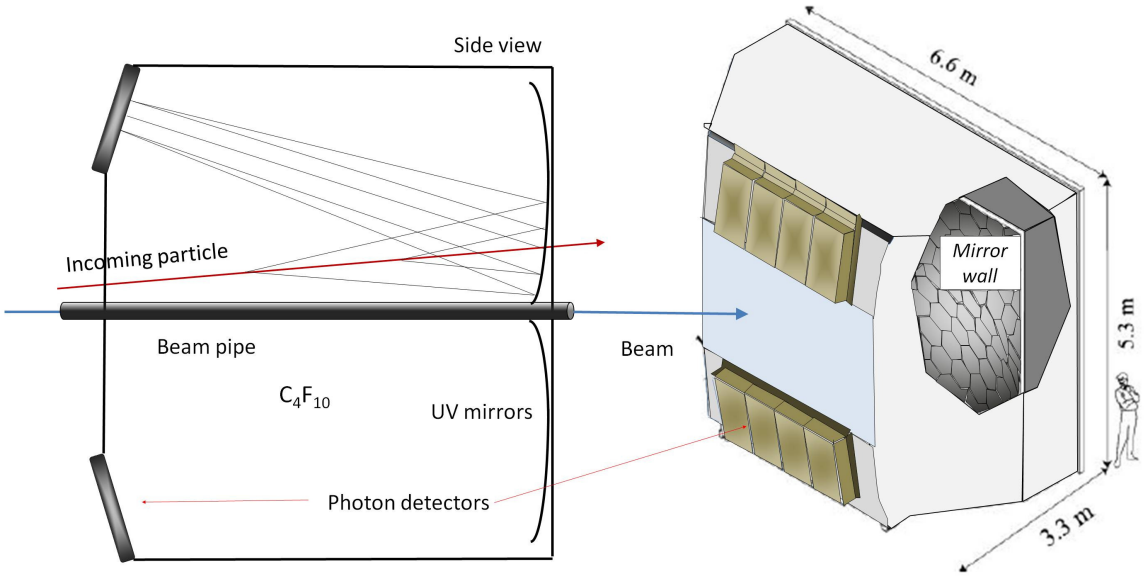

Figure 4.10: A scheme of principle and an artistic view of the COMPASS RICH-1.

The RICH gas system

The RICH radiator gas is contained in a vessel which has a length of 3 m and a volume of 80 m^3. The COMPASS gas system [70] performs different tasks: it

control the internal pressure of the vessel, keeps the gas transparent in the VUV domain and is used to fill and drain the vessel. The internal pressure conditions must be kept controlled because the thin vessel walls can be deformed by a wrong internal pressure. It's important also to purify the gas to reduce as much as possible the contamination by water vapour and oxygen. The transparency is measured on-line using two complementary systems. The purification system guarantees a contamination of less than 1 ppm of water vapour and 3 ppm of O_2.

The RICH mirror system

The RICH optical system [71] consists of two VUV reflecting spherical surfaces of 21 m^2 with a radius of curvature of 6600 mm. The Cherenkov photons are focused on the photon detectors which are placed on a plane surface that is a rough approximation of the spherical focal surface. The two mirror surfaces are a mosaic type composition of 116 spherical mirror units: 68 of them are regular hexagons with a side length of 261 mm, the other 48 are pentagons of six different sizes. To minimize the possible distortions of the image, the central region of the mirror wall is equipped with the hexagons with the angle of curvature closest to the nominal value, and going farther, sequences of mirrors minimizing R-variation are chosen. The mirrors are adjusted so they are placed on a net-like wall using joints which permit a rotation on two orthogonal axis and the mirrors alignment. The geometrical aberration due to difference between the nominal and the real radius of the mirror is 0.32 mrad for particles incident at small angles and larger for particles produced at larger angles.

The RICH photon detectors

The geometry of a spherical mirror is such as to focalise parallel incident rays in the same point of the focal plane: thus, the distance of the detected photon from the centre of the photon detector depends only on the polar angle of the track at the RICH-1 entrance (ϑ_{RICH}). Since COMPASS is a fixed target experiment, there is a strong correlation between the particle momentum and the polar angle of its track: low momentum particles are mainly detected in the outer part of the detector. The Cherenkov effect saturates with the momentum: the Cerenkov angles produced by different particles become closer as momentum increases, and thus the resolution needed for PID at high momentum is higher than the one needed at low momentum. The photon detector system is split into two symmetric parts, one above and one below the beam line. Each part is divided in 8 units: 6 equipped with Multiwire Proportional chambers (MWPC) and the two central ones equipped with multi-anode photomultipliers tubes (MAPMT). The photoconverstion in the MWPCs is provided by a CsI photocathode, that is a printed circuit board, segmented into mm^2 pads coated with a CsI film. The CsI converts photons in the UV domain, below 200 nm. The MWPC are operated in methane at atmospheric pressure, at low gain ($< 5 \times 10^4$) to preserve the CsI. The read-out system is based on the APV chip, which measures three amplitude samples on the rising edge of the signal and has a negligible dead-time. The units equipped with MAPMTs are arrays of 12×12 multi-anode photomultipliers, segmented into 16 pixels 4×4 mm^2 each. Each MAPMT is coupled with a fused silica lens telescope(a fields lens followed by a concentrator

lens), that allows to enlarge the pixel size to a final equivalent dimension of 12×12 mm^2. The wavelength sensitivity goes from the near UV to the visible region, namely from 200 to 650 nm and the gain is high (> 106). The fast signal rise time (< 1s), makes this kind of detector suitable for high background occupancy regions, like the central part of the detector, where the image of the beam halo is formed. The lens telescope introduces a distortion in the image, that is larger for photons with large incidence angle, mainly due the chromatic dispersion of the photons. With a ray-tracking exercise, the distortion have been estimated to be up to 4.

4.5.2 The muon identification

The muon identification is performed by two detector systems: the *Muon Wall 1* (MW1) which is located in the LAS and the *Muon Wall 2* (MW2) which is located in the SAS. Both systems are made of a set of tracking detectors and a hadron absorber followed by an other set of tracking detectors. The MW1 consists of two stations separated by a 60 cm thick iron absorber (*Muon Filter 1*). The SAS muon filtering system consists of a set of tracker detectors behind the SM2 which are combined with an iron absorber 2.4 m thick (*Muon Filter 2*) and followed by two stations MW2 and three MWPC stations.

The basic element of the MW1 system is the Mini Drift Tube (MDT) which is a gaseous wire detector working in proportional mode. An MDT module is composed by eight aluminium cells with a wall thickness of 0.6 mm covered on top by 0.15 mm thick stainless steel foil, 50 μm diameter gold plated tungsten wires and an ABS plastic envelope (see fig.4.11); the wire pitch is 10 mm. The MW1 consists of two stations each composed by four detectors with two planes of MDTs on both sides to provide the X and Y coordinates (see fig. 4.11). The outer surface of each station is covered with thin aluminium sheets for mechanical, electrostatic and noise protection. The active areas of each MW1 is 4845 × 4050 mm^2 for the X projection and 4730 × 4165 mm^2 for the Y projection while the central holes measure 1445 × 880 mm^2 and 1475 ×765 mm^2, respectively. The total number of modules which form the system is 1056. The MW1 system permits a measurement of each projection with an accuracy of $10/\sqrt{12}$ mm for the 10 mm wire pitch.

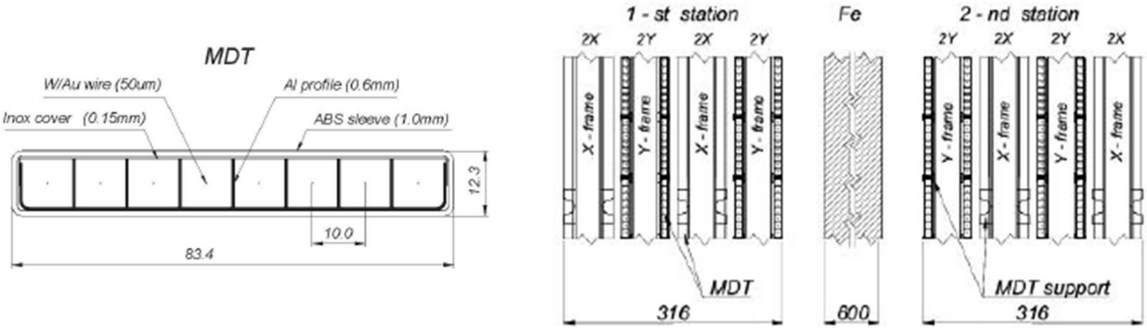

Figure 4.11: Cross-section of a MDT module (left) and schematic cross-section of the MW1 detector (right).

The MW2 is composed by two identical stations which consist of six layers of

drift tubes with an active area of 447 × 202 cm ^{2} grouped into double layers. The projections measured by the three planes are vertical, horizonthal and inclined of -15^o respect to the vertical. The drift tubes diameters 29 mm and the thickness is 0.5 mm.The wires pitch for each layer is 33.5 mm. A rectangular hole of 1 × 0.8 m^2 around the beam is realised.

4.5.3 The hadron and electromagnetic calorimeters

The COMPASS spectrometer contains two Hadron calorimeters and two Electromagnetic calorimeters. The two hadron calorimeters (HCAL1-2) are placed before the muon filters to measure the energy of the hadrons produced in the target and to participate in triggering of the inelastic muon scattering events.

The HCAL1 calorimeter consists of 480 modules each composed by 40 layers of iron and scintillator plates 20 mm and 5 mm thick, respectively, amounting to 4.8 nuclear interaction length. These modules are located on a matrix of 28 (horizontal) × 20 (vertical); in each corner 12 sectors are left empty and in the center a rectangular window of 8 × 4 modules doesn't contain modules for the passage of the beam and scattered muons. The outside dimensions of HCAL1 are 4.2 × 3 m^2 and useful surface is 10.8 m^2. The signal produced by the scintillators is sent from the PMTs via 50 Ω cables 140 m long to to ADC converters. Small fraction of this signal is used in the trigger system. The stability of the calorimeter during data taking is checked by a system which distribute the light emitted by a Light Emitting Diode (LED) to all the 480 modules. The evaluation of the efficiency which has been done also considering the efficiency of the cluster search and the energy reconstruction, has given a value very close to 100% for particles with momentum above 5 GeV/c.

The HCAL2 calorimeter consists of 22 × 10 modules arranged on a mobile platform. In the centre of the detector a hole of 2 × 2 modules has been done to let the high intensity beam pass by. Two types of modules are used to compose HCAL2: one type consists of 36 steel plates with a thickness of 25 mm alternated by 5 mm thick scintillator sheets, the other one consists of forty layers of thicker modules. This last kind of modules cover the central 8 × 6 cells. A silicon compound provides the optical contact between the scintillators and the PMTs. The PMT signals are transmitted to an ADC converter; as for HCAL1 also in this case a very small part of the signal is used by the trigger system. The HCAL2 stability monitoring is done using a light pulse from a group of LED. The monitoring system is used for amplification, adjustment and control. The efficiency of this detector is close to 100% for hadrons with energy above 10 GeV. The two electromagnetic calorimeters have not been used in the 2010 transversity run and will be not discussed here.

4.6 The trigger system

The COMPASS trigger system is designed to select the event candidates in a high rate context with a time windows smaller than 500 ns and with minimum dead time, and to trigger the read-out of detectors and front-end electronics. This system consists of a series of fast hodoscopes, calorimeters and veto system. These elements are differently combined in the case of muon or hadron beam, in the following the trigger system configuration for the muon beam will be described. The main goal

of the trigger system is to detect events in a Q^2 range from ≈ 0 to the maximum Q^2 value allowed by the kinematic. The events at high Q^2 are mainly selected with the vertical target pointing method. The muon track is reconstructed using two horizontal scintillator hodoscopes and is projected in the non-bending plane (the ZY plane); the trigger system select the good events checking the compatibility of the muon scattered angle θ and the target position. At low Q^2, and so at low scattering angle, this method is not useful because the track reconstruction is not precise using hodoscopes only. For this reason, in this kinematical region, the hodoscopes measure the muon energy loss using the two spectrometer bending magnets and the trigger is given if a minimum energy loss is detected. In addition, for these events, minimum energy deposit is required also in the hadronic calorimeters to eliminate background due to beam halo and elastic scattering off electrons and nuclei. Each hodoscope station is composed by two hodoscopes with in the middle an absorber to reject hadrons and electrons. Five different triggers have been used in 2010: the "Large Angle Spectrometer Trigger (LAST)" (H1,H2), the "Inner Trigger (IT)" (H4I,H5I), the "Ladder Trigger (LT)" (H4L,H5L), "Middle Trigger (MT)" (H4M,H5M) and the "Outer Trigger (OT)" (H3O,H4O). The positions of the various hodoscope is shown in fig. 4.12. The main feature of this trigger is the covering of the region at large x which is the region in which the asymmetry signal is larger, as will be shown in chapter 6. The LT and OT trigger events at high Q^2 and only the scattered muon information is used.

The calorimetric trigger is used to cover the high Q^2 region which is not covered by the other triggers and in particular by the OT. To protect the triggers from the background due to the halo beam, two Veto counters have been added. They consists of two scintillator counters upstream the target, the first (Veto 1) has an area of (250×320 cm^2) and the other one (Veto 2) has an area of (2.30×30 cm^2). The veto counters induce a dead time which is about the 20 % at nominal beam intensity: this is without doubt a drawback of the Veto. Otherwise it's clear the importance of these counters, which are used only in the Middle trigger, using the full veto system, the middle trigger rate is reduced from 1.4×10^6/spill to 18000/spill.

4.7 Data acquisition

The amount of data generated by the 250000 detector channels and recorded per year is of the order of thousand TB. The data acquisition system has to manage the high rate flux of $2{\cdot}10^8$ μ per spill, a typical event size of 45 Kb, and trigger rates of 10 kHz (during the μ run of 2010). A very performant pipelined and nearly dead-time free readout scheme has been adopted. The Data acquisition (DAQ) in COMPASS has the granularity of a Run, each composed of a certain number of spills (100 or 200 according to the physics programme/trigger). The data flow in the DAQ architecture is summarized in fig. 4.13 and is carried on essentially in three steps.

The data collected by the detectors are digitalized directly at the front-end by ADCs (Analog-to-Digital Converters) and TDCs (Time-to-Digital Converters) according to the type of detectors the front-ends are coupled to. The data are then transferred to readout driver modules named CATCH (COMPASS Accumulate, Transfer and Control Hardware) and GeSiCA (GEM and Silicon Control and Acquisition) and undergo a formatting along with further timing synchronization in-

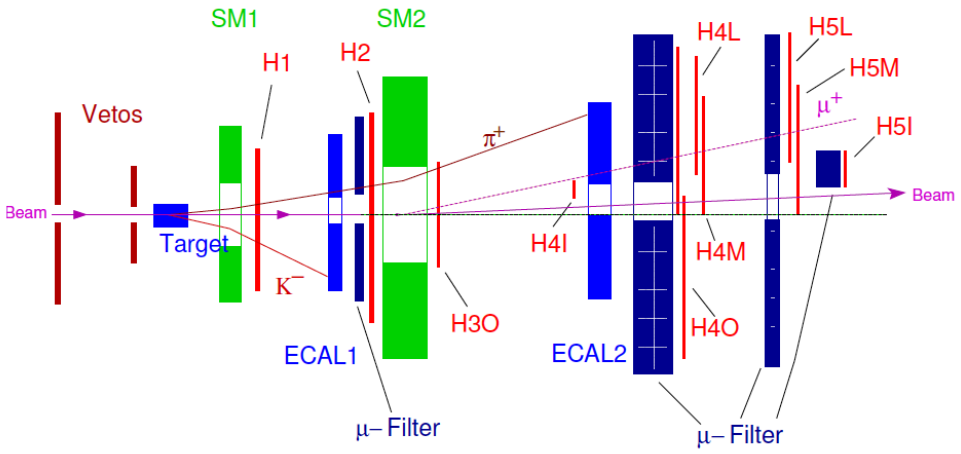

Figure 4.12: Position of the components of the trigger system.

formation integration. Subsequently the data are transmitted to a number or Read Out Buffers (ROB's) through some 64 S-Link optical lines, with a total bandwidth of about 1300 GB/s. The used S-Link standard was defined by CERN. Each read-out module is interfaced to the S-Link lines by an S-Link source card and the ROBs motherboard by a sub-set of S-Link destination "S-Link to PCI" cards, named spill-buffers. The latter incorporate a memory of 512 MB each, in order to decouple the on-spill data stream from the ROB PCI bus. Namely, 4 S-Link lines concentrate in one ROB and the the usage of the spill-buffers allow making use of the SPS duty cycle: during the 9.6 s of beam time the data are written into the memory and during the full cycle of 38.7 s they are read through a PCI interface. In this way the required bandwidth is reduced by a factor of three.

Off-spill, the ROB's empty the spill buffers and carry on a first sub-event building by combining the data belonging to the same event. At this stage sub-events belonging to a single event are handled by different ROBs. These data are then transmitted to the Event Builders via a High Performance Parallel Interface (HiPPI) protocol, exploiting its main feature of allowing to build the destination address via the modulo of the event number, so that that any sub-event of an event will always be delivered to the same event builder. The load balance is obtained thus through a round robin multiplexing.

At the Event Builders (high-performance off-the shelf PCs) the sub-event-blocks are extracted from their HiPPI envelope and ordered according to the detector they came from. The sub-events are thus assembled into a complete event and written locally on disc to a binary file in the DATE format (the Alice Data Acquisition package). The event building is carried on asynchronously with respect to the in/off spill timings that characterize the previous two steps. Each output file is closed when it reaches the size of 1GB and a new output file is opened in turn until the event builder has built every event of the current Run. In this way all the events of a Run turn out to be stored in a set of 1GB-sized files (named after the Run number they belong to). Asynchronously, event-meta-data are extracted from the output

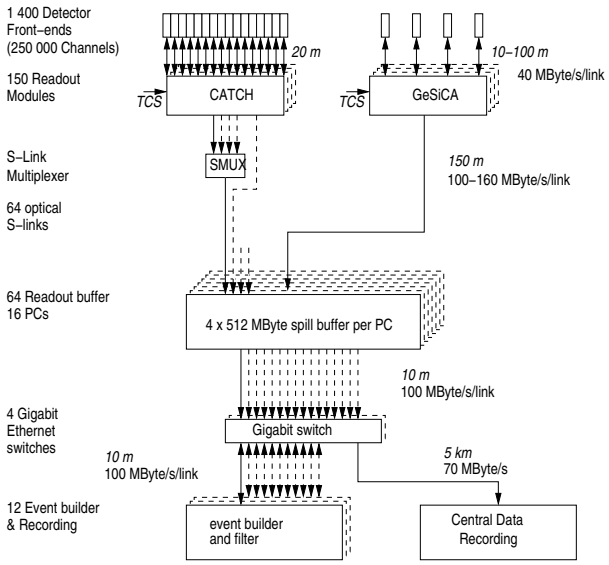

Figure 4.13: General architecture of the DAQ system. Digitised data from the detector front-ends are combined in the readout modules named CATCH and GeSiCA close to the detectors. The storage of the data during the spill and the event building is performed locally. The data are then recorded at the CERN computer centre.

files to populate a database and the files themselves are sent over to the central CERN store facility, as described in the paragraph 4.8.

Trigger Control System and readout modules

In a pipelined system it is mandatory to keep track of all events by marking them properly. Even in case of failures or time-outs at least a certain header information should be generated to guarantee a continuous flow of events. The header information should match the received trigger and timing and should be inserted as early as possible in the data flow. To this extent a sophisticated system, the Trigger Control System (TCS), synchronizes the digitising and read-out units.

The TCS distributes trigger, time reference and event identification information to the readout-driver modules (GeSiCA and CATCH) and generates the strobes for gating some of the analogue-to-digital converters.The TCS utilizes an optical distribution system which broadcasts information from a single source to a few hundred destinations using a passive optical fibre network. The TCS receiver is plugged at the back side of each slot where GeSiCA or CATCH modules are located. The receiver recovers the 155.52 MHz clock from the incoming data, decodes the data, the trigger and provides this information to the readout-driver module. The readout-driver modules distribute trigger and timing signals to the front-ends, perform the initialisation of the front-ends and serve as a concentrator for the data received from the digitising units of the front-ends. The reference clock, synchronisation signals as well as spill and event numbers are transmitted optically on fibres from the trigger control system to the TCS-receivers. The TCS receivers transmit the decoded information to each CATCH or GeSiCA module. The readout-driver modules act as a fan-out and transmits the reference clock and synchronisation signals to the

front-ends. The complete events are transmitted with a S-LINK transmitter to the readout buffers via optical fibres.

4.8 The offline system

Once produced by an event builder, each file undergoes asynchronously further handling. Event meta-data are extracted from them in order to populate a database the usage of which allows to have an efficient means of accessing the events data later in the off-line processing (for example fast event-aggregation by trigger type is possible thanks to this solution). Currently the COMPASS event store is implemented as an hybrid system which maintains the event-data in the original flat bynary files and holds the event-metadata, associated to the relevant plain-file entry for each event in an Oracle RAC database system. When the meta-data extraction is over, a file is marked as liable to central recording, so it is then copied over to the CERN central computer centre through a dedicated Gigabit Ethernet link, which is able to sustain a parallel-streams of TCP/IP traffic whose average bandwidth has grown over the years from 40MB/s to 70MB/s. The Central Data Recording (CDR) marks the off-line stage of the COMPASS data flow and consists in the storage of the data on tape under CASTOR, the hierarchical storage system [46] developed and adopted at CERN. The copy of the files is carried on by RFIO CASTOR clients, so that the actual handling of the files, from the event builders local disc pools to the CERN computing centre tapes, is performed transparently. When CDR is requested for a file, it is actually written temporarily by CASTOR on disc (within a dedicated pool of discs) and then asynchronously migrated to tape. A specific configuration of CASTOR has been created for COMPASS and 6 tape writers are reserved for CDR. Only when a file turns out to have been actually migrated to tape, its local copy on the event builder disc pool is deleted to prevent any data loss. In the current configuration the event builders disc pools are sized so that they can cope with any CDR failure that lasts up to 48 hours. Once registered under CASTOR name space, the access to the files is thoroughly managed by CASTOR and from within the reconstruction framework designed by COMPASS, which will be described later on, the data can be retrieved simply by means of requests to the event-database, which translates high-level requests of data into file-block-entry requests. In 2010 the amount of data collected by the experiment has been about 1.9 PB. The collected data for each Run corresponded to 200 consecutive spills.

The huge amount of data of about 2000 TBytes/year is reconstructed at the CERN computer centre, requiring a computing power of about 9000k SPECint2000.

The event reconstruction is carried on by CORAL [72], the COMPASS reconstruction and analysis framework, a fully object oriented program with a modular architecture written in C++, which provides interfaces for the event reconstruction algorithms and insulation layers to access the data and for external pluggable packages. The reconstruction is carried out in parallel, by some 3000 jobs running on the CERN batch system. Although this is the minimum computing power granted to COMPASS, as agreed with the CERN Information Technology Division, COMPASS is allowed to exploit some of the temporarily unused computing resources up to $\sim$ 4500 parallel jobs, which amount to about 13000k SPECint2000.

CORAL decodes the data, reconstructs tracks and vertexes, and performs the

particle identification by making use of the alignment and calibration data describing the apparatus, which are stored as time/version-dependent information in a MySql database. The reconstructed data are output in a proprietary binary format to files called Data Summary Tapes (DSTs), and in ROOT [73] format to mini-DSTs. The latter are selectively filtered out subset of the DSTs and are produced during the reconstruction and turn out to have a size of about 4% of the original RAW data. DSTs and miniDSTs are stored also centrally on tape, under CASTOR. The physics analysis is performed on the mini-DSTs, replicated in the different institutes, by means of PHAST [74], the COMPASS framework for the final data analysis. fig. 4.14 depicts the reconstruction and analysis system to which the data flow after they are stored centrally.

For the correct track reconstruction a crucial procedure must be performed: the alignment of the detectors. The alignment also is carried on by means of CORAL and it is implemented by performing a track reconstruction and then by minimising the χ^2 of all tracks simultaneously. Initially the tracks are reconstructed using detector positions determined by a geometrical survey. The optimised parameters are: *i*) the position of the detector centre, *ii*) the rotation between the detector coordinate system and the global coordinate system, *iii*) the effective distance between adjoining wires or pads. The procedure is iterated until the changes in the detector positions become negligible compared to their resolution. The adjustment of detector parameters is first done using data samples, collected with the spectrometer magnets switched off, so that straight trajectories through the spectrometer can be assumed, and then refined using standard data. The alignment procedure is repeated after each long interruption of the data taking and each time some detector has been moved.

4.9 Event reconstruction

The input to the reconstruction software is either the raw data collected in the experiment, or the output of the Monte Carlo simulation software. The data files produced by the COMPASS acquisition software contain the raw information from the detectors, digitised by the front-end electronics. Two processing phases are needed to prepare the input to the track finding algorithm. In the first phase, called "decoding", the information on the fired detector channels is extracted from the raw data. In the second phase, called "clustering", detector channels that are fired by the same particle are grouped together and the information on the geometrical position of each detector in space, retrieved from the Data Base, is used to calculate the coordinate of the cluster in the main reference system of the apparatus. The information from tracking detectors is then used to reconstruct the trajectories of the charged particles through the spectrometer and to determine their momenta. The track reconstruction algorithm consists of three phases: pattern recognition (i.e. finding track segments in the various zones of the spectrometer), bridging (i.e. connecting track segments from several distinct zones to build full tracks), and fitting (i.e. computing the best estimators for the parameters of the reconstructed tracks).

The "pattern recognition" selects sets of clusters consistent with track segments. To that end, 5 zones along the beam are considered, where track segments are expected to be approximately straight lines: the region between the last magnet of

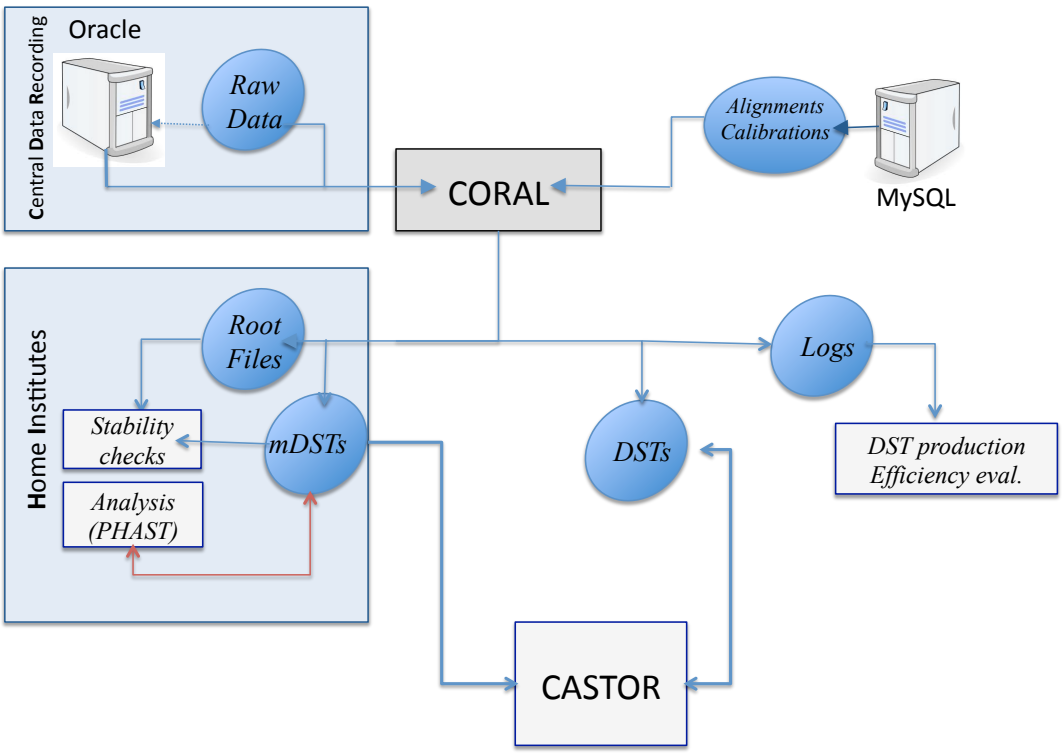

Figure 4.14: Schematic representation of the COMPASS reconstruction software.

the beam line and the target, from the target to SM1, from SM1 to SM2, from SM2 to the second muon filter, and downstream of the second muon filter. In the first region only beam tracks are looked for: the tracks reconstructed in the beam telescope are extrapolated upstream and associated, on the basis of time and position, to the hits in the BMS, (see sec. 4.2), thus allowing the reconstruction of the momentum of the incident beam trajectory.The reconstruction is first performed in projections. For this purpose the detector planes in each zone are divided into groups measuring the same projection of a track and a selection of candidate track projections is then performed, based on the number of clusters, and taking into account its variation as a function of the track angle. In the next step, all projections are combined to produce space track segments. In this procedure pairs of projections are associated to obtain a road in space and all the clusters within this road from all detector planes are collected. All track candidates are then compared to a dictionary (a look up table) of possible tracks through the COMPASS spectrometer. The track segments found in this phase are used to build the full tracks via "bridging" (i.e. connecting track segments) trough two adjacent zones. The successfully combined track segments are then ordered according to a quality function based on the χ^2 and the number of hits associated to the track. The combination with the best quality function is

retained, while combinations re-using one of the previously accepted segments are discarded. The process is iterated until the list is exhausted. In the final phase of the tracking algorithm, magnetic fields and material maps are used to get the best estimates of the track parameters (x and y positions, $\mathrm{d}x/\mathrm{d}z$ and $\mathrm{d}y/\mathrm{d}z$ slopes, inverse momentum $1/p$) and their error matrix. For this purpose, the Kalman fit method is used twice, first in the downstream and then in the upstream direction, in order to provide the track parameters both at the first and at the last measured point of the track.

The list of tracks with the last measured point downstream of SM1 is then scanned to search for the muon outgoing from the primary interaction vertex (scattered muon). A track is identified as a scattered muon if it corresponds to a positively charged particle, and if its trajectory is compatible with the hodoscope hits as given in the trigger matrix. In addition, the muon track candidate must cross the entrance and the exit of the polarized target at a distance smaller than 5 cm from the beam axis. The beam track and the fringe field tracks are excluded from the search.

The following step in the event reconstruction is reconstruction in space of the primary interaction point ("primary vertex") or of the two-body decays point of neutral particles ("V^0 vertices") to get the best estimate of the coordinates of the vertex position and of the three components of the momentum vector of each track at this vertex, and the corresponding covariance matrices. A first estimate of the primary vertex position is obtained by computing the average of the closest points approach between one beam track and all possible outgoing tracks. All tracks (but the scattered muon μ') having a point of closest approach too far from the mean are discarded. Since in an event more than one beam track can be reconstructed, in this phase many primary vertices can be identified. The "best primary vertex" is the primary vertex with most outgoing particles and, if this is not enough to determine uniquely the best primary vertex, that with the smallest χ^2 of the fit is selected. The tracks are then used to perform the fit of the vertex position by an inverse Kalman filter algorithm. During the first iteration, all tracks are used to estimate the parameters of the vertex, and the relative χ^2 contribution of each track to the fit is computed. If the largest χ^2 contribution exceeds a threshold value, the corresponding track (if it is neither a reconstructed beam track nor a scattered muon track) is removed from the list and the procedure is iterated once more. The algorithm stops when all remaining tracks survive the χ^2 selection.

Secondary vertices are reconstructed both inside the target and also several meters downstream, so that nearly all K^0_S, Λ and $\overline{\Lambda}$ decays into charged particles are observable. The V^0 vertices are searched by combining all pairs of tracks with opposite charge, regardless of their association to the primary vertex.

The mean energy deposit associated to a single particle can be either an hadron or an electromagnetic calorimeter cluster. A calorimeter cluster can be associated either to a neutral particle, in this case we define it as neutral calorimeter cluster, or to a charge particle (charged calorimeter cluster). The hadron calorimeter clusters are used to separate muons and hadrons. Electromagnetic calorimeter clusters measure the energy and impact coordinate of photons and electrons. Hadron identification is performed by the RICH; a dedicated software package which combines information from the RICH photon detectors and from reconstructed tracks and momenta, is used to calculate the most probable Cherenkov angle and to assign probabilities to

all possible particle hypotheses.

The RICH Particle Identification algorithms

The PID with the RICH is performed with the CORAL package RICHONE [75] which combines the information on the photon coordinates measured by the photon detectors and the particle trajectory at the RICH entrance window from the track reconstruction. A charged particle, travelling through the radiator gas, with a velocity larger than c/n, where n is the refractive index, emits photons. The polar angle θ of the emitted photons, with respect to the given direction of the particle trajectory, depends only on the refractive index n and on the mass M of the particle while the azimuthal angle ϕ is uniformly distributed. For this reason all the photons emitted by a given particle are expected to have the same Cherenkov angle θ. The background photons, which are not produced in this process, are expected to have a smooth θ distribution. The measurement of the trajectory of the photons emitted by a considered particle and its Cherenkov angle θ allows to identify the particle. The photon trajectory is reconstructed making use of the Ypsilantis-Seguinot algorithm [76]: for each photon and each accepted particle the photon trajectory is calculated using the mean position of the particle in the radiator gas and the measured coordinates of the photon. The quality of the PID which is achieved by the COMPASS RICH can be appreciated in fig. 4.15, where the mean Cherenkov angle θ is plotted versus the momentum of the particle. The π, K and p thresholds are, clearly, visible (2.8, 9.5, and 19 GeV respectively), as welle as the fact that π's and K's can be separated up to momenta of $\sim$ 50 GeV/c. In order to optimize the PID, the identification algorithm is based on the maximum likelihood estimator [77] in which one compares the expected value evaluated by the Cherenkov equation:

$$cos\theta_M = \frac{1}{n\beta} = \frac{\sqrt{P^2 + M^2}}{nP}, \tag{4.1}$$

(for the mass hypothesis M and momentum P), and the Cherenkov angle measured for each photon found in a fiducial region (θ <70 mrad). For each particle the Likelihood function is evaluated considering five different masses (e, μ, π, K and p), as well as the hypothesis of no signal, to discriminate the background. The expression of the likelihood function for each mass hypothesis M is:

$$\mathcal{L}_M = \exp[-(S_M + B)] \prod_{j=1}^{N} \Big[s_M(\theta_j, \phi_j) + b \Big], \tag{4.2}$$

where s_M and b are respectively the signal and background probabilities, S_M and B their integral over the fiducial region, and N is the number of detected photons in the fiducial region. The signal probability depends on the mass as given in this formula:

$$s_M(\theta_j, \phi_j) = \frac{S_0}{\sigma_{\theta_j}\sqrt{2\pi}} exp[-\frac{1}{2}\frac{(\theta_j - \theta_M)^2}{\sigma_\theta^2 j}]\epsilon_D(\theta_j, \phi_j), \tag{4.3}$$

where $S_0 = N_0 sin^2\theta_M$ is the expected number of photons from the Frank-Tamm law and $\sigma_{\theta j}$ is the single photon resolution of the photon detector. The $\epsilon_D(\theta_j, \phi_j)$

term takes into account the probability that the photon is detected. The particle identification is done using the six likelihood values and assuming that the maximum likelihood value corresponds to the good mass hypothesis. As shown in fig.4.15 it's possible that two particles have the same Cherenkov angle and, of course, a very similar likelihood value. In chapter 5 it will be discussed how to refine the identification requiring that the ratio between the maximum value and the second maximum value is larger than a fixed threshold. The rejection of the events for which this condition is not verified improves the purity. No cuts on the ratio between the maximum value and the background value are applied because the central region of the RICH is background-free.

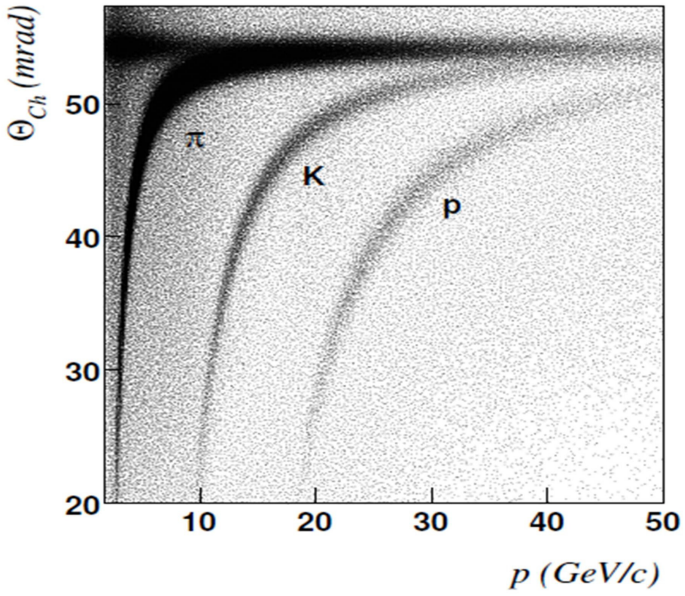

Figure 4.15: The measured Cherenkov angle θ versus the identified particle momentum P.

A crucial point in the particle identification using the RICH detector is the determination of the refractive index of the radiator gas. The refractive index of a radiator gas depends on many parameters, such as the gas purity, pressure and temperature so it is time dependent. For this reason it is measured at regular time intervals and the evolution is calculated as a function of the pressure and the temperature of the gas, which are measured with a precision at the 0.1% level. The refractive index measurement is performed from the data considering all the photons associated to one particle of given momentum and assuming the pion mass hypothesis. These two conditions together with the measured of the θ angle allows to measure the refractive index from the eq. 4.1.

The ideal image produced by a single charged particle on the photon detector plane is a ring. The "ring reconstruction algorithm" allows to measure the radius of the ring and this measurement is used for the calibration of the RICH detector.

The mean value of the distribution divided by the focal lenght of the mirrors gives the mean θ_R angle value and all the photons inside 3σ are considered photons of the ring. The single photon resolution σ_θ is the Gaussian RMS of the distribution $\theta - \theta_M$ assuming the pion mass hypothesis. The overall photon resolution is $\approx$2.5 mrad and the ring resolution σ_0 is the width of the distribution of $\theta_R - \theta_M$ and is estimated from the data to be $\approx$1.6 mrad.

Chapter 5

Analysis of the 2010 data

The 2010 run has been totally dedicated to the measurement of the transverse spin effects with a 160 GeV/c μ^+ beam and the transversely polarized proton target. The data taking started in June and finished in November. The data have been collected during 12 different periods each consisting of two sub-periods of about 5 days. In between the two sub-periods the target polarization was reversed. The periods and the corresponding target polarizations are given in table 5.1. COMPASS labels periods as indicated in column two but for simplicity in the following we will refer to the chronological order as reported in column one. This chapter is devoted to the description of the analysis of the data collected in 2010. The analysis of these data is very similar to that of the data collected with transverse target polarization in the previous years and in particular in 2007. In section 1 the selection of DIS and SIDIS events and the identification of the final state hadrons are described. Section 2 is dedicated to the tests of the data quality and stability and to the definition of the final data sample. In section 3 the methods used to extract the asymmetries are described while section 4 is dedicated to further stability tests and to the evaluation of the final systematic errors. The results will be illustrated in chapter 6.

5.1 Selection of SIDIS events and final state hadrons

5.1.1 SIDIS events

The mDST produced as described in sec. 4.9 have been copied on the local farm in Trieste to perform the physics analysis. They have been first "filtered" selecting only events with at least a primary vertex with at least two final state particles with momentum larger than 1 GeV/c, reducing the mDST size from 83 TB to 30 TB.

These events have then to satisfy several requirements which are described in the following. The position of the best primary vertex has to be inside the polarised target. In particular we ask the transverse coordinates in the laboratory system x_{vtx} and y_{vtx} to satisfy the requirement $(x_{vtx}\text{-}x_0)^2+(y_{vtx}\text{-}y_0)^2<r_0^2$ where x_0 and y_0 are the coordinates of the centre of the target cells in the laboratory system. The value of the effective radius of the cells r_0= 1.9 cm, has been fixed taking into account the vertex reconstruction resolution. The values of x_0=-0.2 cm and y_0=0.02 cm have been measured looking at the events with primary vertex on the wall of the cells. It has also been checked that, for the 2010 data, the values of x_0 and y_0 do not change

Table 5.1: Summary of the 2010 run periods and their polarizations. For each period the number of events on tape, the integrated muon flux and the orientation of the polarization in the three target cells are given.

Period	Week	Events collected	Beam flux ($\times 10^{12}$)	Sub-P 1 Pol	Sub-P 2 Pol
1	W23	1 099 896 305	2.73	↓↑↓	↑↓↑
2	W24	1 479 139 255	2.38	↑↓↑	↓↑↓
3	W26	1 158 982 236	2.00	↓↑↓	↑↓↑
4	W27	1 331 925 927	1.99	↑↓↑	↓↑↓
5	W29	2 090 396 862	2.58	↑↓↑	↓↑↓
6	W31	3 321 755 884	2.39	↓↑↓	↑↓↑
7	W33	3 689 568 241	3.54	↑↓↑	↓↑↓
8	W35	4 028 866 060	4.25	↓↑↓	↑↓↑
9	W37	4 148 031 518	4.22	↑↓↑	↓↑↓
10	W39	5 910 841 333	8.33	↓↑↓	↑↓↑
11	W42	4 173 112 436	4.34	↓↑↓	↑↓↑
12	W44	4 216 917 860	3.34	↑↓↑	↓↑↓

with z. A cut on the z coordinate of the primary vertex z_{vtx} is applied in order to select the events with the interaction point inside one of the cells of the polarized target and not in the region before, after or in between the cells which are filled with helium. In fig. 5.1 the distribution of z_{vtx} before (white distribution) and after (yellow distribution) this selection is shown.

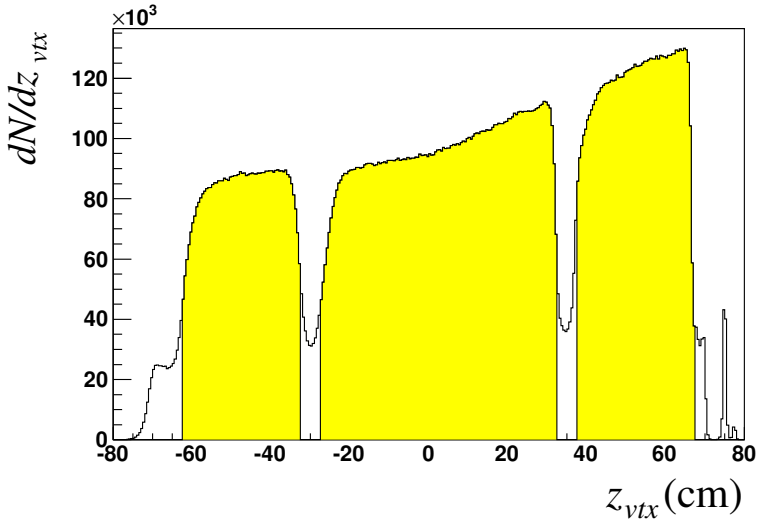

Figure 5.1: z coordinate of the primary vertex in the laboratory system.

For the incoming μ we require that:

- the μ track is reconstructed with χ^2_{Red} χ^2/(number of degrees of freedom) < 10;
- the beam momentum P_μ has been measured in the BMS;
- 140 GeV/c $< P_\mu <$ 180 GeV/c;
- the track extrapolation crosses all the three target cells to have the same integrated flux in each cell.

The scattered muon (μ') identification is done requiring that:

- the reconstructed track has $\chi^2_{Red} < 10$;
- z position of the last hit of the reconstructed track is after the Muon Filter 1, i.e. $z_{last} > 350$ cm;
- the charge of the particle associated with the track has the same sign of the beam particle;
- the extrapolation of the track goes through the active area of a pair of hodoscopes that gave the trigger, in the case of IMT, MT, LT and OT;
- the z position of the first hit detected for the μ' is before the SM1 ($z_{first} <$ 350 cm);
- the material crossed by the μ' candidate corresponds to more than 30 radiation lengths.

Only events with only one μ' candidate outgoing from the primary vertex are accepted.

The identification of the beam and scattered muons permits to construct the invariant kinematical quantities used to describe the DIS processes: Q^2, y, W and x. The DIS events are selected rejecting the events with Q^2<1 (GeV/c)^2 and to exclude the region of nucleon resonances, a cut on the invariant mass of the final hadronic state $W < 5$ GeV/c^2 is applied. Also the relative energy lost by the muon in the scattering process y has to be between 0.1 and 0.9 and the Bjorken variable x has to be in the range $0.003 < x < 0.7$. Fig. 5.2 shows the kinematical distributions obtained for the two-hadron analysis events.

5.1.2 Final state hadrons

The particles outgoing from the primary vertex that are not identified as muons are hadron candidates. The candidates have to satisfy the following requirements:

- the reconstructed track must have $\chi^2_{Red} < 10$;
- the crossed material has to correspond to less than 10 radiation lengths;
- the z coordinate of the first hit of the track has to be $z_{first} < 350$ cm;

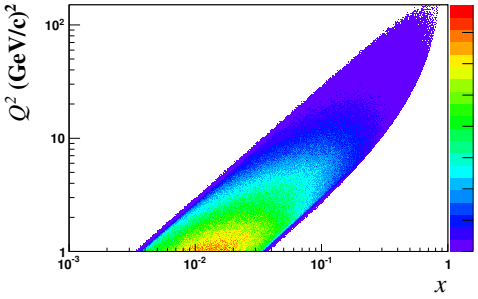

(a) Q^2 versus x scatter plot.

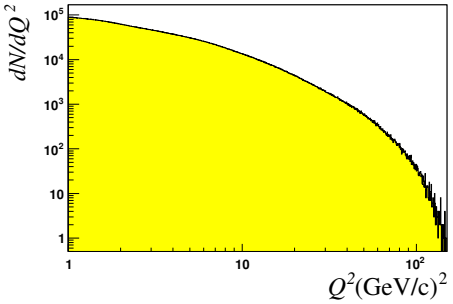

(b) Q^2 distribution.

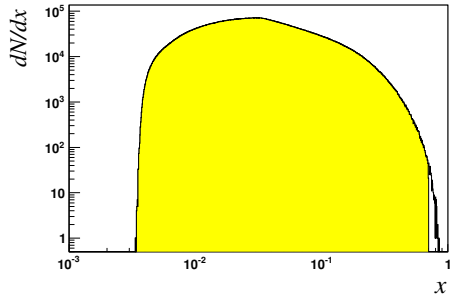

(c) x distribution.

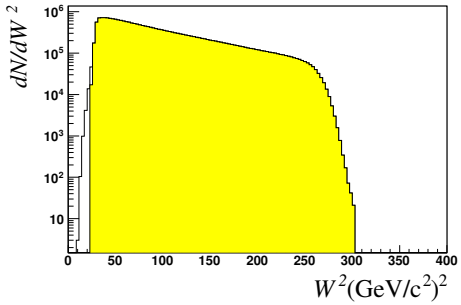

(d) W^2 distribution.

Figure 5.2: Q^2 versus x (a), Q^2 (b), x (c) and W^2 distributions of the events obtained after the two-hadrons analysis cuts.

- the z coordinate of the last hit of the track has to be 350 cm $<z_{last} <$ 3300 cm.

In the analysis of the COMPASS 2007 proton data the calorimeter information has been used to select the hadrons, giving an extra rejection of a few percent. For the 2010 data, given the small effect of the selection and the instabilities of these equipments during the data taking, no cut has been applied.

For the measurement of the single hadron transverse spin asymmetries at least one hadron outgoing from the primary vertex is required. The further cuts applied to select the "good hadrons" are:

- a fraction of the available energy transported by the hadron $z > 0.2$, to select the current fragmentation region;

- the transverse momentum of the hadron with respect to the virtual photon direction $P_{hT}>0.1$ GeV/c, to have a good resolution in the azimuthal angle of the hadron.

For the measurement of the two hadron asymmetry at least two hadrons outgoing from the primary vertex are required and the following cuts are applied to select the hadron pairs to be used in the asymmetry extraction:

- a fraction of the available energy transported by each hadron $z_i > 0.1$ (i=1,2), to select the current fragmentation region.
- the modulus of the component of the four-vector R defined in eq. 2.37 orthogonal to the virtual photon $R_T > 0.07$ GeV/c, again to have a good resolution in the azimuthal angle of the plane containing the two hadrons.
- the Feynman invariant $x_F = \frac{|P_{h//}|}{|P_{max//}|}$) larger than 0.1 for each hadron, which is almost equivalent to the previous requirement;

where $P_{h//}$ is the longitudinal momentum of the hadron in the centre of mass of the photon-nucleon system while $P_{max//}$ is the maximum longitudinal momentum available in the reaction.

The "missing energy" given by:

$$E_{miss} = \frac{(P + q - (P_{h1} + P_{h2}))^2 - (M_P c)^2}{2M_P} \tag{5.1}$$

is required to be larger than 3 GeV. This cut is applied to reject hadron pairs coming from the decay of the exclusive produced ρ^0. Fig. 5.3 shows the missing energy distribution (left) and the $z=z_1+z_2$ distribution (right) before (white) and after (yellow) the missing energy cut.

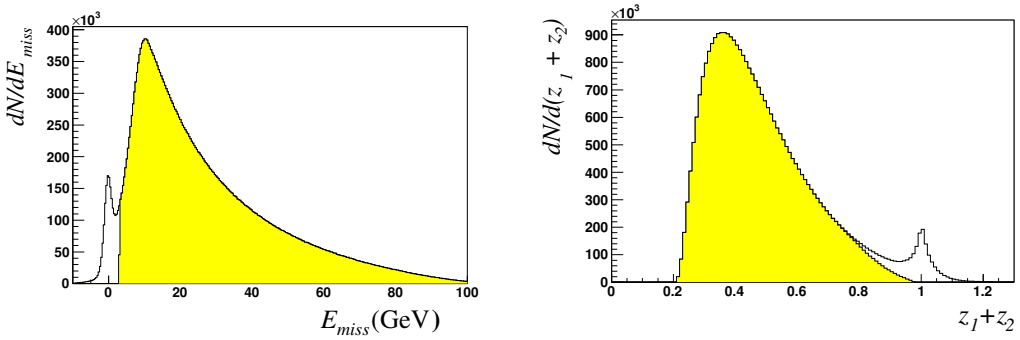

Figure 5.3: Missing energy (left) and $z = z_1 + z_2$ (right) distributions obtained applying all the cuts but the E_{miss} cut. The yellow filled histograms are the distributions obtained applying also the cut $E_{miss} > 3$ GeV.

5.1.3 Particle identification

Since the RICH operation in 2010 was almost the same as in 2007, the same selection has been applied to identify charged π and K. As described in sec. 4.9, for each track the result of the RICHONE package are the values of the likelihood function in the hypothesis e,μ,π,K,p and background. To associate a particle type to the track a cut is applied on the likelihood values which has to be tuned optimizing the efficiency and the purity. Here only a short description of the method used to tune the cuts is given. For more details see [78, 79].

The RICH efficiency is evaluated separately for kaons and pions considering respectively the ϕ_{1020} decay in K^+K^- pairs and the K^0 decay in $\pi^+\pi^-$ pairs. These events are selected asking for only two hadrons with opposite charge and with the invariant mass of the parent particle. The ϕ_{1020} life time is so small ($1.55 \times 10^{-22} s$) that is not possible to distinguish the primary vertex from the secondary vertex, while the selection of the K^0 decay events is done requiring that the K^0 gives a secondary vertex. To describe the procedure let's consider all the pair of hadrons h_1 and h_2 with invariant mass close to the K^0 PDG mass. If we select the events with h_2 identified as negative pions, in the ideal case, with 100% efficiency, all the hadrons h_1 should be positive pions. The ratio between the number of hadrons $h_1^{\pi^+}$ identified as positive pion over the total number of hadrons h_1^T gives the value of the identification efficiency ϵ_{π^+} of the RICH for positive pion. The remnant h_1 hadrons are unidentified or identified as kaon. The ratio of the number of hadrons identified as kaons $h_1^{K^+}$ and the total number h_1^T gives a further information: the misidentification probability. As an example, the invariant mass spectra for $K^0 \to \pi^+\pi^-$, is shown in fig. 5.4. In both plots the black line histograms have been obtained using oppositely charged hadrons. In the left plot the red line gives the distribution for identified $\pi^+\pi^-$ pairs while in the right plot the red line represents the misidentified pairs $(\pi \to K)$.

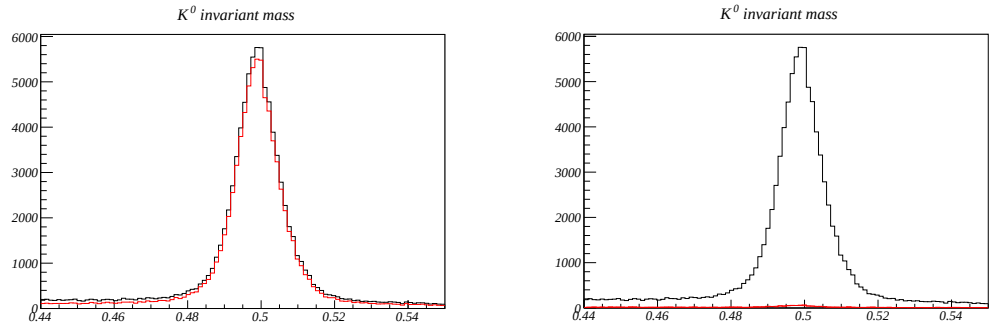

(a) (b)

Figure 5.4: Invariant mass distribution for pairs of oppositely charged hadrons. The red lines are the same distribution for $\pi^+\pi^-$ pairs (a) and π^+ K$^-$ (b).

If we indicate with $N^I_{\pi(K)}$ the number of identified pions (kaons), $N^{true}_{\pi(K)}$ the number of correctly identified pions (kaons) and $N^{Tot}_{\pi(K)}$ the total number of pions (kaons) in the sample we have that the $N^{true}_{\pi(K)} = \epsilon_{\pi(K)} \cdot N^{Tot}_{\pi(K)}$ and the $N^I_{\pi(K)}$ is given by the sum of the correctly identified pions (kaons) and the misidentified kaons (pions). These relations can be written in a compact way as:

$$\begin{pmatrix} N^I_\pi \\ N^I_K \end{pmatrix} = \begin{pmatrix} \epsilon_\pi & P(\pi \to K) \\ P(K \to \pi) & \epsilon_K \end{pmatrix} \cdot \begin{pmatrix} N^{Tot}_\pi \\ N^{Tot}_K \end{pmatrix}$$ where $P(y \to x)$ is the misidentification probability, namely the probability that a particle of type y is identified as a particle of type x.

The efficiency and misidentification matrices can be used to measure the purity which is given by the ratio between the number of particles of a given type correctly identified and the total number of particles identified as of the same type, including both the true and the misidentified particles:

$$Purity_{\pi(K)} = \frac{N^{true}_{\pi(K)}}{N^{I}_{\pi(K)}} = \frac{\epsilon_{\pi(K)} \cdot N^{Tot}_{\pi(K)}}{N^{I}_{\pi(K)}}. \quad (5.2)$$

A cut on the ratio between the maximum likelihood value and the second maximum likelihood value $\mathcal{L}_{first}/\mathcal{L}_{2nd}$ can be applied to reduce the misidentification probability. If the maximum likelihood value corresponds to a particle of type x we can fix a threshold $\mathcal{L}_{thr}(x)$ and consider unidentified the particles for which $\mathcal{L}_x/\mathcal{L}_{2nd} < \mathcal{L}_{thr}(x)$. The cut on the likelihood ratio is tuned for each different measurement to enhance the purity of the K sample, while keeping the efficiency as high as possible.

The efficiency and the misidentification probability are measured in several bins of the momentum and the polar angle of the track at the RICH entrance ϑ_{RICH} . These two variables have been chosen to take into account the dependence on the saturation in the number of produced photons, the occupancy, the background and the different photon detector types. The bin limits are given in table 5.2.

Table 5.2: Lower/upper values of the bins in which the efficiency and the misidentification probability are measured.

P_h(GeV/c)		2.8	9.6	13	18	25	35	50
ϑ_{RICH} (mrad)	0	0.01	0.02	0.03	0.04	0.06	0.11	0.3

Different values of the threshold have been considered and for each value the identification-misidentification matrices are extracted and the purity evaluated. The Cherenkov angle saturates with the momentum so, fixing the value of the threshold, the purity decreases with the momentum. In fig. 5.5 the misidentification probabilities are shown for each threshold value, as function of the momentum. The tuning is done choosing the threshold value which represents the better compromise between the maximization of the efficiency and of the purity. The value of $\mathcal{L}_{thr}(\pi)$ has been fixed to 1.02 while $\mathcal{L}_{thr}(K)$ has been fixed to 1.08. A further cut is applied requiring $\mathcal{L}_e < 1.8 * \mathcal{L}_\pi$ in order to distinguish electrons and pions. Finally a cut is applied on the maximum momentum of the particle $p_{max} < 50$ GeV/c. As can be seen in fig. 5.5 the misidentification probabilities are always smaller then 10 % even at high momenta: in particular, the probability of identifying a π as a K is not larger than 5 %.

5.2 Data quality and data selection

The data quality and stability are very important points in the data analysis because the measured transverse spin asymmetries are small, of a few per mille, and instabilities can produce systematic errors. This is even more clear if one keeps

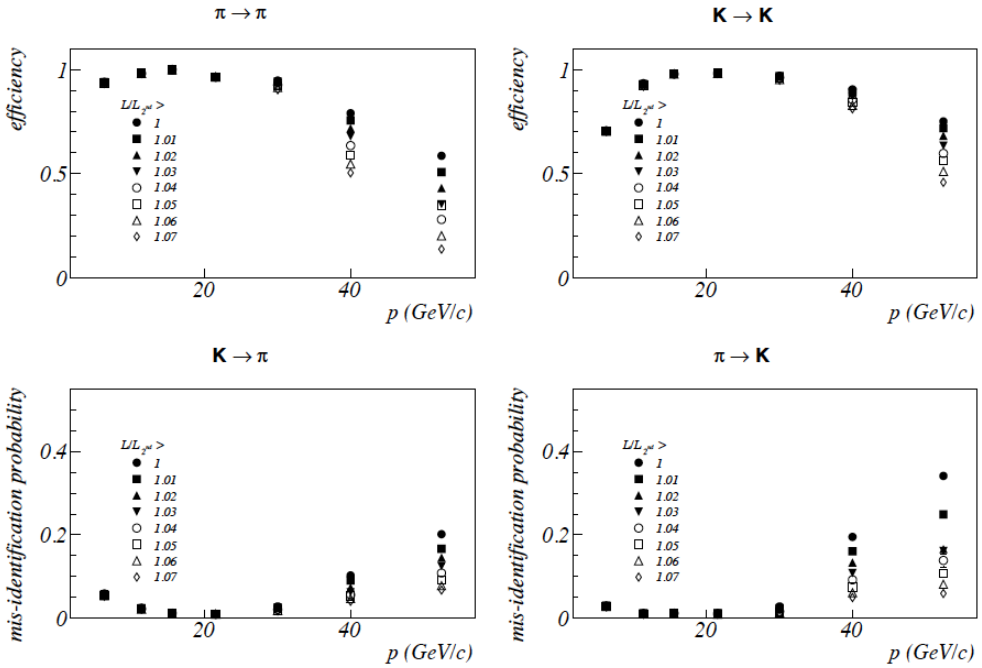

Figure 5.5: The efficiencies (top) and the misidentification probabilities (bottom) as function of the particle momentum for pions (left) and kaons (right). Different markers correspond to different cuts on the value of $\mathcal{L}_{thr}(\pi(K))$.

in mind that, in the asymmetry extraction, data taken during more than a week are compared and, in that time, the apparatus performances can change because of human operations (that are reduced down to the bare minimum) and other unavoidable reasons like temperature and detector efficiency variations. In spite of the 3 (or 2) target cell configuration chosen to minimize the impact of possible acceptance and efficiency variations in time, many tests have been performed to investigate the stability of the performances of the spectrometer.

During the data taking, hit distributions on the different planes of the tracker, trigger rates, dead-times, e, were continuously monitored- Also sample of data were processed and analysed in real time (see sec.5.2.1) to check the quality of the data . In particular a lot of work has been done before and after the implementation of the LAST trigger.

Before processing the data, the stability of the efficiency of all the tracker planes were checked and unstable detector planes or part of planes were switch off for the event processing.

After the event reconstruction, a lot of effort has been put to select the data collected in spills and runs showing instabilities with respect to the means of the period (see sec.5.2.2, 5.2.3). The final statistic for charged hadrons is given in sec.5.2.3. A further test using the μ-e^- elastic scattering events has been performed. It is described in sec.5.2.4. Finally the RICH stability studies are described in sec. 5.2.5.

5.2.1 Data quality check during data taking

During the data taking, about six runs for each period (three for each sub-period) have been processed and analysed to be sure that no major problems affected the data. These productions have also been used to check the detectors description used in the reconstruction program and to optimize the efficiency of the reconstruction software. The main purpose was, however, a complete check of the quality of the data. In this analysis first of all several particularly relevant kinematical distributions have been measured and compared with the expected distributions, and compared with the distributions obtained from the data collected in the previous periods and with the distributions obtained for the same period but with different alignments or CORAL versions. The distributions have also been compared with the same distributions obtained in the 2007. The distributions which have been scrutinized in this phase are:

- the beam momentum distribution, to evaluate the BMS efficiency;
- the azimuthal and polar angle distributions of the reconstructed beam tracks, to check the stability of the efficiency of the beam track reconstruction;
- the primary vertex coordinates and χ^2, to get informations on the quality of the alignment;
- the scattered muon momentum, azimuthal angle and polar angle distributions, to study overall LAS nad SAS efficiency;
- the distributions of the kinematical quantities used to characterize the DIS events, namely y, x, Q^2;
- the multiplicities and the Collins and Sivers angles distributions.

All the comparisons have been done considering the ratio of the distributions from the data collected in different periods and sub-periods. For the DIS and SIDIS quantities the comparison has been done also trigger by trigger to investigate possible triggers inefficiencies.

A particular effort has been done to understand the performances of the new trigger, the LAST, covering the region at large scattering angle of the muon. In August 2010, after these tests, the new trigger has been introduced in the acquisition.

5.2.2 Bad spill rejection analysis

The bad spill rejection is the first step in the offline data selection. In this analysis several variables grouped in five classes (as summarized in table 5.3) are used. The variables are normalized on the flux of the beam, on the total number of events or on the number of primary vertex. In the identification of the bad spills only the *Macro*, *HCal*, *Trigger* and *Exclusive trigger* classes have been considered since the ECals were not used in the trigger nor in the analysis. Only the events with $Q^2 > 1$ (GeV/c)^2 have been used.

The bad spill identification is done period by period and in each period each spill is identified by a “unique spill number" assigned on the basis of the absolute time of

Table 5.3: Variables used in the bad spill identification with the corresponding normalization variables.

Class	Variables	Normalization variable
Macro	Number of primary vertices (PV)	Number of events
	Number of particles per event	Number of events
	Number of beam particles	Number of primary vertices
	Number of outgoing particles from PV	Number of primary vertices
Ecal	Energy loss by charged particles in ECal1/2	Number of events
	Energy loss by neutral particles in ECal1/2	Number of events
	Number of clusters associated with charged particles in ECal1/2	Number of events
	Number of clusters associated with neutral particles in ECal1/2	Number of events
Hcal	Energy loss by charged particles in HCal1/2	Number of events
	Energy loss by neutral particles in HCal1/2	Number of events
	Number of clusters associated with charged particles in HCal1/2	Number of events
	Number of clusters associated with neutral particles in HCal1/2	Number of events
Trigger	Inclusive trigger	Flux per spill
Exclusive Trigger	Exclusive trigger	Flux per spill
RICH	RICH information	Number of tracks in RICH

the spill. The basic element of the analysis is the mean value which the considered variable assumes in a spill (SMV). In the ideal case it's expected that the SMV has a gaussian distribution with the same mean value in all the spills of a period. The principle of the analysis is quite simple: we assume that each instability in time of the selected variables, i.e. SMV "far" from the mean value over spill of the period, indicates that the spectrometer performance (or the beam) was not stable during that spill, which thus has to be flagged as "bad" spill and rejected. Of course a criteria is needed to establish when to tag a spill as "bad ". To explain the used method it is necessary to introduce the concept of "spill neighbours". Considering two spills A and B, a generic variable V, and the mean value of V in the two spills $\mu(A)$ and $\mu(B)$ we define A as neighbour of B if $|\mu(A) - \mu(B)|$ is smaller than a fixed value m. The bad spills are selected counting the number of neighbours in between the 1200 spills chronological closest to the considered spill. So, considering for example the $Macro$ class, if the number of neighbours of a spill, for one or more variables of the class is smaller than a minimum value N, this spill is tagged as bad. It's important to stress the fact that two spills are defined neighbours is the condition that $|\mu(A) - \mu(B)| < m$ is verified for all the variables of a class and not at least on one of them.

The m value is fixed for each variable V evaluating the root mean square (σ) of V in the full period. The value of m is chosen comparing the different neighbour distributions corresponding to distributions of m equal to 1.0 σ, 1.5 σ, 2.0 σ, 2.5 σ. In fig. 5.6 (left) the distribution of the number of neighbours of the $Macro$

class for real data and different m values are shown. The minimum m for which the neighbour distributions show a clear peak is chosen. In this case we have chosen m=2.5 and m =3 for $HCal$ and $Macro$ classes respectively. The N value has been then fixed for each class requiring a rejection rate of about 0.5 %. The values of m and N for each class are given in table 5.4. Finally, the bad spill identification is repeated after rejecting the bad spill identified in the first pass.

The procedure is quite complex, and to test it a simple Monte Carlo generating the variables V with gaussian distribution has been implemented. In fig. 5.6 (right) the distributions of the number of neighbours for a class of 4 variables are shown and as can be seen, the agreement with the data is good. After the choice of the m values, the bad spills corresponding to N equal to 200, 300, 400, 500, 600, 700, 800 have been rejected, both in the real and simulated data, and for each N value the analysis has been repeated on the good spills. The comparison of real and Monte Carlo data allows to evaluate the rejection rate corresponding to different N values in the ideal case (gaussian distribution of SMV). The number and the percentage of bad spills in the real data for the $Macro$ and the $HCal$ classes are given in table 5.5, columns 2 to 4. The corresponding percentage of bad spills using Monte Carlo data are given in columns 6 and 7 of table 5.5. As can be seen, the chosen values $N = 200$ and $N = 500$ respectively correspond to a rejection rate of 0.5 % and 0.8 % on Monte Carlo data.

Table 5.4: Values of m and N used in the bad spill analysis.

Class	m	N
Macro	2.5 σ	200
Hcal	3 σ	500
Trigger	3 σ	500
Exclusive Trigger	2.5 σ	200

Table 5.5: Number of rejected spills and rejection rate for real and simulated data for "Macro" and "HCal" classes for different N values. The simulated data refer to 4 and 8 gaussian variables, respectively.

Neighbors	*Macro*	*Macro(%)*	*HCal*	*HCal(%)*	Simulated Macro(%)	Simulated HCal(%)
200	50	0.6	7	0.1	0.5	0.03
300	72	0.9	21	0.3	1.2	0.1
400	116	1.5	48	0.6	2.6	0.3
500	198	2.5	101	1.3	5.0	0.8
600	350	4.5	173	2.2	9.0	1.7
700	573	7.3	335	4.3	13.7	3.3
800	1014	13	698	8.9	16.5	6.4

Once the constants are fixed, and the bad spills selected, the software package produces, for each variable, the plot of the SMV as function of the unique spill number in the full period, with the bad spills coloured in red for check purposes. As an example, fig. 5.7 shows the distribution of the mean number of tracks per primary vertex per spill versus unique spill number for the first period. Of course

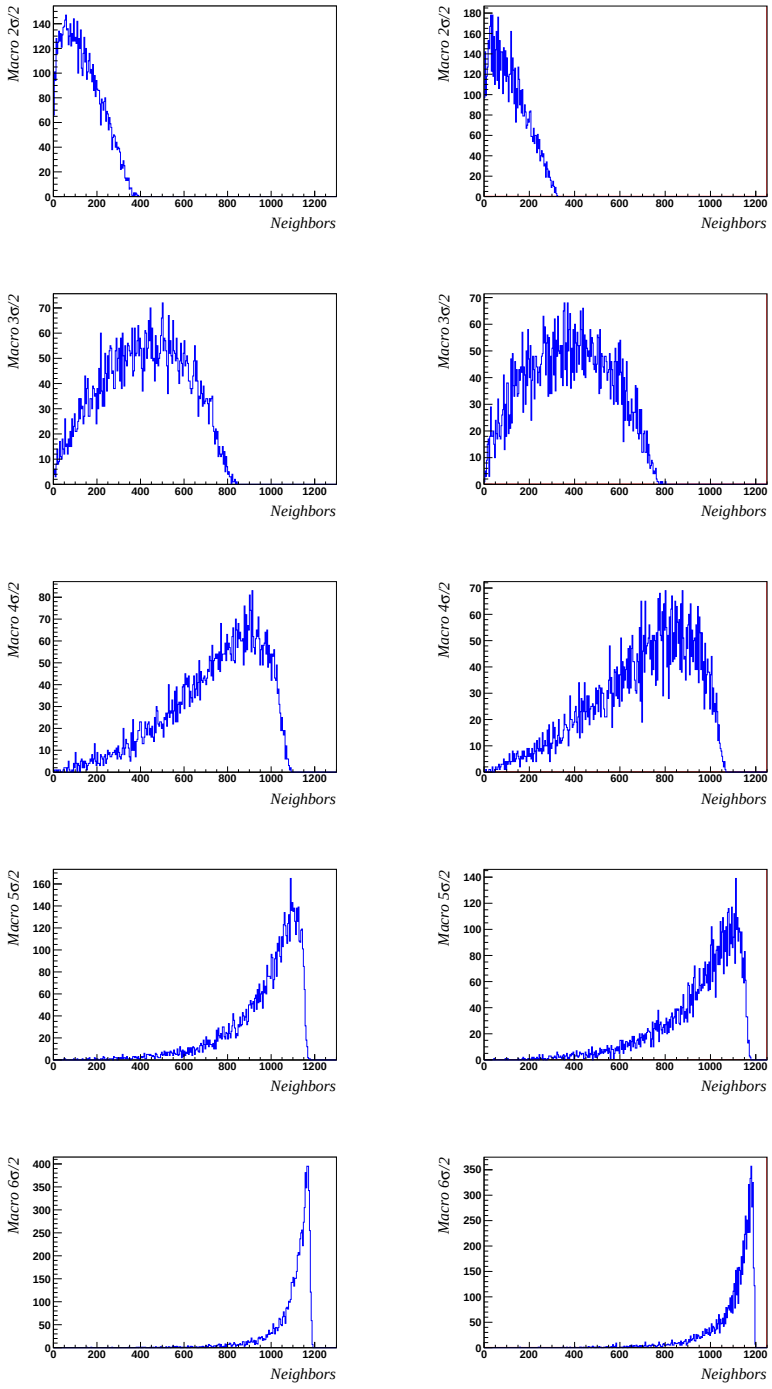

Figure 5.6: Left: distribution of the number of neighbours for real data for m equal to σ, 1.5σ, 2σ, 2.5σ (top to bottom). Right: same distributions for Monte Carlo data.

not for all variables and for all periods the distributions were as expected and a considerable amount of work was needed to investigate all the different cases.

The "chronological order" allows to understand if the bad spills are uniformly

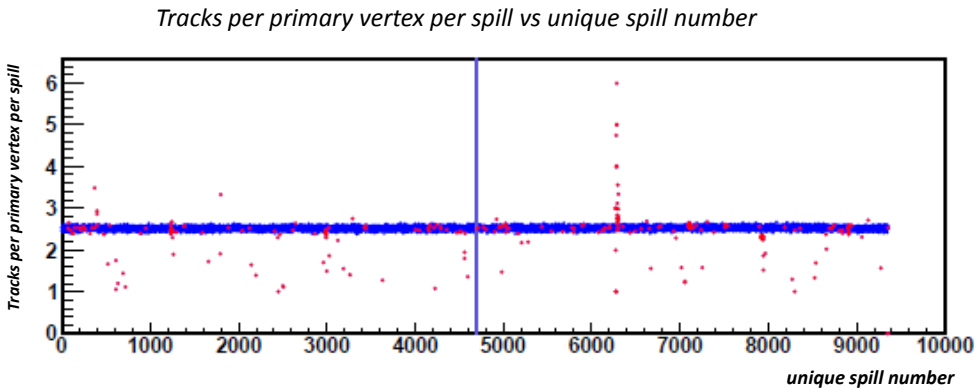

Figure 5.7: Mean number of tracks per primary vertex per spill versus unique spill number. The red dot are the bad spills.

distributed in the time or if they correspond to a particular period of the data taking. So it's possible to obtain information on problems present during considerable time slots. In the case of fig. 5.7 most of the bad spills are randomly distributed in time. A different example is shown in fig. 5.8. In the top plot, the mean number of HCal1 clusters for W24 is shown. A jump in the second sub-period related to inefficiencies of the calorimeter is evident. The reason of this jump have been understood looking at the spatial distribution of the calorimeter clusters in the X-Y plane shown in fig. 5.8 (bottom) for a run of the first sub-period (left) and a run of the second part of the second sub-periods (right). As can be seen in the first part of the period there are large regions of inefficiency which cause the decrease in the number of clusters and deposited energy.

In a few cases this kind of inefficiency was due to high voltage problem and the corresponding runs (or the events collected because of a calorimetric trigger during the whole period) had to be excluded. In most of the cases, however, the problem was a read-out problem which did not affect the trigger and all the events could be used, even if the use of the calorimeters in the analysis turned out to be compromised

At the end of the process the program produces a file compatible with PHAST (see sec. 4.7) which allows to exclude the bad spills during the data processing. In table 5.6 the fraction of events rejected is given.

5.2.3 Bad run rejection analysis

After the exclusion of the bad spills the quality of the selected data is checked with several tests on kinematical variables. This analysis is applied to the events and hadrons which survive to the cuts described in the sec. 5.2.2. The first step of the analysis consists in the comparison of the distributions of the kinematical variables $x, y, Q^2, E_{\mu'}, \theta_{\mu'}, \phi_{\mu'}, E_h, \theta_h, \phi_h, P_{hT}$ obtained in the two sub-periods and in each run. The run by run analysis is done considering, for each variable, the ratio of the distribution obtained for a single run and the distribution for the sub-period to

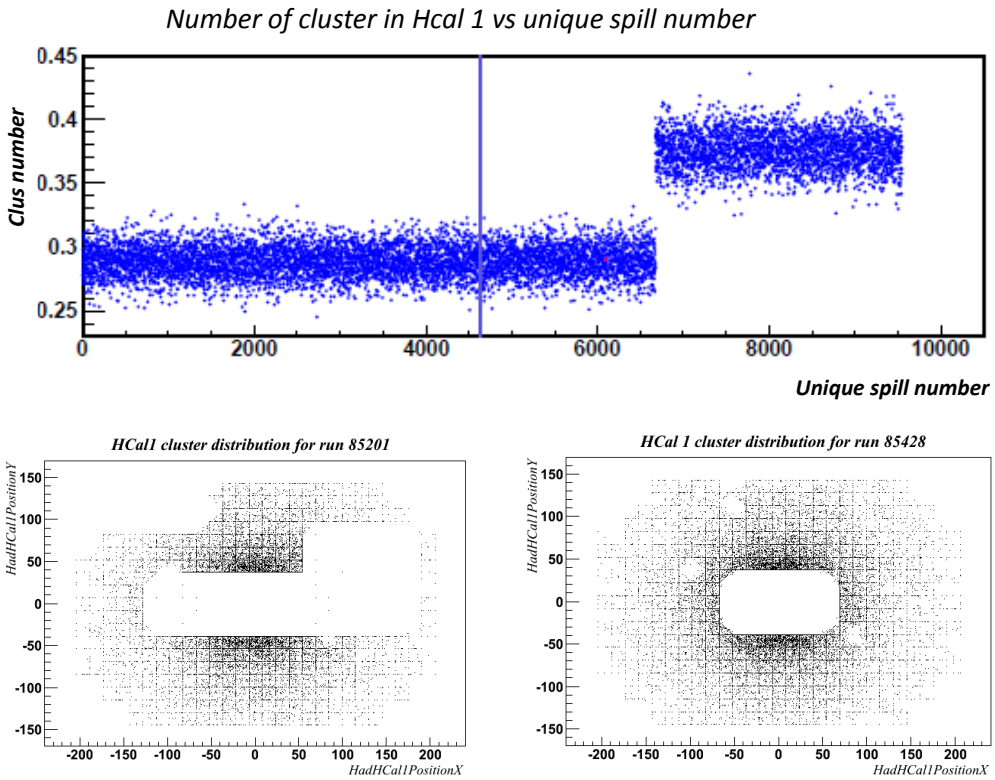

Figure 5.8: Top: Mean number of HCal1 clusters per spill. Bottom: distribution of HCal1 clusters in the X-Y plane for a run collected in the first (left) and second (right) part of the period.

Table 5.6: Percentage of rejected events after the bad spill rejection.

Period	Percentage of rejected events
1	2,19%
2	5,42%
3	3,03%
4	4,22%
5	2,07%
6	2,28%
7	5,14%
8	3,49%
9	2,42%
10	2,91%
11	2,09%
12	3,15%

which the run belongs. The ratio is fitted with a constant function and the χ^2 probability of the fit is evaluated to spot out blocks of runs showing instabilities

with distributions of the kinematical variables. After a first cleaning of the data sample by removing these runs the test is repeated and the runs with kinematical distributions significantly different from the mean are rejected. In this step a run is removed if

- $P_v \leq 10^{-5}$ for at least one variable where P_v is the probability of the χ^2 for the variable v,
- $P_{tot} \leq 10^{-4}$, where P_{tot} is the sum of the χ^2 calculated for all the 10 variables v.

This analysis rejected in total about 6 % of the total hadrons.

The run by run stability check has been done also monitoring the position of the K^0 mass peak and the number of reconstructed K^0 normalized to the number of primary vertexes. The runs with a number of K^0 per primary vertex more than three standard deviations away from the mean of the distribution calculated for the period are excluded. The data rejected because of this test is very low, less than 1 % for each period.

The final statistics for the one and two hadron analysis is given in table 5.7 for all the data taking periods.

Table 5.7: Final statistics of the 1 hadron and the 2 hadron samples.

Period	h^+	h^-	h^+h^-pairs
1	2136694	1679411	1688231
2	1979658	1557481	1570083
3	2130282	1670615	1691234
4	2286439	1797609	1804717
5	2585990	2032504	2044274
6	3735831	2941097	2982732
7	3854452	3036795	3075647
8	4638938	3658840	3704061
9	4482275	3527844	3568240
10	6693964	5273269	5312771
11	4500112	3537206	3563477
12	4482967	3524894	3558312
total	43507602	34237565	34563779

5.2.4 μ - e^- elastic scattering as monitor for the stability

The stability of the spectrometer has been checked with an analysis applied for the first time to the 2007 data. This method is based on the fact that the μ - e^- elastic scattering is characterized by a fixed value of x. The idea is to evaluate the x value of the elastic-scattering peak for each run and to compare the results obtained for all the runs of a period, since the x value is very sensitive to instability of the spectrometer, problems in the detector alignment, or other instability related to the magnetic fields.

The incoming muons can interact with the atomic electrons via elastic scattering. In this case the value of $x = Q^2/2m_e\nu$ is expected to be 1. Considering the nucleon mass in the calculation of x one obtains:

$$x = \frac{Q^2}{2M_N\nu} = \frac{Q^2}{2m_e\nu} \cdot \frac{m_e}{M_N} = \frac{m_e}{M_N} = 5.466 \cdot 10^{-4}. \tag{5.3}$$

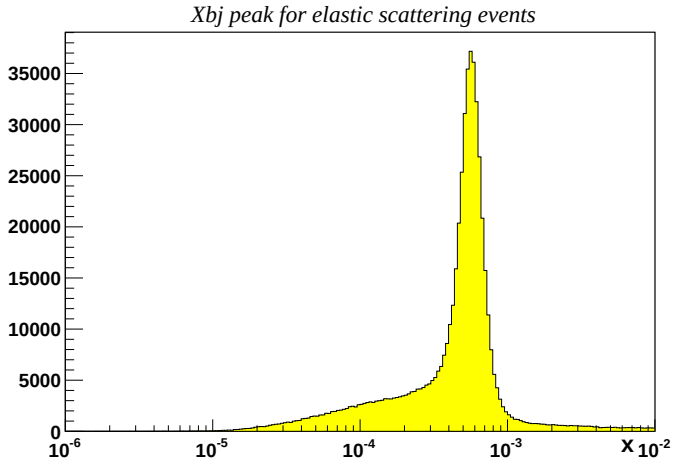

Figure 5.9: x distribution for Q^2 <1 (GeV/c)^2 and two outgoing particles from the primary vertex (scattered μ and a negative particle).

Fig. 5.9 shows the distribution obtained for a single run of period 9 requiring Q^2 <1 (GeV/c)^2 and two outgoing particles from the primary vertex (scattered μ and a negative particle). The cuts applied to select the μ - e^- elastic scattering events are:

- Q^2<1 (GeV/c)^2;
- two outgoing particles from the primary vertex;
- One of this particles as to be identified as the scattering muon (based on the CORAL definition, see sec. 5.1) and the other must have a negative charge;
- a μ scattering angle θ< 0.00487 rad, since in the COMPASS kinematics the maximum value is θ_{max}=0.00487 rad;
- a transverse momentum of the negative particle smaller than 0.1 GeV/c, to exclude large angle particles.

The effects of this cuts are shown in fig. 5.10. The cut on the scattering angle rejects events at large x, while the cut on the transverse momentum of the negative particle rejects events in the full x range. In particular the cut on the transverse momentum has been applied because it allows one to improve the fit of the background. The events in which the two outgoing particles are the scattered muon and a positive particle are used to evaluate the background and from now on they will be

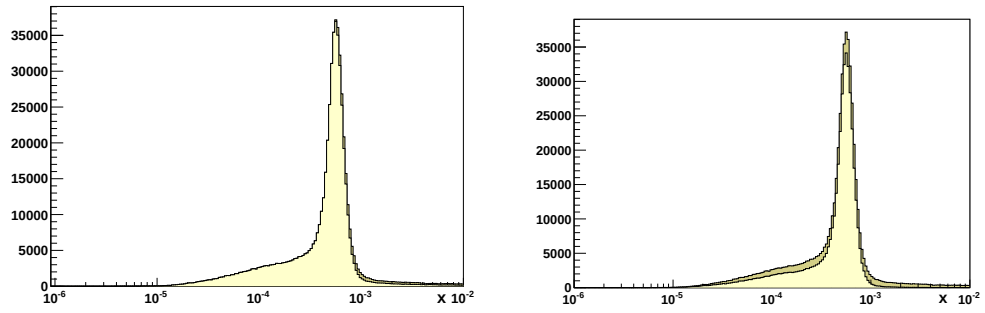

Figure 5.10: x distribution with (bright) and without (dark) the cut on the scattering angle (left). x distribution with (bright) and without (dark) the cut on the transverse momentum of the electron (right).

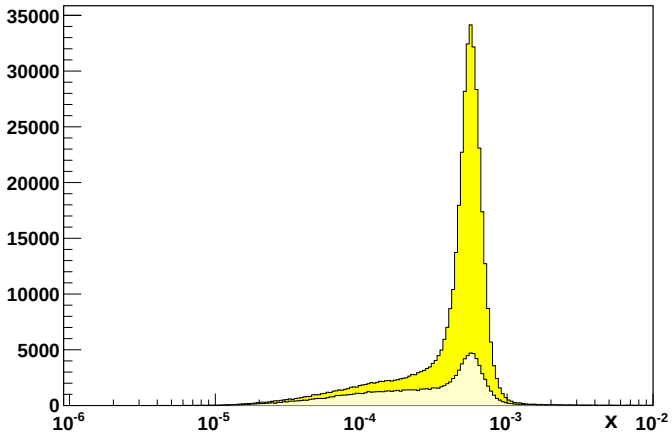

Figure 5.11: x distribution for elastic scattering events candidates and for the "background" events.

indicated as background events. Their x distribution is compared to the distribution of the elastic scattering events in fig. 5.11.

The functions used to fit the x distribution of the selected events contains the function

$$(a + bx + cx^2)(1 - d \cdot e^{(f \cdot x)}), \tag{5.4}$$

used to describe the background, and the function

$$\frac{A}{(x - x_0)^2 + (\frac{B}{2})^2}, \tag{5.5}$$

used to describe the elastic scattering signal.

The fit result is shown in fig. 5.12. The quality of the fit is good enough for the stability studies. In fact, we only need to monitor the stability of the distribution and in particular the stability of the x_0 values from the different runs and different

periods. For this reason we did not put a particular effort to understand the absolute value of x_0. The values of x_0 for each 2010 run are shown in fig. 5.13 (right). The results from the different periods and the different runs are compatible and no evidence of instability is observed. The situation was completely different in the 2007 data, as can be seen in fig. 5.13. This confirms the better quality of the data collected in the 2010 run.

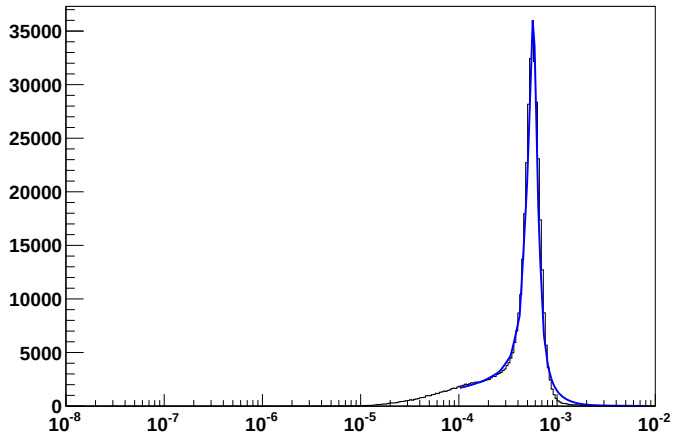

Figure 5.12: x distribution for the elastic events and background. The blue line represents the fit of the elastic peak.

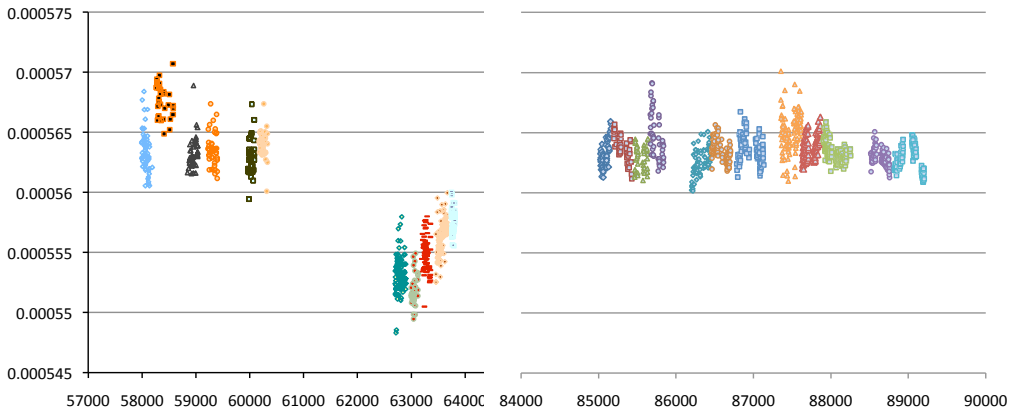

Figure 5.13: x_0 values run by run and for different periods of the 2007 (left) and 2010 (right) runs.

5.2.5 RICH stability in 2010

The stability of the RICH detector has been studied using the data sample selected with the data quality studies described before . The first step of this investigation

consisted in the *spill*-by-*spill* analysis of the six likelihood values associated to the different particles. The procedure is the same described in sec. 5.2.2 and no more spills have been excluded by this analysis. The spill mean value of the likelihood distribution for pions and kaons versus the spill number for period 6 is shown in fig. 5.14.

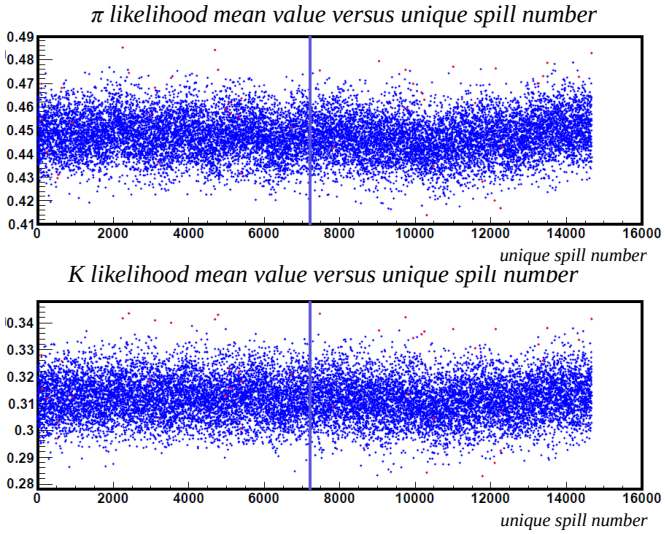

Figure 5.14: The Likelihood mean value distribution for pions and kaons versus the spill number for period 6.

The run-by-run analysis, performed after the spill-by-spill analysis, consists in the study of the stability of ratio between the number of identified particles and the number of unidentified particles evaluated for each run. These tests (performed separately for the one-hadron and the two-hadron samples), have been done also dividing the detector in four regions defined by the polar angle ϑ_{RICH} of the tracks at the entrance window of the RICH:

- $\vartheta_{RICH} < 30$ mrad, to define the very central region, close to the beam pipe;
- 30 mrad $< \vartheta_{RICH} <$ 110 mrad, to define the region in which the Cherenkov photons are mainly detected in the MAPMT;
- 110 mrad $< \vartheta_{RICH} <$ 200 mrad, to define the region in which the Cherenkov photons are detected in the MAPMT and in the MWPC;
- $\vartheta_{RICH} >$ 200 mrad, to define the outer region in which the Cherenkov photons are detected in the MWPC.

The stability of the data is studied looking at the distribution of the ratios π/h for each run of a period. The runs having a π/h ratio which differs from the mean value of all runs of the period by more than 4σ (where σ is the r.m.s. of the distribution) are rejected. Fig. 5.15 shows the ratio between the number of π over all charged hadrons for ϑ_{RICH} >200 mrad. The red lines show the $\pm 4\sigma$ cut. The rejected hadrons are 1.7% and 2.1% in the one-hadron and two-hadron case, respectively, when all the periods are considered. The final samples of identified hadrons have been obtained using only the runs surviving both in the one-hadron and in the two-hadron tests.

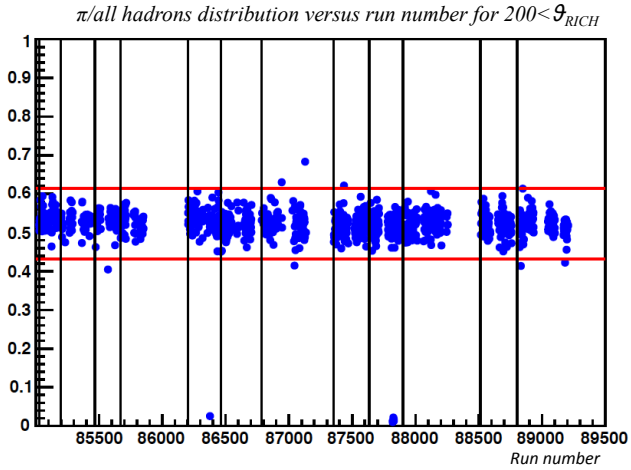

Figure 5.15: π over all hadrons for ϑ_{RICH} >200 mrad; the red lines represent the $\pm 4\sigma$ value.

5.3 Measurement of the transverse spin asymmetries

As discussed in sec. 4.3 the COMPASS target consists of three cells with opposite polarization orientation. In a data taking period, typically up to 12 days long, the orientation of the polarization of each cell is inverted after 4 to 5 days defining two sub-periods. The asymmetries are measured as function of x, z and M_{inv} in two-hadron analysis (as function of x, z and P_{hT} in one-hadron analysis), each time integrating over on the other variables. The binning used in two-hadron and Collins Asymmetries extraction are given in table 5.8 and 5.9, respectively.

Table 5.8: Binning used in the two-hadron asymmetries extraction.

bin	x	z	M_{inv} (Gev/c^2)
1	$[0.003 - 0.008]$	$[0.20 - 0.25]$	$[0.0 - 0.4]$
2	$[0.008 - 0.013]$	$[0.25 - 0.30]$	$[0.4 - 0.5]$
3	$[0.013 - 0.020]$	$[0.30 - 0.35]$	$[0.5 - 0.6]$
4	$[0.020 - 0.032]$	$[0.35 - 0.40]$	$[0.6 - 0.7]$
5	$[0.032 - 0.050]$	$[0.40 - 0.50]$	$[0.7 - 0.8]$
6	$[0.050 - 0.080]$	$[0.50 - 0.65]$	$[0.8 - 0.9]$
7	$[0.080 - 0.130]$	$[0.65 - 0.80]$	$[0.9 - 1.0]$
8	$[0.130 - 0.210]$	$[0.80 - 1.00]$	$[1.0 - 1.2]$
9	$[0.210 - 0.700]$	/	$[1.2 - 1.6]$
10	/	/	$[1.6 - 100]$

The procedure used to extract the transverse spin asymmetries is the same in the case of single hadron or hadron pair production. What changes is the azimuthal angle defined by the hadrons and the number of modulations expected in the cross-section. In the following we will refer to a general ϕ angle which indicates $\phi_C = \phi_h + \phi_S - \pi$ and $\phi_{RS} = \phi_R + \phi_S - \pi$ in the case of single hadron or hadron pair production,

Table 5.9: Binning used in the one-hadron asymmetries extraction.

bin	x	z	P_{hT} (Gev/c)
1	$[0.003-0.008]$	$[0.20-0.25]$	$[0.10-0.20]$
2	$[0.008-0.013]$	$[0.25-0.30]$	$[0.20-0.30]$
3	$[0.013-0.020]$	$[0.30-0.35]$	$[0.30-0.40]$
4	$[0.020-0.032]$	$[0.35-0.40]$	$[0.40-0.50]$
5	$[0.032-0.050]$	$[0.40-0.50]$	$[0.50-0.60]$
6	$[0.050-0.080]$	$[0.50-0.65]$	$[0.60-0.75]$
7	$[0.080-0.130]$	$[0.65-0.80]$	$[0.75-0.90]$
8	$[0.130-0.210]$	$[0.80-1.00]$	$[0.90-1.30]$
9	$[0.210-0.700]$	/	$[1.30-100]$

respectively.

Considering a generic cell i the number of h^+h^- pairs, or hadrons in single hadron analysis, produced by the scattering of lepton off a transversely polarized target is given by (see sec. 3.2):

$$N_i^{\pm}(\phi) = N_i^0(1 \pm f S_T D_{NN} A_{2h(Coll)} sin(\phi) \pm .....) \tag{5.6}$$

where:

- $\pm$ indicates the transverse spin orientation of the proton;
- f is the target dilution factor;
- S_T is the target polarization;
- D_{NN} is the spin transfer parameter;
- $\phi = \phi' + \phi_S - \pi$ with $\phi'= \phi_R$ in the two-hadron asymmetries case and $\phi' =\phi_h$ in the Collins asymmetry case. The ϕ_R and ϕ_h angles have been defined in sec. 3.2 and sec. 3.1, respectively. Note that ϕ_S, the azimuthal angle of the nucleon spin, is always calculated for polarization orientation upwards in the laboratory system;
- $N_i^0=N_{beam}\sigma L_i$, where N_{beam} is the useful number of incident μ^+, σ the unpolarized cross-section and L_i the length of cell i.

In a real experiment the number of detected hadrons depends on the ϕ acceptance and efficiency. As it will be clear in the following, the only acceptance contribution which affects our measurement has the same azimuthal modulation as the asymmetry we want extract. So, taking into account this contribution, eq. 5.6 can be rewritten as:

$$N_i^{\pm}(\phi) = N_i^0(1 \pm \epsilon sin(\phi))(1 + a_i sin(\phi)), \tag{5.7}$$

where $\epsilon = fS_T D_{NN} A_{2h(Coll)}$ and a_i is the amplitude of the corresponding modulation in the acceptance of the cell i.

5.3.1 The quadrupole ratio method

To measure the asymmetries with the "quadrupole ratio" (QR) method, the middle cell is split in two parts obtaining the final configuration of the target cells shown in fig.5.16 in the the case the first cell has polarization in the "up" direction in the first sub-period. With reference to the conventions of fig. 5.16 combining the data

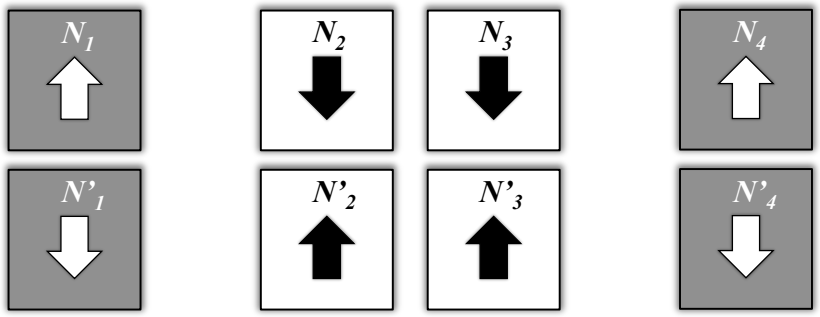

Figure 5.16: Cells configuration.

of two sub-periods it's possible to measure the quantities:

$$F^{QR}(\phi) = \frac{N_1(\phi) \cdot N_2'(\phi) \cdot N_3'(\phi) \cdot N_4(\phi)}{N_1'(\phi) \cdot N_2(\phi) \cdot N_3(\phi) \cdot N_4'(\phi)}, \tag{5.8}$$

where $N_i(\phi)$ and $N_i'(\phi)$ are the number of events with vertex in cell i in the two sub-periods. Replacing in eq. 5.8 the $N_i^{\pm}$ definition given in eq. 5.7 and neglecting terms of the second order in the amplitudes of the modulations one obtains:

$$F^{QR}(\phi) \approx C(1 + [(a_1 - a_1') - (a_2 - a_2') - (a_3 - a_3') + (a_4 - a_4') + 8\epsilon] sin(\phi)), \tag{5.9}$$

where

$$C = \frac{N_1^0 N_2'^0 N_3'^0 N_4^0}{N_1'^0 N_2^0 N_3^0 N_4'^0} = 1, \tag{5.10}$$

since the beam flux of the four cells is the same in all the four cells.

Defining $e_i = (a_i - a_i')$ the eq.5.9 becomes:

$$F^{QR}(\phi) \approx \left\{ 1 + (e_1 - e_2 - e_3 + e_4 + 8\epsilon) sin(\phi) \right\}. \tag{5.11}$$

Fitting the $F^{QR}(\phi)$ quantities with $f(\phi) = p_0(1 + p_1 sin(\phi))$ one obtains the measured asymmetry $\epsilon_m = p_1/8$ which is related to the real asymmetry ϵ by

$$\epsilon = \epsilon_m - \frac{(e_1 - e_2 - e_3 + e_4)}{8}. \tag{5.12}$$

As evident from eq.5.11 a bias can only be due to possible changes of the cell acceptances between the two sub-periods and not to different geometrical acceptance of the cells. Such a bias cannot be separated from the real asymmetry, but it disappears if the acceptance variations in the four cells (or in cells 1 and 2 and cells 3 and 4) are the same. Very likely this is true, and in the following it is referred as "Reasonable Assumption (RA)".

To extract the asymmetry ϵ, one has to apply a small correction due to the finite size of the ϕ bins. Usually the ϕ range is divided into 16 or 8 bins of equal width Δ. In each bin the number of events is a constant times the mean value of the expected distribution. In particular for a $sin(\phi)$ modulation in the bin i, the mean value is:

$$\big\langle sin(\phi_i) \big\rangle = \frac{1}{\Delta} \int_{\phi-\Delta/2}^{\phi+\Delta/2} sin\phi d\phi = \frac{2}{\Delta} sin\frac{\Delta}{2} sin\phi. \tag{5.13}$$

Thus fitting the data with the function $f(\phi) = p_0(1 + p_1 sin(\phi))$ the measured asymmetry has to be calculated as

$$\epsilon_m = \frac{p_1}{8} \frac{1}{\frac{2}{\Delta} sin\frac{\Delta}{2}}. \tag{5.14}$$

When 16 ϕ bins are used, the correction can be neglected because it is at the level of 0.6 %, much less than the typical statistical error.

The method described here, namely the quadrupole ratio (QR) method, is based on 4 target cells and two sub-periods. A similar method, called in the following the double ratio (DR) method, consists in considering separately the upstream and downstream cells to build the quantities:

$$\begin{aligned} F_{up}^{DR}(\phi) &= \frac{N_1 \cdot N_2'}{N_1' \cdot N_2}, \\ F_{down}^{DR}(\phi) &= \frac{N_3' \cdot N_4}{N_3 \cdot N_4'}. \end{aligned} \tag{5.15}$$

This method gives two independent measurements of the asymmetries. The weighted mean of the results obtained from F_{up}^{DR} and F_{down}^{DR} should of course give the result obtained with the QR. The DR has been the first to be used in the measurements of transverse spin asymmetries and was developed when the target consisted of two cells only.

In the case one wants to measure amplitudes of more modulations in combinations of ϕ' and ϕ_S, these "1D" methods can still be used considering one modulation at the time. A possible problem is that the acceptance can introduce correlations

between the measured amplitudes. To avoid this problem, the "2D" QR and DR methods have been developed. They consist in evaluating the F^{QR} and F^{DR} quantities in bins of (ϕ', ϕ_S) and using a fitting function in which all the modulations appear. Still, in the case of very low statistic, these methods based on ratios of number of events are not safe. For this reason the binned and unbinned maximum Likelihood methods have been developed. Recently all the COMPASS results are produced with the second method which is described in the following.

5.3.2 The unbinned maximum likelihood method

The unbinned maximum likelihood method [80, 57] has been developed to overcome the problem of statistical fluctuations in the ratio of small numbers. In this method a probability density function $p(\phi', \phi_S; \epsilon_k)$ which depends by the considered cell i and is proportional to the product of the acceptance and the physics modulation function is associated to each hadron. The cross section is parametrized in such a way that all possible modulations can be included. For instance, in the case of single hadron asymmetries, the used expression of the cross section is:

$$\begin{aligned}\sigma_{\pm}(\phi_h, \phi_S) \propto 1 + \epsilon_{u,1} cos(\phi_h) + \epsilon_{u,2} sin(2\phi_h) \pm \Big[& \epsilon_C sin(\phi_h + \phi_S) + \epsilon_S sin(\phi_h - \phi_S) + \\ & + \epsilon_2 sin(3\phi_h - \phi_S) + \epsilon_4 cos(\phi_h - \phi_S) + \epsilon_5 sin(\phi_S) + \epsilon_6 sin(2\phi_h - \phi_S) + \\ & + \epsilon_7 cos(\phi_S) + \epsilon_8 cos(2\phi_h - \phi_S) \Big].\end{aligned} \tag{5.16}$$

Here $\epsilon_{u,1}$ and $\epsilon_{u,2}$ are the amplitudes of the unpolarized modulations and ϵ_i, with i=C,S,2,4,5,6,7,8, are amplitudes of the spin dependent modulations. In probability distribution function the terms with the acceptance in ϕ' and ϕ_S are neglected because the extracted spin dependent asymmetries do not depend on it, but only on the (unknown) acceptance variations between the two sub-periods. As in the case of DR and QR, such variations can introduce a bias if the RA is not verified. The estimator used for the evaluation of the raw asymmetries is based on an extended unbinned maximum likelihood method. The likelihood function is built as the product of the probability densities p corresponding to each hadron i from each target cell. The likelihood for hadrons from a given target cell in one period is written as

$$\mathcal{L} = \left(e^{-I^+} \prod_{i=0}^{N^+} p^+(\phi_{h,i}, \phi_{S,i}) \right)^{\frac{1}{N^+}} \cdot \left(e^{-I^-} \prod_{i=0}^{N^-} p^-(\phi_{h,i}, \phi_{S,i}) \right)^{\frac{1}{N^-}}. \tag{5.17}$$

The + and − signs refer to the orientation of the target polarisation in the two sub-periods and $N^{\pm}$ is the corresponding total number of hadrons. The quantities $I^{\pm}$ are the integrals of the probability densities over ϕ_S and ϕ_h given by:

$$I_i^{\pm} = \int_0^{2\pi} \int_0^{2\pi} d\phi' d\phi_S p_i^{\pm}(\phi', \phi_S). \tag{5.18}$$

The likelihood function is built for all the bins used in the analysis and the minimization is performed using the MINUIT package.

5.4 Systematic effects

The evaluation of the systematic error has been done considering different effects which can affect the measurement. All the tests have been applied to the final data sample, after the rejection of the bad spills and bad runs.

The azimuthal stability of the apparatus has been estimated with two different tests: the "T-test" and the "RA-test".

The systematic errors due to the variation of acceptance between two sub periods have been estimated looking at non-physical (false) asymmetries. Finally the compatibility of the results from the different periods of data taking and from the different methods has been investigated. All these tests have been performed for the Collins asymmetries, separately for positive and negative hadrons, and for the two-hadron asymmetries.

5.4.1 Stability of the acceptance

The stability of the acceptance in the azimuthal angles has been first investigated performing 2 different tests: the "T-Test" and the "RA-Test". The results are then combined for a final test of the data quality.

The T − test

If we define the function:

$$T(\phi) = \frac{N_1 \cdot N_2 \cdot N_3 \cdot N_4}{N'_1 \cdot N'_2 \cdot N'_3 \cdot N'_4} \tag{5.19}$$

and we neglect terms $\mathcal{O}(sin^2(\phi))$, using eq. 5.7 we obtain:

$$T(\phi) = T_0[1 + (e_1 + e_2 + e_3 + e_4)sin(\phi)], \tag{5.20}$$

where $e_i = (a_i - a'_i)$ are the same quantities defined before and represent the change of acceptance of the cell i between the two sub-periods. Here

$$T_0 = \frac{N_{01} \cdot N_{02} \cdot N_{03} \cdot N_{04}}{N'_{01} \cdot N'_{02} \cdot N'_{03} \cdot N'_{04}}. \tag{5.21}$$

In the ideal case in which the acceptance does not change in the two sub-periods, e_i=0 for each cell i, and the expected value for $T(\phi)$ is constant in ϕ and equal to T_0.

The T-test is performed fitting $T(\phi)$ with a function $f(\phi) = const \cdot [1 + \alpha sin(\phi)]$ and checking if the amplitude α of the modulation is less than 2 standard deviations from zero. The results of the fit and its error are indicated as T and σ_T. The main idea is that the acceptance in the different cells are expected to compensate, as from eq. 5.11. Still, the compensation can be marginal for large variations, and 2 standard deviations from zero are considered a safe limit.

The RA − test

In the Reasonable Assumption (RA), the variations of the acceptance in the 4 cells are considered to be the same, i.e. $e_i = e$ for each i. This can be tested in the following way. For each cell the ratio of the azimuthal distributions obtained for the two sub−periods is fitted with $c \cdot (1 + \varepsilon_i \cdot sin(\phi))$ and each amplitude is obtained from the fit:

$$\begin{aligned}
\frac{N_1(\phi)}{N_1'(\phi)} &\rightarrow \epsilon_1 = (e_1 + 2\epsilon), \\
\frac{N_2(\phi)}{N_2'(\phi)} &\rightarrow \epsilon_2 = (e_2 - 2\epsilon), \\
\frac{N_3(\phi)}{N_3'(\phi)} &\rightarrow \epsilon_3 = (e_3 - 2\epsilon), \\
\frac{N_4(\phi)}{N_4'(\phi)} &\rightarrow \epsilon_4 = (e_4 + 2\epsilon).
\end{aligned} \tag{5.22}$$

If the RA holds, $e_i = e$ for each i and the amplitude of the physic modulation ϵ is given by ϵ=$(\epsilon_1 - \epsilon_2 - \epsilon_3 + \epsilon_4)/8$ while the sum of the asymmetries ϵ_i give the amplitude $T = 4e$. It's easy to see that:

$$\begin{aligned}
E[\epsilon_1] &= (\frac{T}{4} + 2\epsilon) = \alpha_1, \\
E[\epsilon_2] &= (\frac{T}{4} - 2\epsilon) = \alpha_2, \\
E[\epsilon_3] &= (\frac{T}{4} - 2\epsilon) = \alpha_3, \\
E[\epsilon_4] &= (\frac{T}{4} + 2\epsilon) = \alpha_4.
\end{aligned} \tag{5.23}$$

The four measured amplitudes ε_i are used to build the following χ^2_{RA} with 2 degrees of freedom:

$$\chi^2_{RA} = \sum_{i=1-4} \big(\frac{\varepsilon_i - \alpha_i}{\sigma_i}\big)^2, \tag{5.24}$$

where σ_i is the error on each amplitude ε_i.

The combination of the T − test and the RA − test

The quantities given by the T−test and the RA−test have been combined to give a unique χ^2 probability (T+RA) for each period of data taking and separately for each transverse spin asymmetry. The final χ^2_{T+RA} is:

$$\chi^2_{T+RA} = \chi^2_{RA} + \big(\frac{T}{2 \cdot \sigma_T}\big)^2, \tag{5.25}$$

with 3 degrees of freedom. All these studies have also been performed using the azimuthal distributions extracted in each bin of x and also integrating over x. It was checked that there is no relevant dependence from the kinematics and that the T+RA values are similar to the unbinned case.

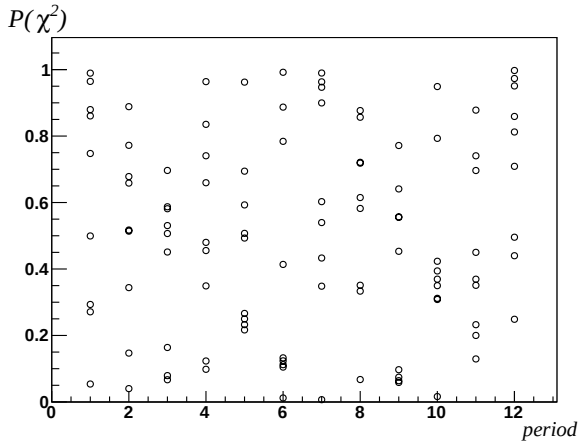

Figure 5.17: χ^2 probabilities for all periods in each of the nine x bins.

As an example, fig. 5.17 shows the probabilities of χ^2_{T+RA} for all periods in each x bin, while in the table 5.10 the results obtained for the integrated distributions are given. The probability values are very reasonable, and do not point at any particular problem. The conclusion of this work is that any period of the 2010 data taking looks affected by large systematic effects and the data collected in all the periods have been used to evaluate the asymmetries. The systematic errors have been evaluated with different methods, as discussed in the following sections.

Table 5.10: probabilities of χ^2(T+RA) obtained without making any bin on the kinematical variables.

Period	T+RA (Collins)	T+RA (Two-hadron)
1	91%	75%
2	58%	89%
3	72%	69%
4	93%	76%
5	85%	73%
6	94%	88%
7	87%	79%
8	65%	80%
9	97%	70%
10	33%	91%
11	83%	79%
12	83%	88%

5.4.2 False asymmetries

To estimate the systematic errors due to possible acceptance variations we have used the "false asymmetries" (FA) method which consists in using the same number of events entering eq. 5.20 (from which we evaluate the physical asymmetries) but

combining them in such a way to evaluate asymmetries which are expected to be zero. This is the case for the following functions:

$$\begin{aligned} FA^{ext}(\phi) &= \frac{N_1 \cdot N_4'}{N_1' \cdot N_4}, \\ FA^{int}(\phi) &= \frac{N_2' \cdot N_3}{N_{\prime 3} \cdot N_2}. \end{aligned} \tag{5.26}$$

By fitting FA^{ext} and FA^{int} with the function $const \cdot (1 + \epsilon \cdot sin(\phi))$, the ϵ value is expected to be compatible with zero for both functions. The asymmetries measured for these configurations can be different from zero only because of systematic effect due to acceptance variations, thus they can be used to quantify (e_1-e_4) and (e_3-e_2).

To have an estimate of the systematic errors the absolute value of the difference

$$FA_- = |FA_{ext} - FA_{int}| / \sqrt{\sigma_{int}^2 + \sigma_{ext}^2}\,, \tag{5.27}$$

and the sum

$$FA_+ = |FA_{ext} + FA_{int}| / \sqrt{\sigma_{int}^2 + \sigma_{ext}^2}\,, \tag{5.28}$$

both normalized to the statistical error, are computed and the value 0.68 (the medium value of $|FA_{ext} - FA_{int}|$ is subtracted in quadrature to each of them. If $|FA_\pm| \leqslant 0.68$, it is put equal to zero.

The arithmetic mean

$$\alpha = \frac{\sqrt{FA_-^2 - 0.68^2} + \sqrt{FA_+^2 - 0.68^2}}{2} \tag{5.29}$$

is eventually calculated for each period and bins of x.

After having checked that the α values are similar for all the periods, the systematic error in each bin is calculated as the arithmetic mean over the 12 periods:

$$\sigma_{sys} = \frac{\sum_i \alpha_i}{12 \cdot 9}. \tag{5.30}$$

In fig. 5.18 the $\sigma^{sys}/\sigma^{stat}$ values for two-hadron asymmetries in the 9 x bins are plotted.

The systematic errors from this test is the mean of the final errors in the different bins. They are:

- $0.45 \cdot \sigma_{stat}$ for the Collins asymmetry, positive hadrons;
- $0.51 \cdot \sigma_{stat}$ for the Collins asymmetry, negative hadrons;
- $0.71 \cdot \sigma_{stat}$ for the two-hadron asymmetry.

5.4.3 Systematics from spectrometer acceptance

To evaluate the systematics errors, the asymmetries have also been evaluated dividing the spectrometer into top and bottom and into left and right. The azimuthal angle of the scattered muon in the laboratory frame has been used to associate the

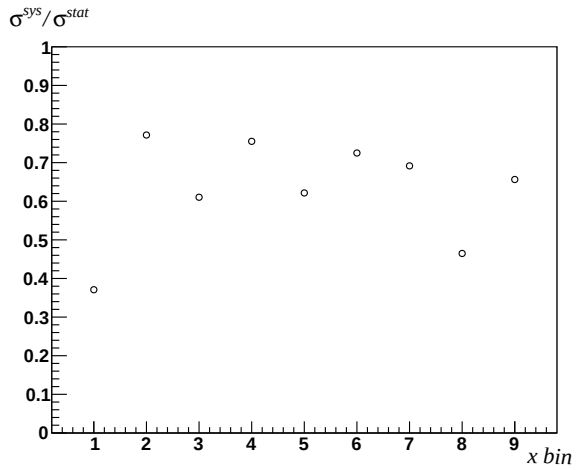

Figure 5.18: $\sigma^{sys}/\sigma^{stat}$ obtained from the false asymmetries in the two hadron asymmetry analysis, in the 9 x bins.

events to the top or to the bottom and to the left or to the right regions. The evaluation of the systematic error has been done in a very similar way to that described in sec. 5.4.2. In this case A_{top} and A_{bottom}, the asymmetries evaluated respectively for top and bottom part of the spectrometer, and A_{left} and A_{right}, the asymmetries evaluated respectively for left and right of the spectrometer, are compared. From

$$A_{top-bottom} = |A_{top} - A_{bottom}|/\sqrt{\sigma^2_{top} + \sigma^2_{bottom}}, \tag{5.31}$$

and

$$A_{left-right} = |A_{left} - A_{right}|/\sqrt{\sigma^2_{left} + \sigma^2_{right}}, \tag{5.32}$$

the value 0.68 has been subtracted in quadrature to each of them, i.e.

$$\alpha = \sqrt{A^2 - 0.68^2} \tag{5.33}$$

for each period and bins of x separately for top-bottom and left-right. The systematic error has been calculated as the arithmetic mean

$$\sigma_{sys} = \frac{\sum_i \alpha_i}{12 \cdot 9} \cdot \sigma_{stat} \tag{5.34}$$

over the 12 periods and the 9 x bins for positive and negative hadrons. The systematic errors evaluated from this test are:

	Collins h+	Collins h-	two-hadrons
$\sigma_{sys}(top/bottom)$	$0.53 \cdot \sigma_{stat}$	$0.50 \cdot \sigma_{stat}$	$0.73 \cdot \sigma_{stat}$
$\sigma_{sys}(left/right)$	$0.45 \cdot \sigma_{stat}$	$0.60 \cdot \sigma_{stat}$	$0.81 \cdot \sigma_{stat}$

5.4.4 Compatibility among periods

A further evaluation of the systematic error has been done comparing the results for the physical asymmetry obtained from the different periods. In fig. 5.19 the Collins asymmetries for positive (top) and negative (bottom) hadrons as function of x from

the 12 data taking periods of 2010 are shown. The compatibility has been evaluated considering for each period the weighted mean value of asymmetries measured in the nine x bins. No evidence of systematic errors, both for one-hadrons and two-hadrons asymmetries, has been observed.

5.4.5 Compatibility among different methods

In sec. 5.3.1 we have seen that there are different methods to evaluate the asymmetries, in particular the quadrupole ratio method and the Unbinned likelihood estimator (UL) method have been described. The Collins and two-hadron asymmetries have been measured with both methods and the results have been compared (The final results are those obtained with the UL method). The comparison of the results is performed using the quantities:

$$\Delta_{ij} = \frac{A_i - A_j}{\sigma_i}, \tag{5.35}$$

where A_i and A_j are the same asymmetries measured with different methods. Fig. 5.20 shows the Δ_{ij} distributions obtained, comparing the QR with UL and the DR with UL results for the Collins asymmetries measured, for each period, as function of x,z and P_{hT}. Both distributions have a r.m.s of about 0.2. The same result has been obtained looking at the Δ_{ij} distributions in the two-hadron analysis (see fig. 5.21, 5.22).

The r.m.s. represents the ratio between the systematic error and the statistical error $\sigma_{sys}/\sigma_{stat}$. The contribution to the systematic error from this estimator has been evaluated to be 15% of the statistical error.

5.4.6 Estimate of the overall systematic errors

Table 5.11 and 5.12 summarize all the contributions to the systematic errors. The arithmetic mean value of the three contributions from acceptance variation, left/right and top/bottom, has been added in quadrature to the contribution from the different asymmetries estimator. As can be seen, the systematic error is small, always smaller than the smallest statistical error.

Table 5.11: Overall point to point systematic error in units of statistical one for the two hadron asymmetry.

test	h^+h^-
estimator used for extraction of asymmetries	0.15
acceptance variations from false asymmetries	0.71
spectrometer regions:t/b	0.73
spectrometer regions:l/r	0.81
period compatibility	0
overall	0.76

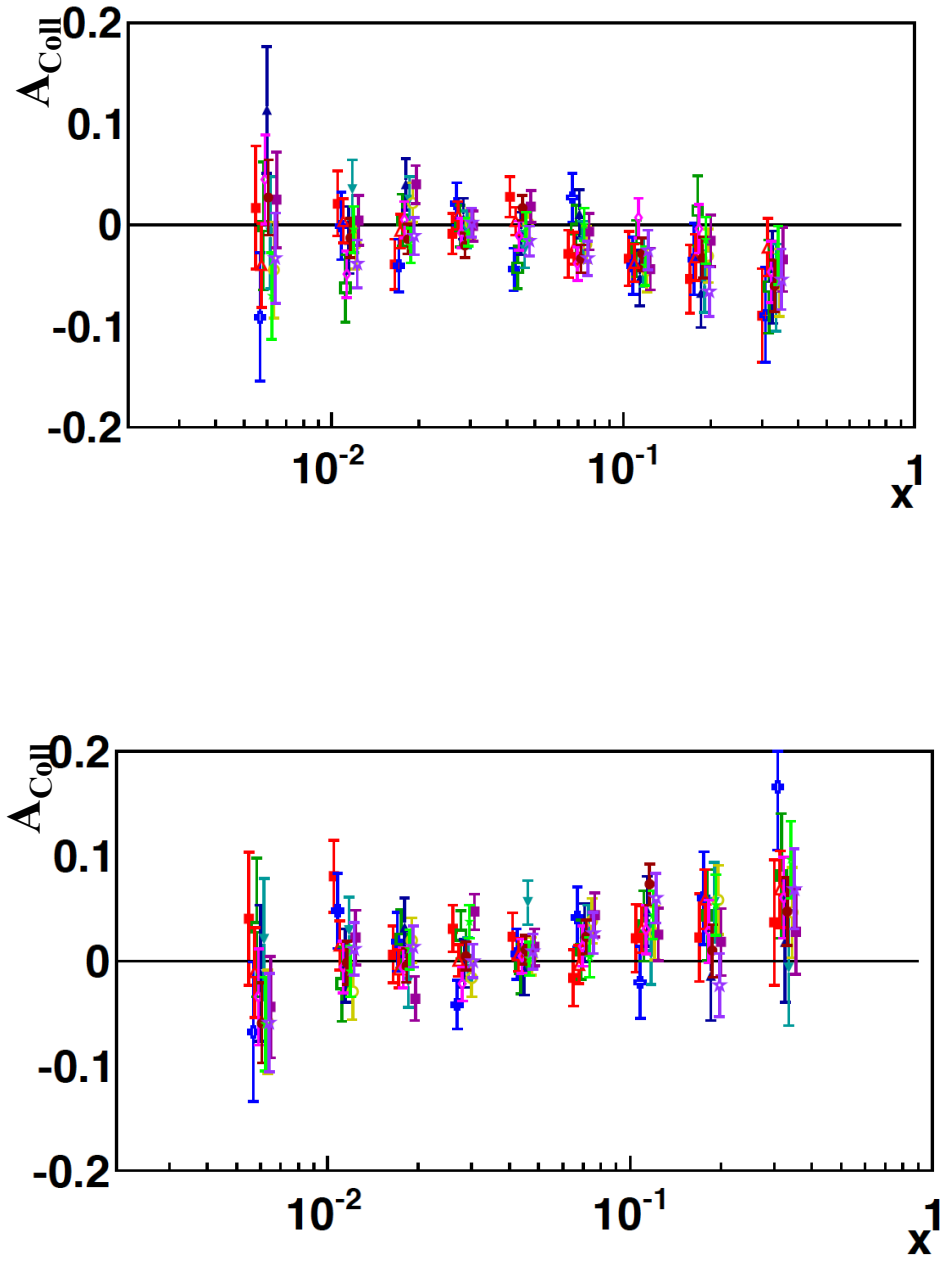

Figure 5.19: Collins asymmetries as a function of x for positive (top) and negative (bottom) hadrons. The different set of data points correspond to the 12 data taking periods of 2010 run.

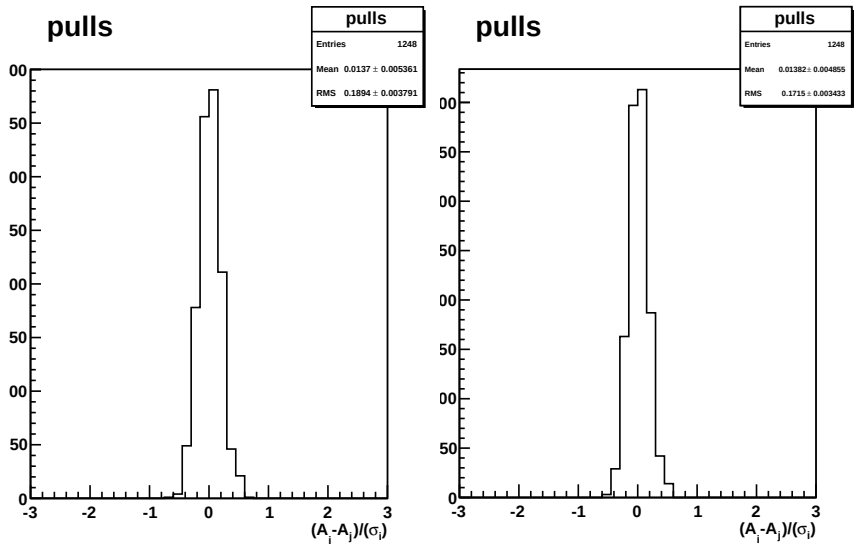

Figure 5.20: Δ_{ij} obtained for the asymmetries extracted with the UL and the QR (left), UL and DR (right).

Table 5.12: Overall point to point systematic error in units of statistical one for the Collins asymmetry.

test	Coll h+	Coll h-
estimator for extraction of asymmetries	0.15	0.15
acceptance variations from false asymmetries	0.45	0.51
spectrometer segments:t/b	0.53	0.50
spectrometer segments:l/r	0.45	0.60
period compatibility	0	0
overall	0.52	0.56

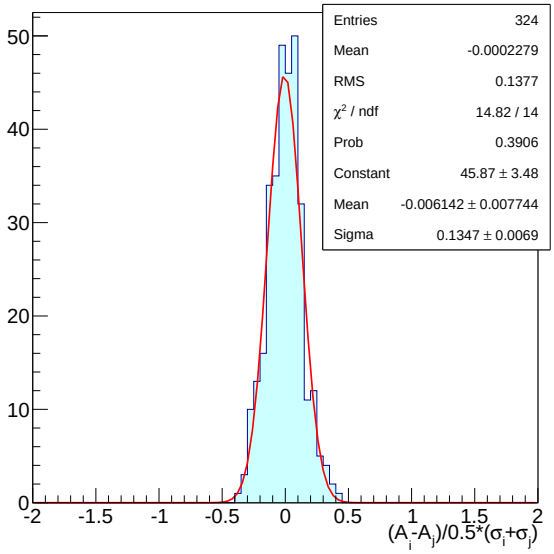

Figure 5.21: Δ_{ij} obtained for the two-hadron asymmetries extracted with the UL and the QR method.

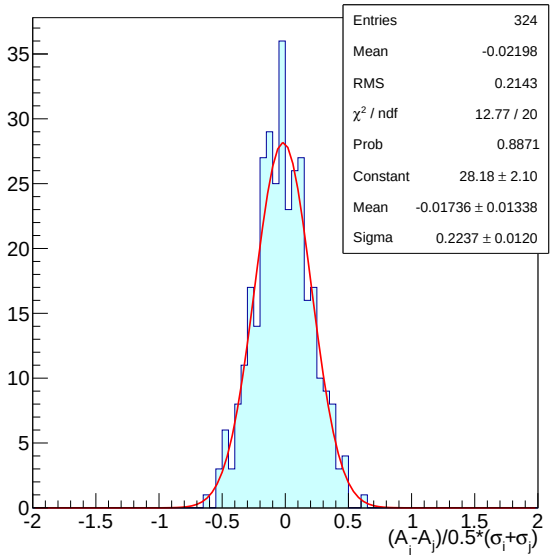

Figure 5.22: Δ_{ij} obtained for the two-hadron asymmetries extracted with the UL and the DR method.

Chapter 6

Results from 2010 data

In the following the results obtained at COMPASS from the data collected in 2010 with the transversely polarized proton target will be presented. All the measured asymmetries shown here are obtained with the methods described in sect. 5.3, and have been corrected for the target polarization and the spin transfer parameter, namely:

$$A_{phys} = \frac{A_{raw}}{f S_T D_{NN}}. \tag{6.1}$$

The spin transfer parameter D_{NN} is measured according to the formula given in eq. 3.8; for the target polarization S_T the measured values given in table 6.1 has been used. The dilution factor f is calculated as function of x; as for the previous measurements we assume that it is constant in z and P_{hT}.

The new results for the Collins and the Sivers asymmetries are presented in sec. 6.1 and sec. 6.2. The results for the two hadron asymmetries are described in sec. 6.3, where they are also compared with previous measurements and model calculations. In the last part of sec. 6.3 further studies on the two hadron asymmetry are described. Sec. 6.4 is dedicated to the measurement of the asymmetries for identified hadrons. Finally in sec. 6.5 the first extraction of the $u-$ and $d-$quark transversity PDFs is presented.

The results for not identified hadrons have already been presented at international conferences (Transversity 2011 [58, 81] and Dubna-Spin 2011 [82]) and will be published soon. The material in the last part of sec. 6.3, sec.6.4 and sec.6.5 is completely new.

6.1 Collins asymmetry

The values of the D_{NN} factor used in the evaluation of the Collins asymmetries as function of x are shown in fig. 6.1, for positive and negative hadrons respectively.

The final asymmetries [58] as a function of x, z, and the transverse momentum of the hadron P_{hT}, are shown in fig. 6.2 for positive (black points) and negative (red points) hadrons. The bars are the statistical errors and the bands give the systematic uncertainties.

The new results confirm with much better statistics the published results from the 2007 proton data [57]. The asymmetries show a strong dependence on x both for

Table 6.1: Measured values of the target polarization for each sub-period.

Period	Sub-period	Cell 1	Cell 2	Cell 3
1	1^{st}	-0.81	+0.81	-0.82
	2^{nd}	+0.81	-0.81	+0.82
2	1^{st}	+0.79	-0.82	+0.82
	2^{nd}	-0.77	+0.79	-0.78
3	1^{st}	-0.80	+0.77	-0.80
	2^{nd}	+0.78	-0.80	+0.80
4	1^{st}	+0.77	-0.78	+0.80
	2^{nd}	-0.72	+0.77	-0.75
5	1^{st}	+0.80	-0.84	+0.83
	2^{nd}	-0.78	+0.80	-0.80
6	1^{st}	-0.79	+0.80	-0.79
	2^{nd}	+0.77	-0.79	+0.78
7	1^{st}	+0.79	-0.81	+0.81
	2^{nd}	-0.76	+0.79	-0.78
8	1^{st}	-0.83	+0.80	-0.80
	2^{nd}	+0.82	-0.83	+0.83
9	1^{st}	+0.80	-0.78	+0.78
	2^{nd}	-0.78	+0.80	-0.79
10	1^{st}	-0.78	+0.76	-0.78
	2^{nd}	+0.75	-0.78	+0.77
11	1^{st}	-0.83	+0.79	-0.81
	2^{nd}	+0.82	-0.83	+0.84
12	1^{st}	+0.79	-0.76	+0.78
	2^{nd}	-0.77	+0.79	-0.78

positive and negative hadrons: in the low-x region the values are compatible with zero, while in the valence region they increase up to about 5%, and have opposite sign for positive and negative hadrons.

The new Collins asymmetries are compared with the previous results from 2007 proton data in fig. 6.3 for positive (top) and negative (bottom) hadrons. As can be seen there is a very good agreement within the statistical errors.

To compare our results with the results of the HERMES collaboration, the Collins asymmetry has also been evaluated for $x > 0.032$. The results are shown as full points in fig. 6.4 as function of x, z and P_{hT}. As can be seen, there is a clear, although weak, linear dependence of the asymmetry both on z and on P_{hT}. The open point in fig. 6.4 are the Hermes results (corrected for the D_{NN} factor and changed in sign because of the different definition of the Collins angle) from [49]. The agreement is very good and this is a very important result, given the difference in the value of $\langle Q^2 \rangle$ between the HERMES and COMPASS data.

Finally the Collins asymmetries from the 2010 proton data are compared with the theoretical predictions obtained by Anselmino et al. [53] in fig. 6.5 for positive hadrons (top) and negative hadrons (bottom). The curves have been obtained from the transversity PDFs and the Collins FF extracted from the fit of the HERMES proton, COMPASS deuteron and the Belle data. The agreement with the COMPASS proton data gives more strength to the current interpretation of the SIDIS results.

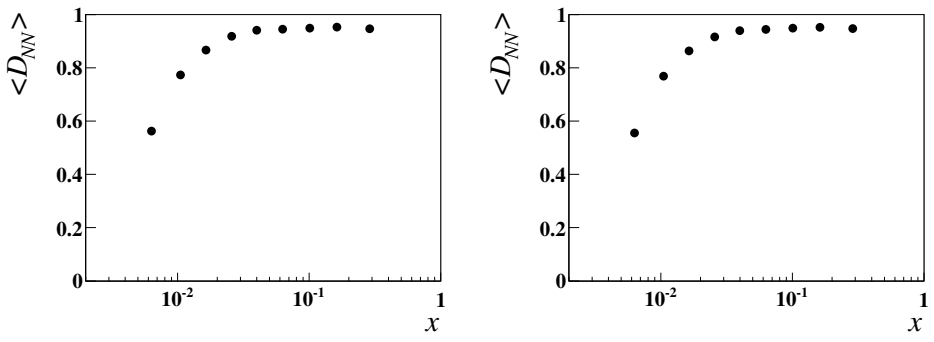

Figure 6.1: D_{NN} factor used in the evaluation of the Collins physical asymmetries as function of x for positive (left) and negative (right) hadrons.

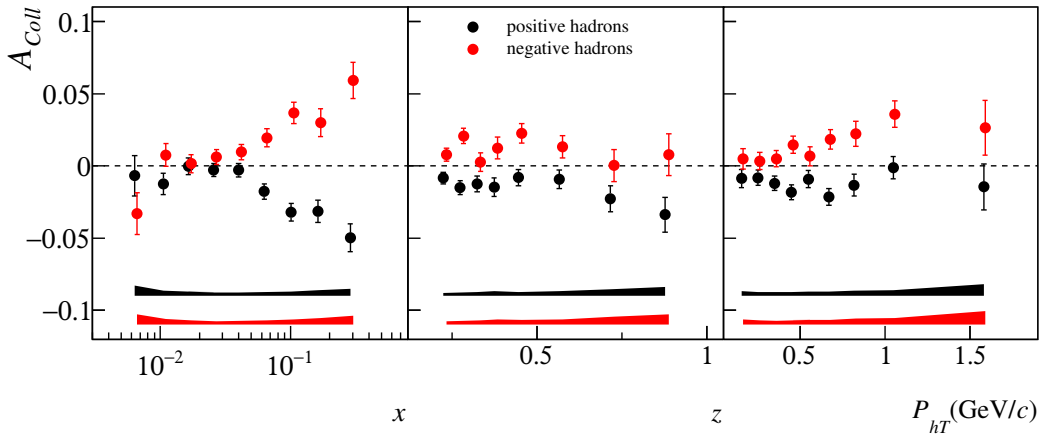

Figure 6.2: The Collins asymmetries from 2010 proton data for positive and negative charge hadrons as function of x,z and P_{hT}.The error bars are the statistical errors and the bands show the systematic errors.

6.2 Sivers asymmetry

For completeness we show the Sivers asymmetries measured from 2010 proton data [58] in fig. 6.6 as function of x, z and P_{hT}.

The Sivers asymmetry as function of x for negative hadrons is compatible with zero while the signal for positive hadrons is definitively different from zero (up to 5%) and the asymmetry is different from zero also at small x values, in the region not measured at HERMES, and where the Collins asymmetry is compatible with zero. The new results are in agreement with the measurement from the 2007 data [57] but the statistical errors are smaller by more than a factor of 2 and the systematic uncertainties are much smaller. In particular the results from the 2010 data are not affected by the 0.01 scale uncertainty of the results of [57]. The new results clearly confirm that the Sivers asymmetry is smaller at the COMPASS energy as compared to the asymmetry measured by HERMES, a fact that seems to be understandable in terms of TMDs evolution [83]. More results on the dependence of the Collins

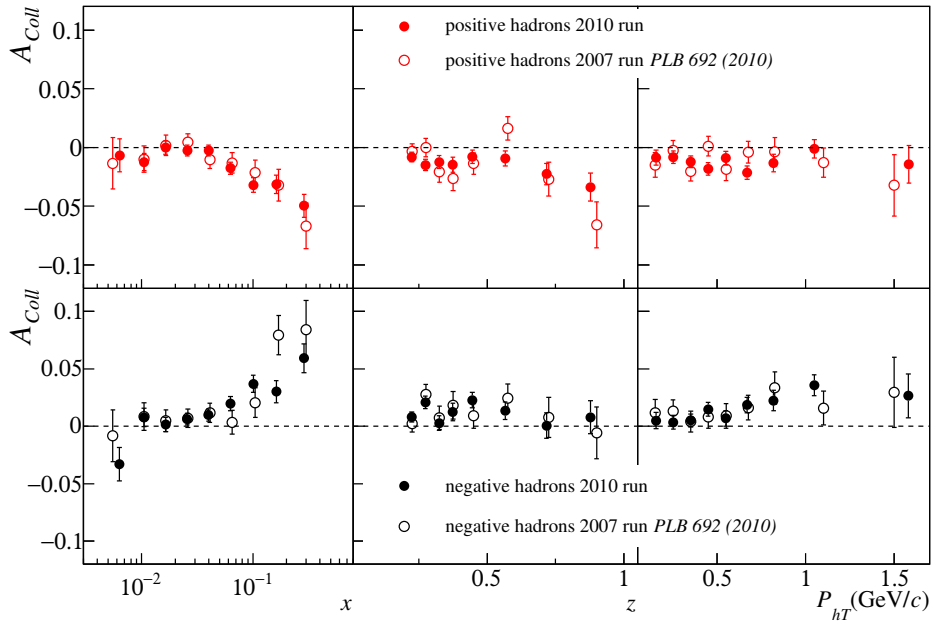

Figure 6.3: The Collins asymmetries from the 2010 proton data (full points)[58] compared with the results from the 2007 proton data (open points)[57] for positive (top) hadrons and negative (bottom) charged hadrons. The error bars are the statistical errors.

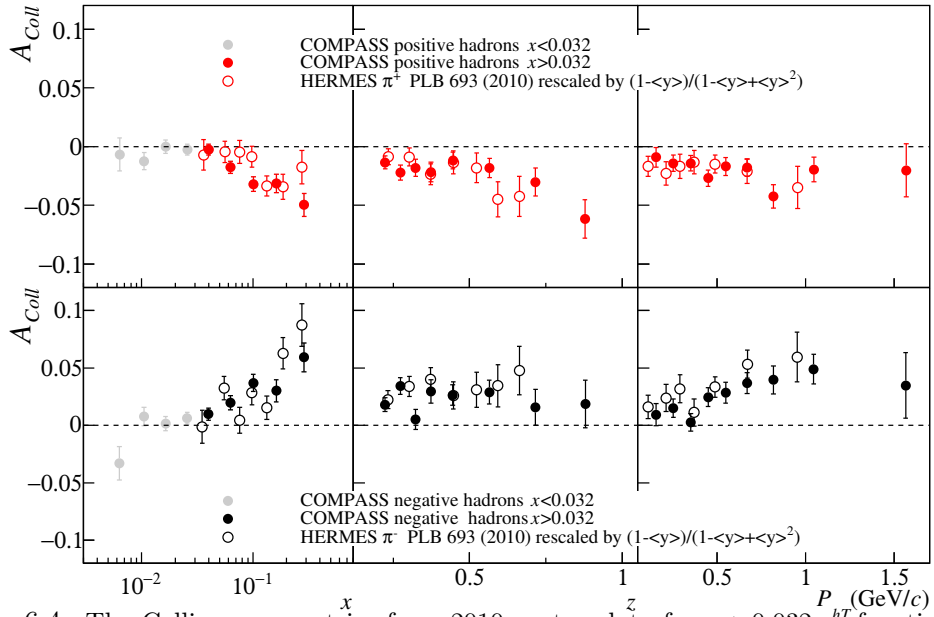

Figure 6.4: The Collins asymmetries from 2010 proton data for x >0.032 as function of x, z and P_{hT} for positive (top) and negative (bottom) hadrons. The open points are the asymmetries measured at HERMES for π^+ (top) and π^- (bottom). The error bars are the statistical errors.

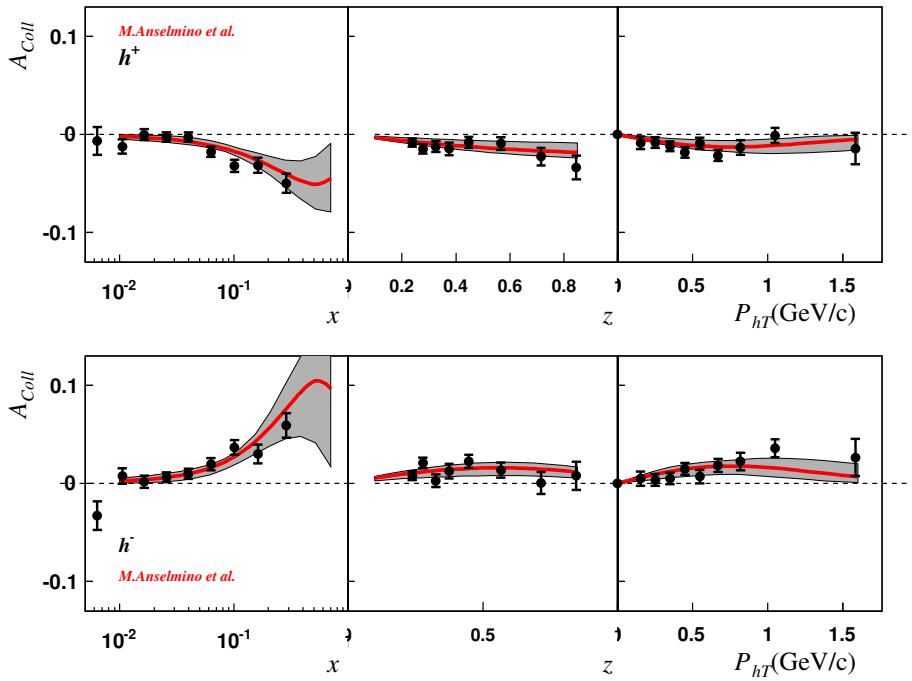

Figure 6.5: The Collins asymmetries from 2010 proton data for positive hadrons (top) and negative hadrons (bottom) compared with the theoretical predictions obtained by Anselmino et al. [53]. The error bars are the statistical errors.

and Sivers asymmetries on the kinematical variables can be found in [58]. The COMPASS measurement is very important in establishing that the Sivers function indeed is different from zero, and opens the way to a possible test of the pseudo-universality property of the T-odd PDFs, a fundamental prediction of the modern treatment in QCD of the SIDIS processes.

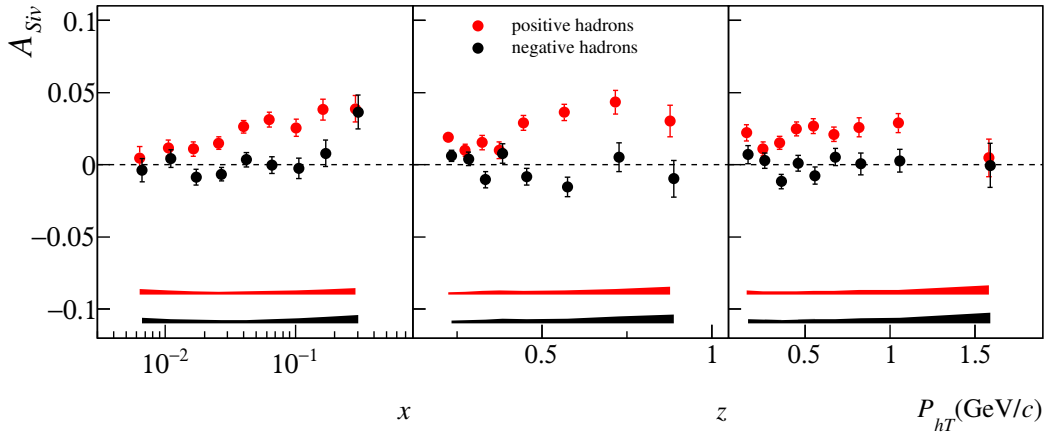

Figure 6.6: The Sivers asymmetries from 2010 proton data for charged hadrons as function of x, z and P_{hT}.The error bars are the statistical errors and the bands show the systematic errors.

6.3 Two-hadron asymmetry

The two-hadron asymmetries have been extracted binning alternatively the data in x, z and the invariant mass of the hadron pairs M_{inv} and the results for all oppositely charged hadron pairs have already been show at Transversity 2011 [81] and Dubna DSPIN2011 [82]. As for the Collins asymmetries, the two-hadron physical asymmetries A_{2h} are obtained from the raw asymmetries using eq. 6.1. The depolarization factor as function of x is shown in fig. 6.7. The values are very much the same as those used for the Collins asymmetry, the differences being due to the slightly different $\langle y \rangle$.

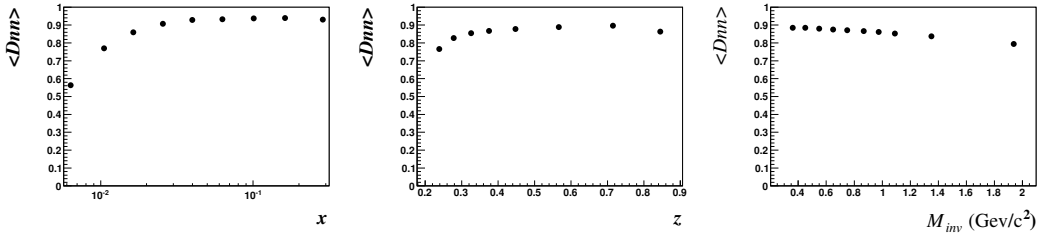

Figure 6.7: D_{NN} factor used in the evaluation of the two-hadron asymmetries as function of x, z and M_{inv}.

The Q^2, x, and W distributions for the final sample have already been given in fig. 5.2. The invariant mass distribution for selected hadron pairs is shown in fig. 6.8. The two peaks which correspond to K^0 around 0.5 GeV/c^2 and ρ^0 around 0.77 GeV/c^2 are evident.

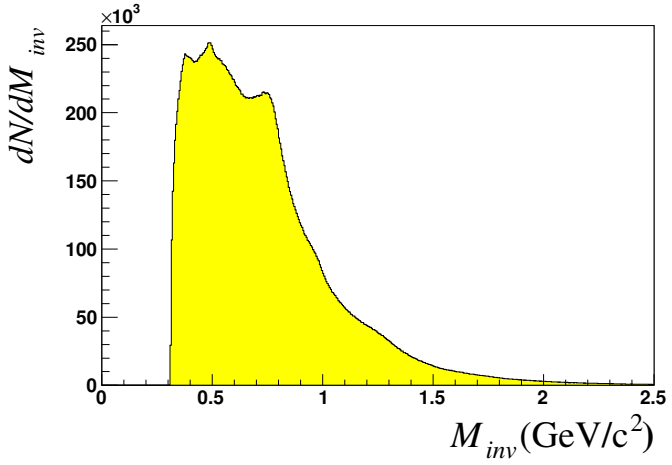

Figure 6.8: Invariant mass distribution of the 2010 final hadron pairs.

The distributions of $z = z_1 + z_2$ and $\xi = z_1 - z_2$ are given in fig. 6.9 left and right, respectively, while fig. 6.10 shows the $z_1 - z_2$ correlation and the z_1 distribution.

Fig. 6.11 shows the $P_{1T} - P_{2T}$ correlation (left) and the P_{1T} distribution (right).

The distributions of sinθ and cosθ defined in sec. 3.2 are shown in fig. 6.12.

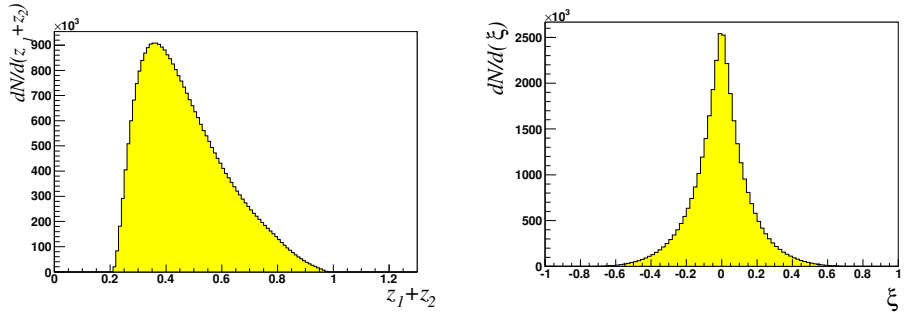

Figure 6.9: The distribution of $z = z_1 + z_2$ and $\xi = z_1 - z_2$ from the 2010 final hadron pairs.

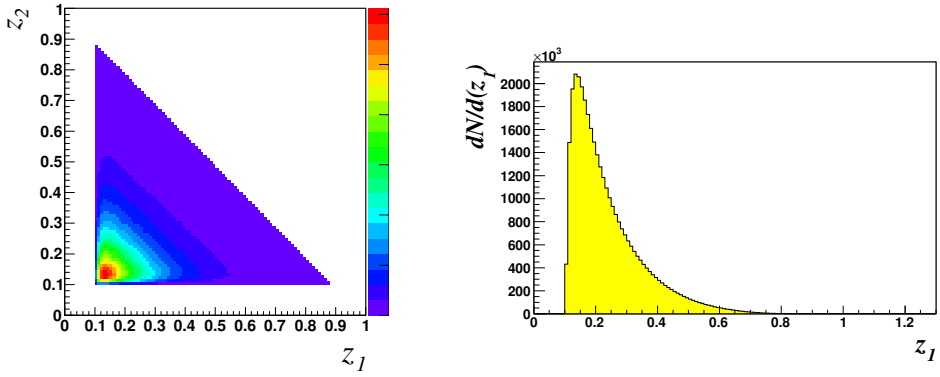

Figure 6.10: $z_1 - z_2$ correlation (left) and z_1 distribution from the 2010 final hadron pairs.

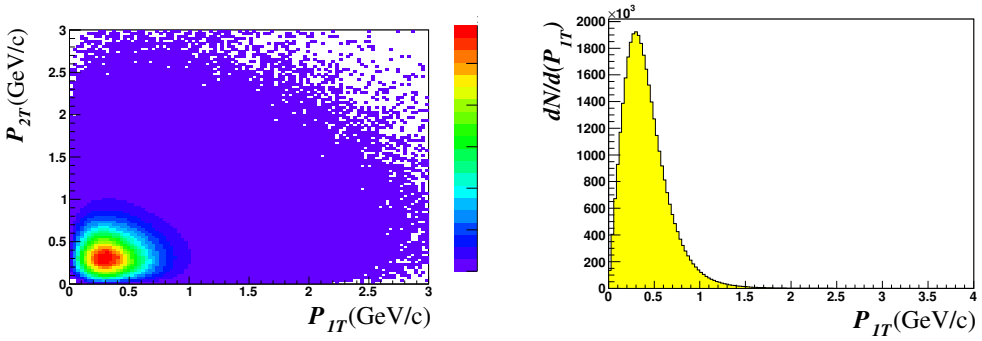

Figure 6.11: $P_{1T} - P_{2T}$ correlation (left) and P_{1T} distribution from the 2010 final hadron pairs.

The mean values of Q^2 in the different x,z and M_{inv} bins are given in fig. 6.13, the mean values of z and M_{inv} in the x bins are given in fig. 6.14, the mean values of x and M_{inv} in the z bins are shown in fig. 6.15, and the mean values of x and z in the M_{inv} bins are shown in fig. 6.16.

The two-hadron asymmetry as function of x, z and M_{inv} is shown in fig. 6.17. It is similar to the dependence measured at Belle. A large asymmetry up to ∼5% in the

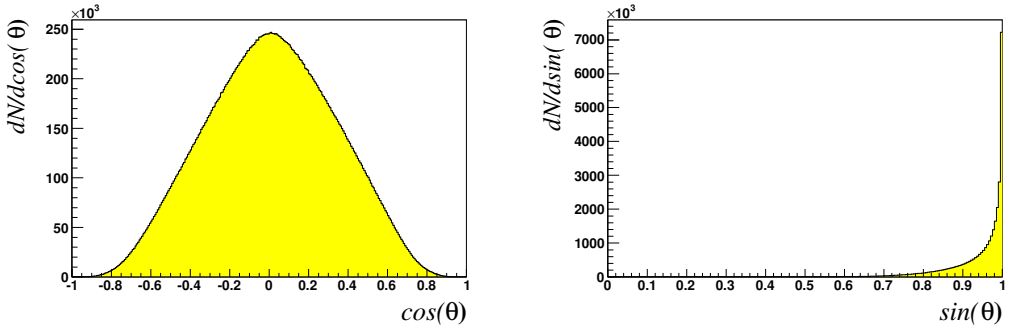

Figure 6.12: cosθ (left) and sinθ (right) distributions from the 2010 final hadron pairs.

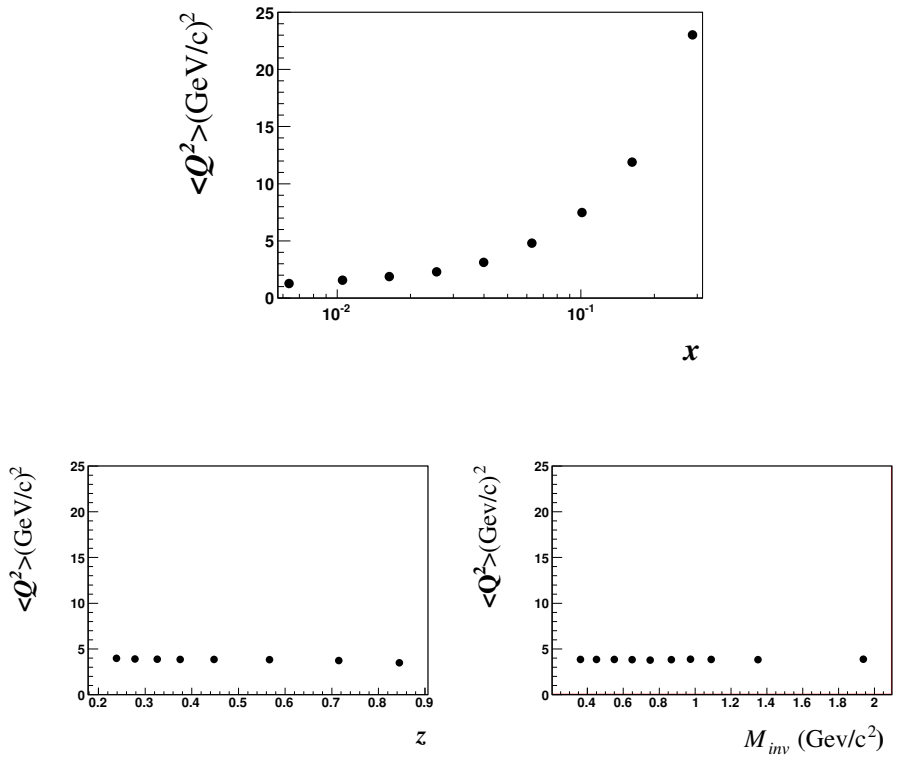

Figure 6.13: mean values of Q^2 in the different x,z and M_{inv} bins.

valence x-region is measured, as large as the Collins asymmetry. The z dependence is smooth while there is a clear and interesting dependence on the invariant mass which is even more clear when the $x > 0.032$ region is selected, as shown in fig. 6.18. The binning used for the $x > 0.032$ data sample, is given in appendix B.

6.3.1 Comparison with previous results and model calculations

The results from the 2010 COMPASS proton data are compared with the results obtained from 2007 COMPASS proton data in fig. 6.19 and the overall agreement

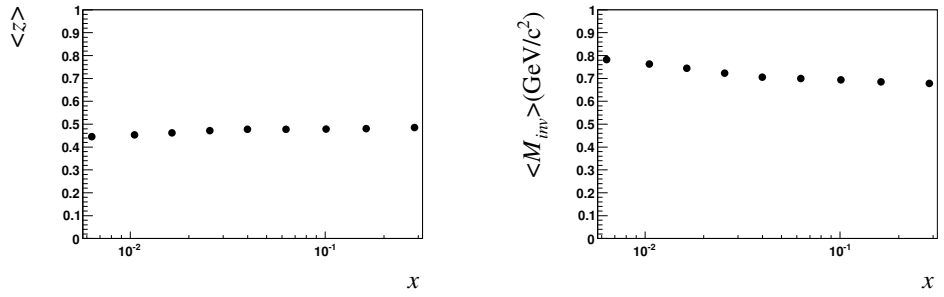

Figure 6.14: mean values of z and M_{inv} in the x bins.

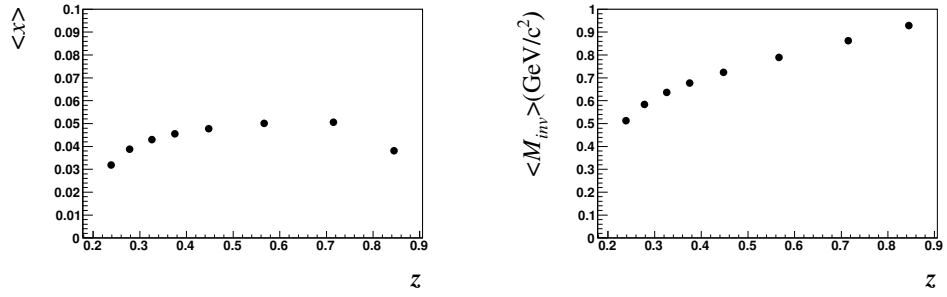

Figure 6.15: mean values of x and M_{inv} in the z bins.

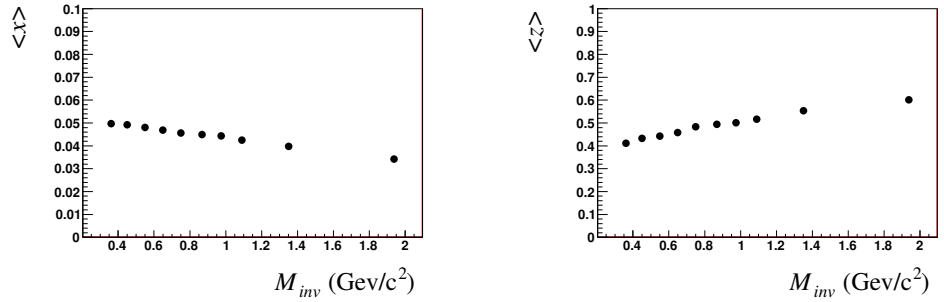

Figure 6.16: mean values of x and z in the M_{inv} bins.

is good. The statistical errors of the 2010 results is almost a factor of 2 smaller than the statistical errors of the 2007 results as shown in fig. 6.20 in which the ratio between the 2010 statistical error and the 2007 statistical error is shown. This will allow for further investigation on the dependence of the asymmetry on the different kinematical variables. The improvement of statistics has also made clearer the M_{inv} dependence. The comparison is shown in fig. 6.19.

The two-hadron asymmetries for proton have been first measured by HERMES [60]. Since the HERMES results given in [60] contain also the D_{NN} factor the comparison between the HERMES and COMPASS results has been performed rescaling the HERMES results by the D_{NN}. Further the sign of the HERMES data has been

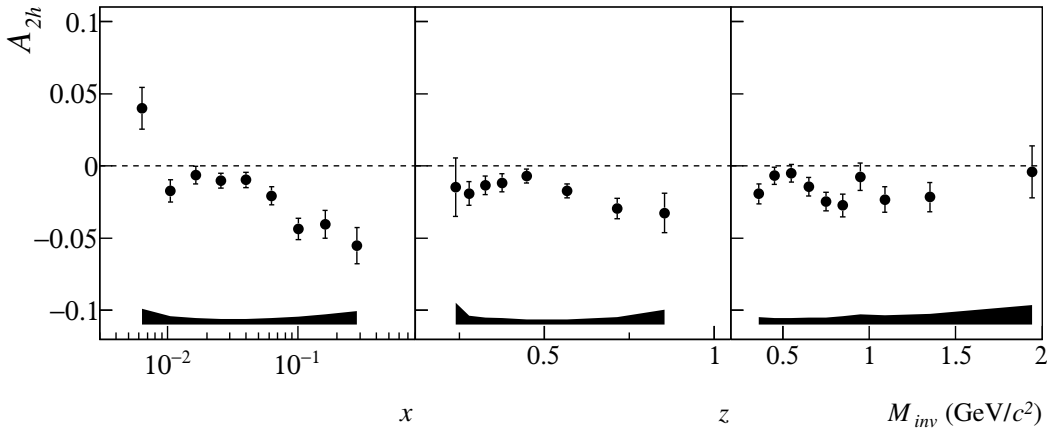

Figure 6.17: Two-hadron asymmetry from 2010 proton data for charged particles as function of x,z and M_{inv}. The error bars are the statistical errors and the bands show the systematic errors.

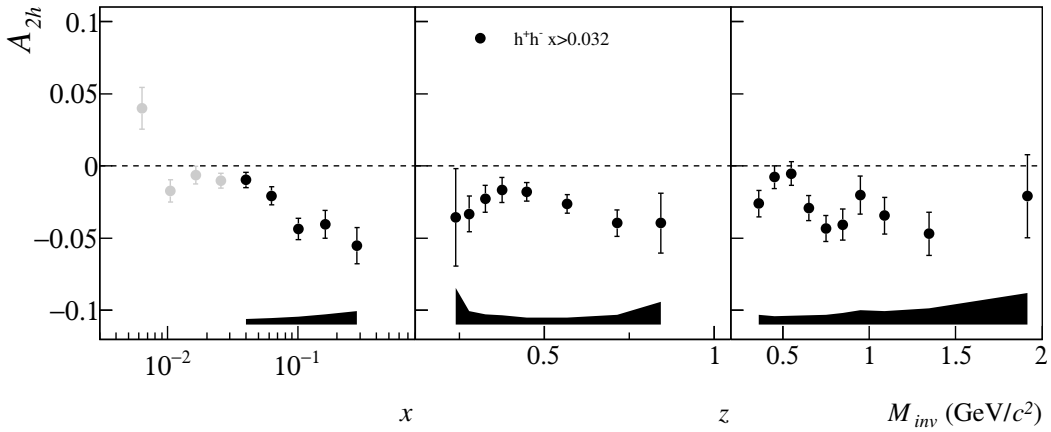

Figure 6.18: Two-hadron asymmetry from the 2010 proton data for charged particles and for $x > 0.032$ as a function of x,z and M_{inv}. The error bars are the statistical errors and the bands show the systematic errors.

changed according to the COMPASS definition of the azimuthal angle[1]. The new COMPASS results already shown in fig. 6.18 are compared with the HERMES data in fig. 6.21. The agreement is good. The statistical precision and the kinematical range of the COMPASS measurements are clearly larger.

The two-hadron asymmetries have been compared with the theoretical predictions given in [43]. The model used in this analysis is the "spectator model" [84] and the parameters of the event generator have been tuned for HERMES kinematics and to reproduce the HERMES results [60]. The results have been obtained using

[1]The COMPASS definition of the ϕ_{RS} angle differs from the HERMES definition for the addition of a π which produce an inversion of the sign.

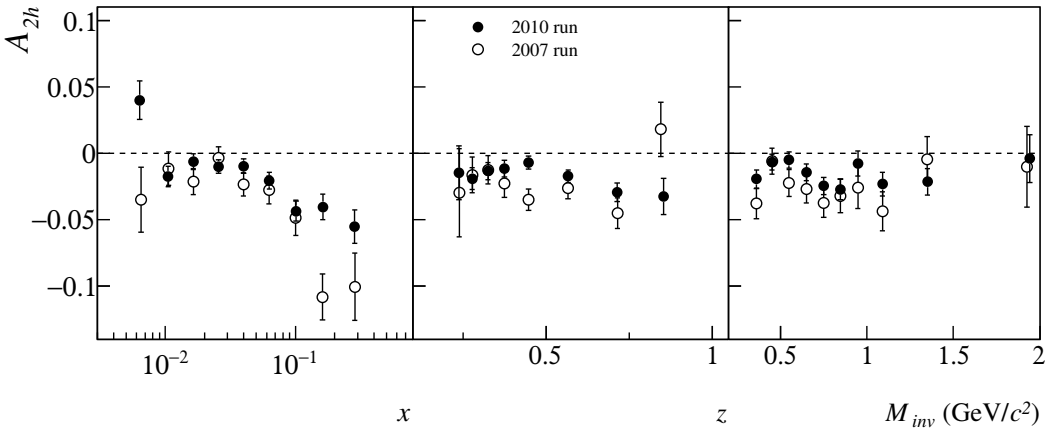

Figure 6.19: Two-hadron asymmetries from 2010 proton data (full points) as function of x,z and M_{inv} compared with the results obtained from 2007 COMPASS proton data (open points). The error bars are the statistical errors.

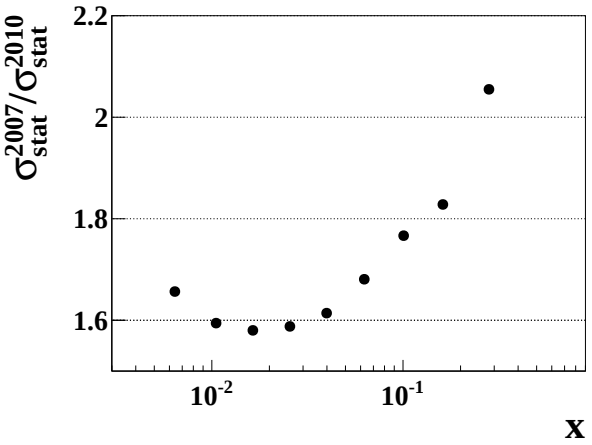

Figure 6.20: Ratio between the statistical errors of the results obtained from the 2007 proton data and from the 2010 COMPASS proton data as function of x .

eq. 16 of ref. [43] without the D_{NN} factor and using the parametrization of ref. [53] for the transversity PDF [86]. The sign of the predictions for the COMPASS has been inverted to take into account the different definition of the ϕ_{RS} angle with respect to that used by HERMES. The model predictions are compared with the new COMPASS results for the two-hadron asymmetries in fig. 6.22. The x and z dependences agree with the data while the dependence on the invariant mass of the measurements is not reproduced very well.

The situation is somewhat similar for the theoretical predictions given in [85]. The model used in this prediction for the fragmentation function is exactly the same used in [43] while the two analysis differ because in [85] is used a model to describe the transversity PDF. The comparison between our results and these predictions is

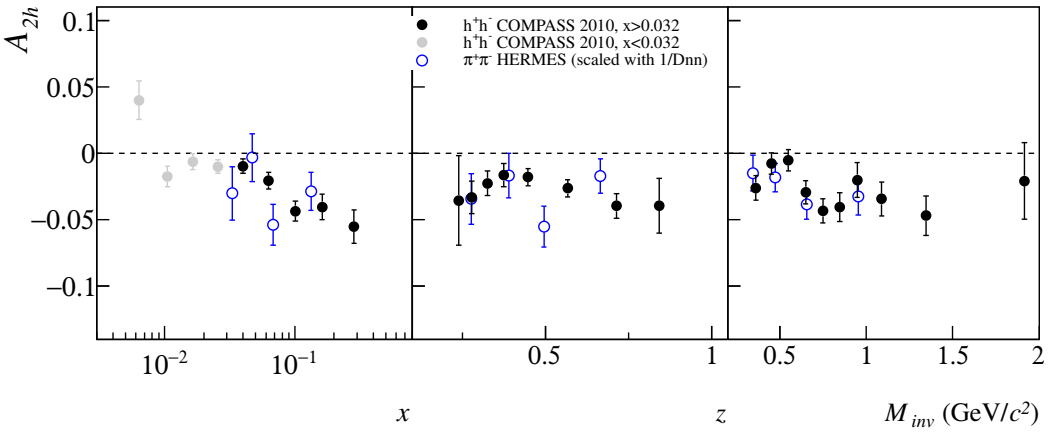

Figure 6.21: Two-hadron asymmetries from 2010 proton data as a function of x,z and M_{inv} compared with the HERMES results [60]. The error bars are the statistical errors.

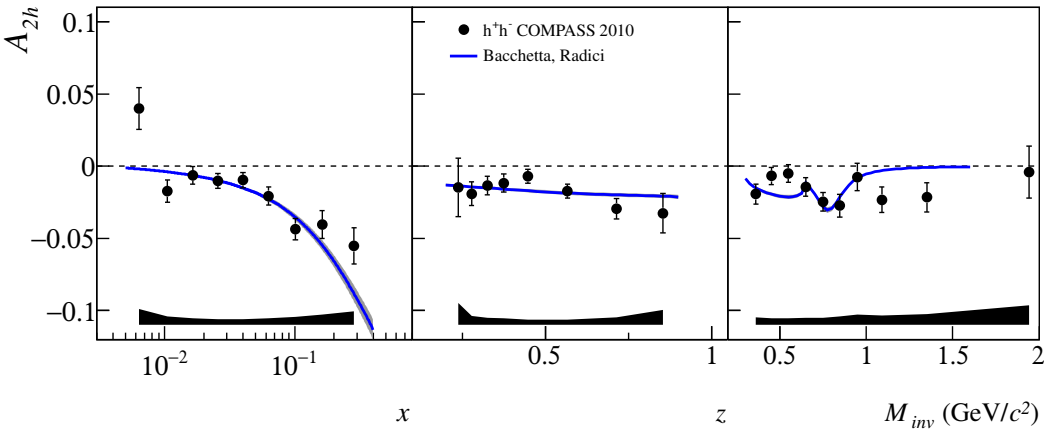

Figure 6.22: Two-hadron asymmetries from 2010 proton data for charged particles as a function of x,z and M_{inv} compared with the theoretical predictions of [43].The error bars are the statistical errors and the bands show the systematic errors.

shown in fig. 6.23. A part from a scale factor, there is a clear disagreement between the data and the predictions as function of the invariant mass.

6.3.2 Further studies of kinematical dependence

In addition to the released results, several new tests have been performed for this thesis and are described in the following. The two hadron asymmetries have been evaluated also selecting different kinematical ranges in y, z and M_{inv} to have a first look to the kinematical dependencies of the signal.

The y range has been divided in two intervals $0.1 < y < 0.2$ and $0.2 < y < 0.9$, to investigate if in the case of the two hadron asymmetries there is some hint for a y (or W) dependence already noticed in particular for the Sivers asymmetry [57, 58].

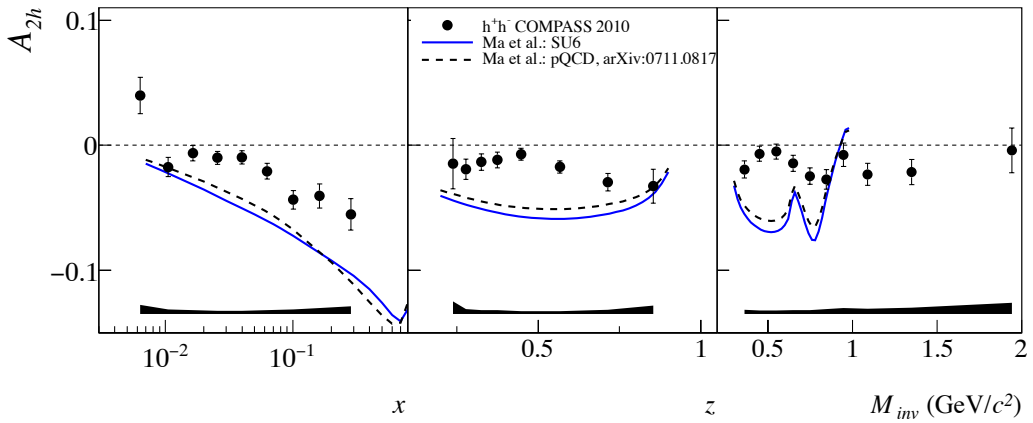

Figure 6.23: Two-hadron asymmetries from 2010 proton data for charged particles as a function of x,z and M_{inv} compared with the theoretical predictions of [85]. The error bars are the statistical errors and the bands show the systematic errors.

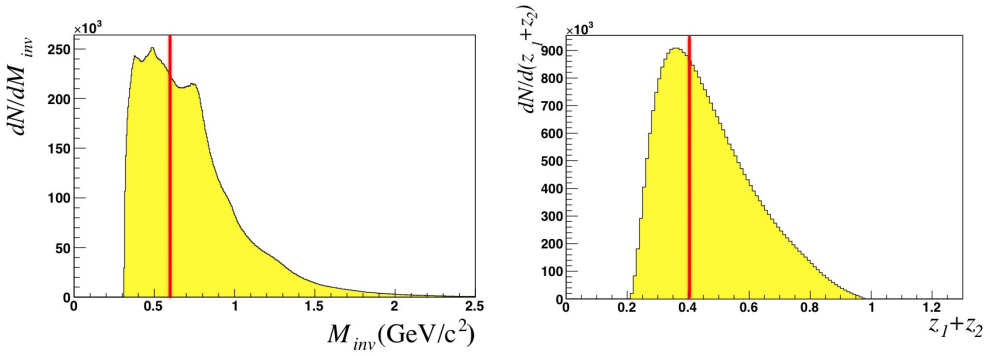

Figure 6.24: Kinematical ranges in z and M_{inv} of the 2010 final hadron pairs.

The z range has also been divided in two intervals ($0.2 < z < 0.4$) and ($z > 0.4$) and two intervals in M_{inv} range, $M_{inv} < 0.6$ GeV/c^2 and $M_{inv} > 0.6$ GeV/c^2, have been considered. The two z and M_{inv} bins are shown in fig. 6.24 for the z and M_{inv} distributions and the asymmetries as function of z and M_{inv} are shown in fig. 6.25. The bins have been chosen in order to have almost the same statistics and to separate two possibly different kinematical regions.

The asymmetries obtained in the two different y ranges are shown in fig.6.26 as function of x, and in fig. 6.27 as function of z and M_{inv}. There is no clear evidence of a dependence on the y. On the other hand, when looking at the asymmetries as function of z, some systematic differences can be present (fig. 6.27), a point which will require a deeper investigation in the future.

The asymmetries obtained in the two different z ranges are shown in fig. 6.28 as function of x and in fig. 6.29 as function of M_{inv}. No dependence on z can be seen except, may be, at $M_{inv} \sim 0.85$ GeV/c^2.

In figs. 6.30 and 6.31 the asymmetries obtained in the two different M_{inv} bins

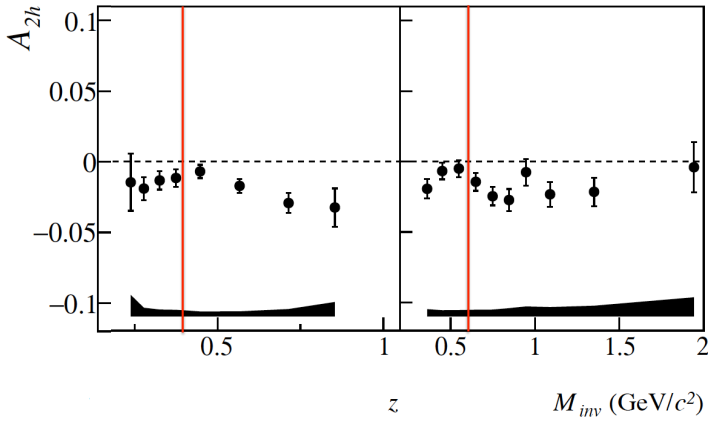

Figure 6.25: Kinematical ranges in z and M_{inv} of the 2010 final hadron pairs.

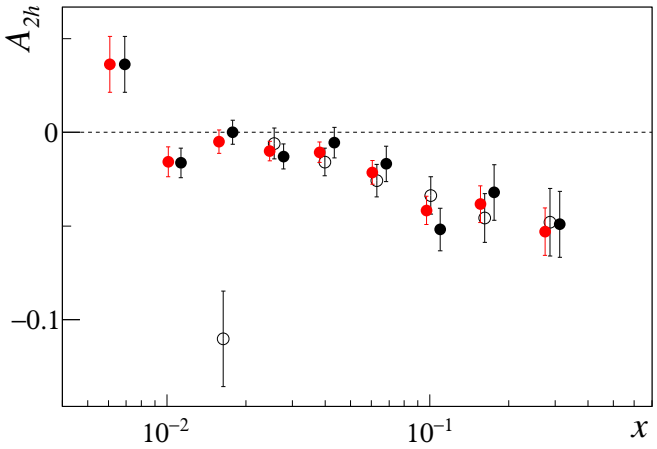

Figure 6.26: Two-hadron asymmetries as function of x for $0.1 < y < 0.2$ (open points), $0.2 < y < 0.9$ (black points) and full y range (red points).

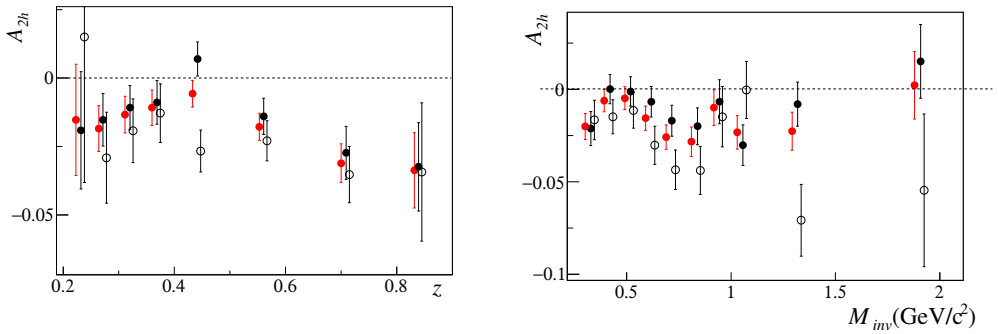

Figure 6.27: Two-hadron asymmetries as function of z (left) and M_{inv} (right) for $0.1 < y < 0.2$ (open points), $0.2 < y < 0.9$ (black points) and full y range (red points).

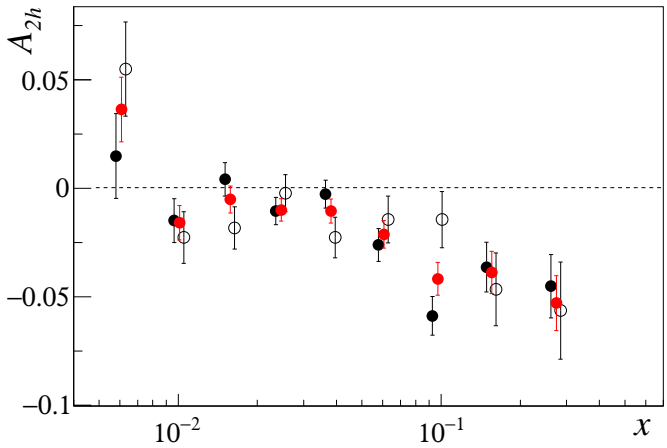

Figure 6.28: Two-hadron asymmetries as function of x for $0.2 < z < 0.4$ (open points), $z > 0.4$ (black points) and full z range (red points).

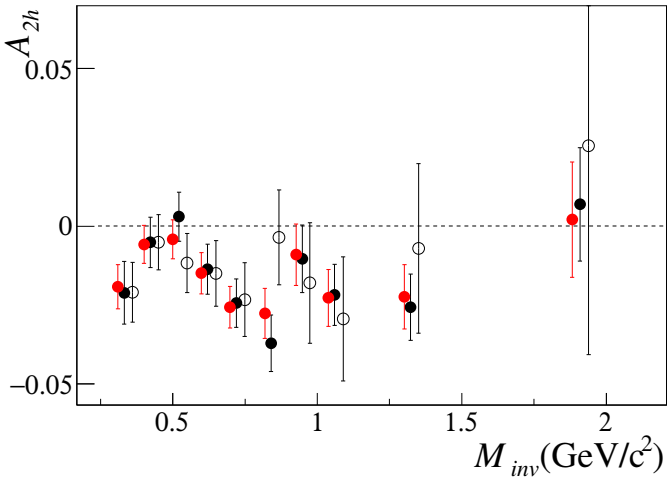

Figure 6.29: Two-hadron asymmetries as function of M_{inv} for $0.2 < z < 0.4$ (open points), $z > 0.4$ (black points) and full z range (red points).

are shown as function of x and z, respectively.

The signal in x bins decreases in the $M_{inv} < 0.6$ GeV/c^2 region, while increases in $M_{inv} > 0.6$ GeV/c^2, but the trend is similar. These results underline the strong kinematical dependence of the two-hadron asymmetries on M_{inv} and in particular how the low M_{inv} region gives only a small contribution to the signal.

Other important information obtained from this analysis concern the z kinematical dependence. The small signal present for $M_{inv} < 0.6$ GeV/c^2 seems to be due to the $z > 0.5$ pair only. On the contrary, for $M_{inv} > 0.6$ GeV/c^2 the z dependence of the asymmetry seems to be almost linear, in agreement with the Belle measurement of fig. 3.17.

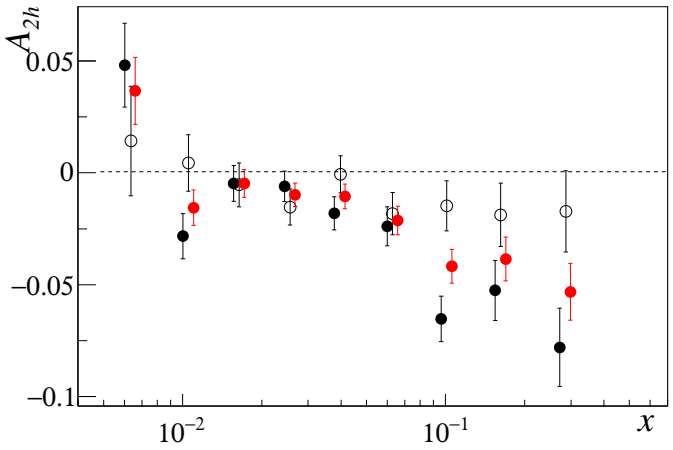

Figure 6.30: Two-hadron asymmetries as function of x for $M_{inv} < 0.6$ GeV/c^2 (open points), $M_{inv} > 0.6$ GeV/c^2 (black points) and full M_{inv} range (red points).

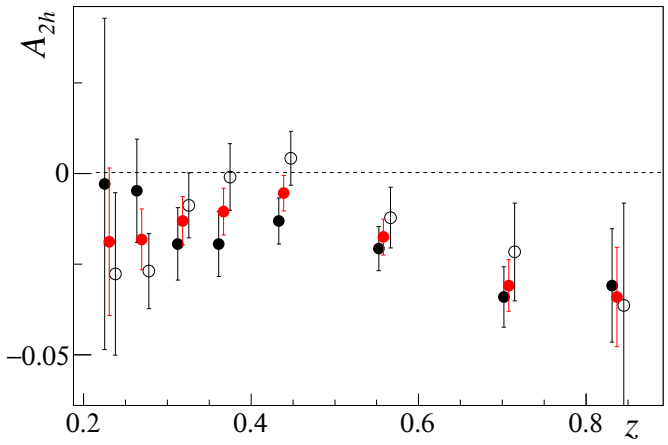

Figure 6.31: Two-hadron asymmetries as function of z for $M_{inv} < 0.6$ GeV/c^2 (open points), $M_{inv} > 0.6$ GeV/c^2 (black points) and full M_{inv} range (red points).

6.3.3 "z-ordered" two hadron-asymmetries

An interesting semi-classical model for the fragmentation of a quark has been proposed by Artru [47] and it has already been introduced in chapter 3. Following this model, the "1st rank" (or "leading") hadron produced in the fragmentation has higher memory of the fragmenting quark. Thus, in the u (d) quark fragmentation the 1st rank hadron should be a π^+ (π^-). To select the 1st rank hadron, and thus access the quark flavour, a possibility is to choose the highest z_i final state hadron[2].

At variance with respect to the pair selection performed until now, the hadron pairs are selected considering only one pair per event, consisting of the leading and

[2]Another possibility, not investigated here and suggested in [47], is to order the final state hadrons with decreasing P_{hT} and choose the sub-leading hadrons as rank 1 hadron.

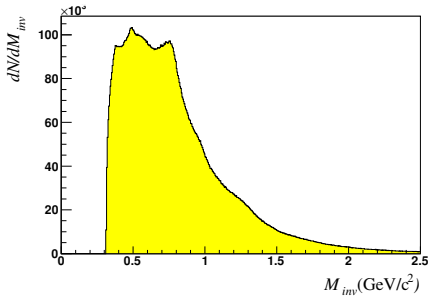

(a) Invariant mass distribution for $h_l^+ h_{sl}^-$ pairs .

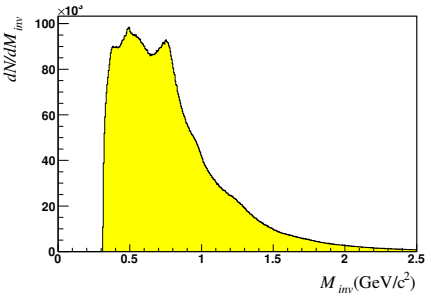

(b) Invariant mass distribution for $h_l^- h_{sl}^+$ pairs .

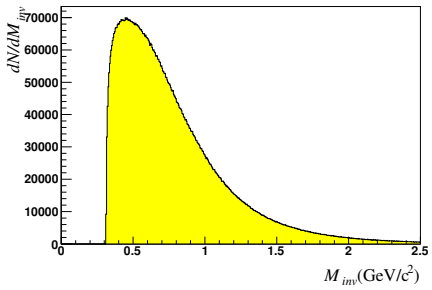

(c) Invariant mass distribution for $h_l^+ h_{sl}^+$ pairs .

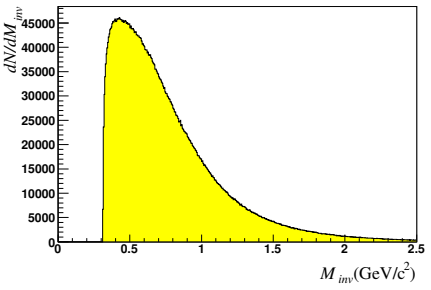

(d) Invariant mass distribution for $h_l^- h_{sl}^-$ pairs .

Figure 6.32: The invariant mass distributions for all possible combinations of leading and sub-lading hadron pairs in the z-ordered analysis.

the sub-leading hadrons, the leading hadron being the hadron with the largest value of z, and the sub-leading hadron the one with the second largest value of z. This pair selection allows to group the hadron pairs according to 4 different combinations with the leading and sub-leading hadrons being either positive or negative. The invariant mass distributions obtained for the different combinations are shown in fig. 6.32. The asymmetries for the different combinations of leading and sub-leading hadrons of opposite charge are shown in figs. 6.33 and 6.34.

As expected in the framework of the Artru model in case of opposite sign u and d quark transversity PDFs, the signal is the same both for $h_l^+ h_{sl}^-$ and for $h_{sl}^+ h_l^-$. In evaluating the asymmetry, the first particle is always the positive one. The size of the asymmetries are almost the same in spite of the somewhat smaller values expected in the $h_{sl}^+ h_l^-$ case. The most remarkable difference is in the dependence on M_{inv}: as can be seen in fig. 6.33, in the $h_l^+ h_{sl}^-$ case almost all the signal seems to come from the region $M_{inv} \sim 0.8$ GeV/c^2, an effect presently we are not able to interpret. For internal cross-check, the weighted averages of the asymmetries for $h_l^+ h_{sl}^-$ and $h_{sl}^+ h_l^-$ has been evaluated. As can be seen in fig. 6.35, these average

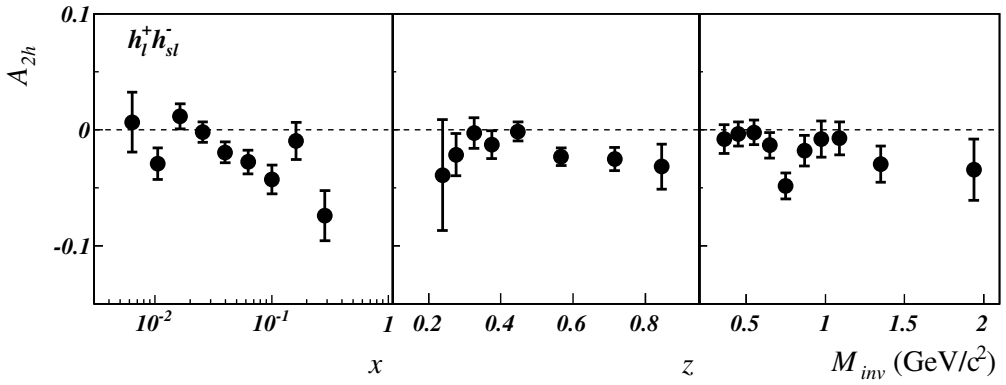

Figure 6.33: Two-hadron asymmetry from 2010 proton data for positive leading hadron and negative sub-leading hadron as function of x,z and M_{inv}. The error bars are the statistical errors.

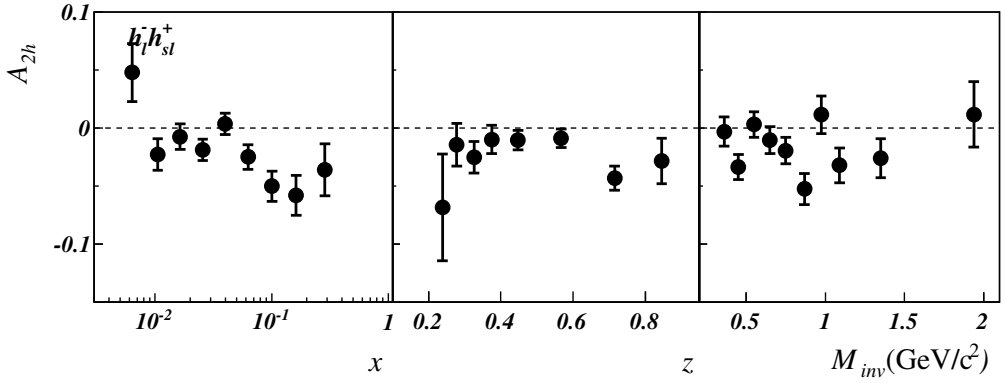

Figure 6.34: Two-hadron asymmetry from 2010 proton data for negative leading hadron and positive sub-leading hadron as function of x,z and M_{inv}. The error bars are the statistical errors.

values are in very good agreement with all the pairs asymmetries, as expected.

Finally, in figs. 6.36 and 6.37 one can see the asymmetries for the pairs with the same electric charge, i.e. $h_l^+ h_{sl}^+$ and $h_l^- h_{sl}^-$. The values are compatible with zero, as expected.

6.4 Asymmetries for charged π and K

The same method described in sec. 5.3 has been used to extract the asymmetries on identified pions and kaons. The particle identification has been performed applying the cuts discussed in sec. 5.1.3 and here summarized:

- $P_{max} = 50$ GeV/c;
- if $\frac{\mathcal{L}_e}{\mathcal{L}_\pi} < 1.8$ the electron can be identified and $\mathcal{L}_e$ is taken into account;
- $\frac{\mathcal{L}_\pi}{\mathcal{L}_{2nd}} > 1.02$;

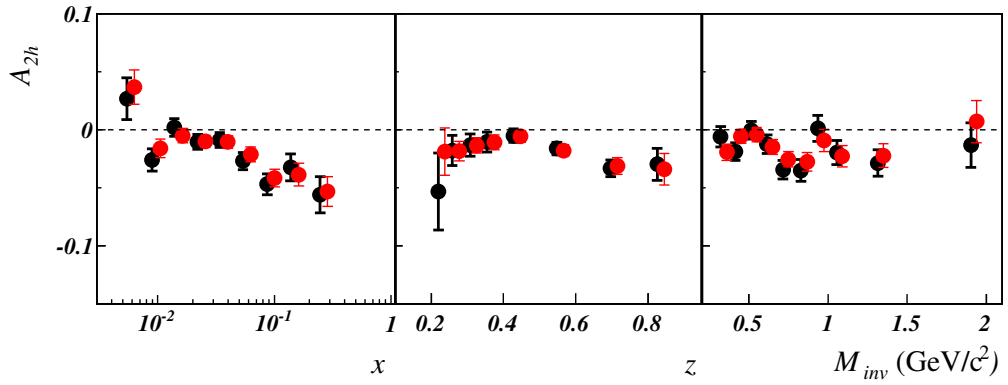

Figure 6.35: Weighted mean between the two-hadron asymmetries obtained for positive leading hadron and negative sub-leading hadron and asymmetries obtained for negative leading hadron and positive sub-leading as function of x,z and M_{inv}. The error bars are the statistical errors.

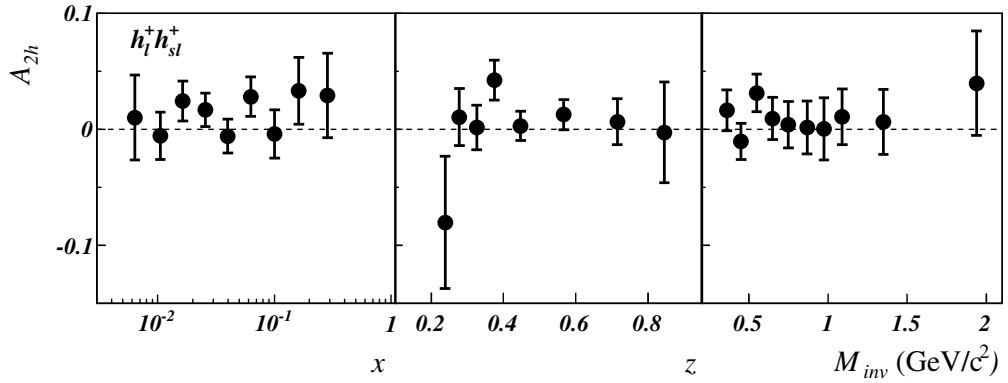

Figure 6.36: Two-hadron asymmetry from 2010 proton data for positive leading hadron and positive sub-leading hadron as function of x,z and M_{inv}. The error bars are the statistical errors.

- $\frac{\mathcal{L}_K}{\mathcal{L}_{2nd}} > 1.08$.

The Collins and Sivers asymmetries have been measured considering separately the positive and negative pions and kaons while in the case of two-hadron asymmetries we have considered all the possible combinations of identified oppositely charged hadrons. Due to the limited statistic of the kaon sample, the binning has been reduced with respect to that used for the unidentified particles and for the pions. The M_{inv} binning for the extraction of two-hadron asymmetries has been changed to take into account the different range of the invariant mass obtained considering the different combinations of pions and kaons. The asymmetries have not been corrected for the misidentification probabilities which are always small (see sec. 5.2.5).

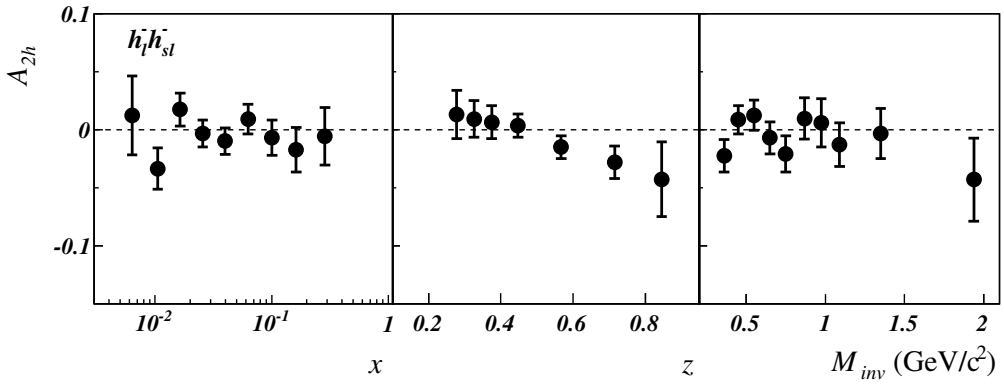

Figure 6.37: Two-hadron asymmetry from 2010 proton data for negative leading hadron and negative sub-leading hadron as function of x,z and M_{inv}. The error bars are the statistical errors.

6.4.1 Collins and Sivers asymmetries

The Collins Asymmetries for positive and negative pions and kaons as function of x, z and P_{hT} are shown in figs. 6.38 and 6.39, respectively.

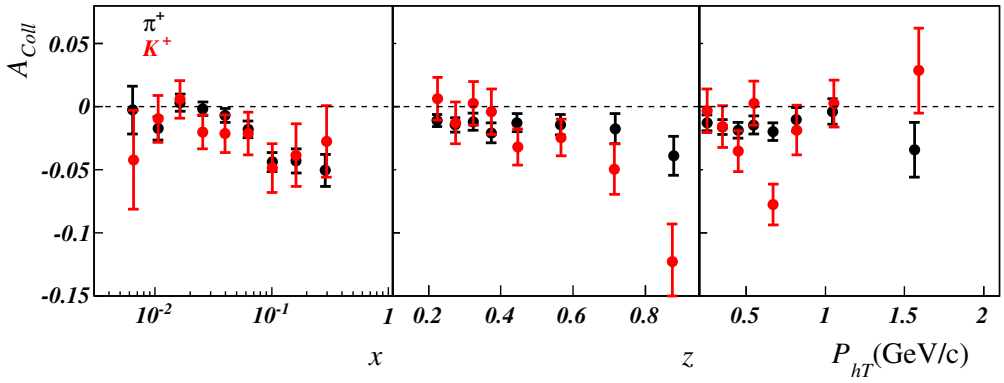

Figure 6.38: Collins asymmetries for positive pions (black points) and positive kaons (red points) as function of x, z and P_{hT}. The error bars are the statistical errors.

The π asymmetries are very similar to that obtained in the case of unidentified particles, as expected (the major part of the unidentified particles are pions). The lower statistics of kaons sample increases the statistical errors and makes less clear the trend of the data but there is a clear signal for positive kaons in the x valence region. The z and P_{hT} dependencies are similar to that obtained for the π sample but with a larger statistical uncertainty. The measured Sivers asymmetries for COMPASS 2010 data are shown in fig. 6.40 and in fig.6.41.

The results obtained for Sivers asymmetries of the pions are also very similar to the values obtained for the unidentified hadrons. In spite of the smaller statistics, the Sivers asymmetries for the positive kaons is positive and slightly larger than the corresponding values for positive pions.

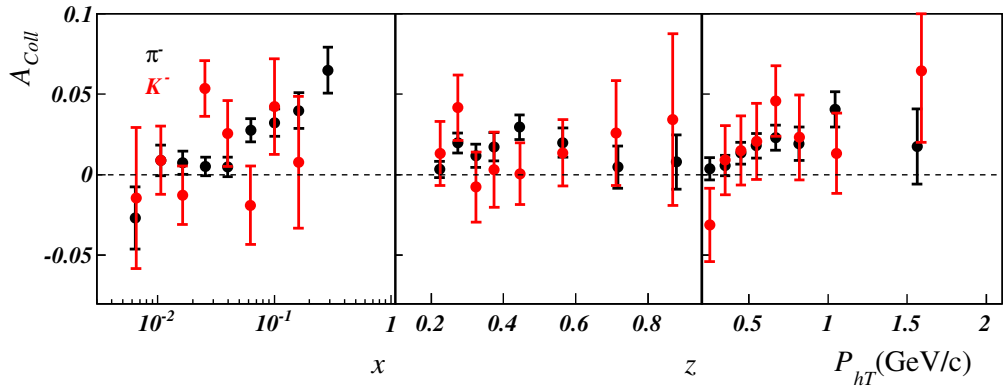

Figure 6.39: Collins asymmetries for negative pions (black points) and negative kaons (red points) as function of x, z and P_{hT}. The error bars are the statistical errors.

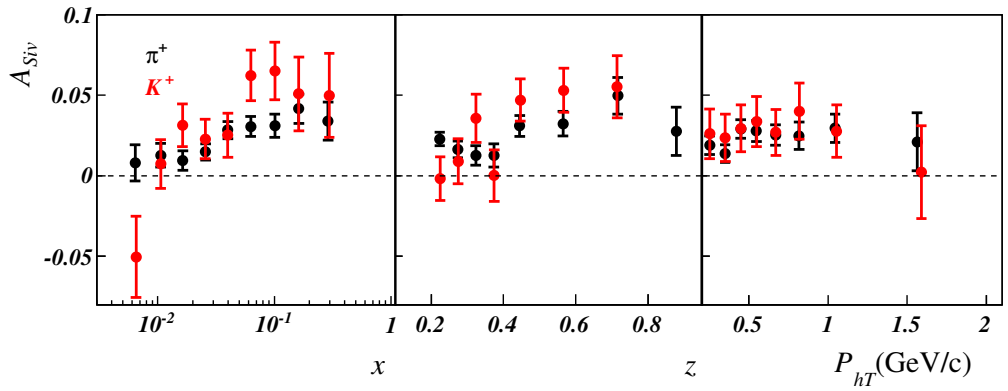

Figure 6.40: Sivers asymmetries for positive pions (black points) and positive kaons (red points) as function of x, z and P_{hT}. The error bars are the statistical errors.

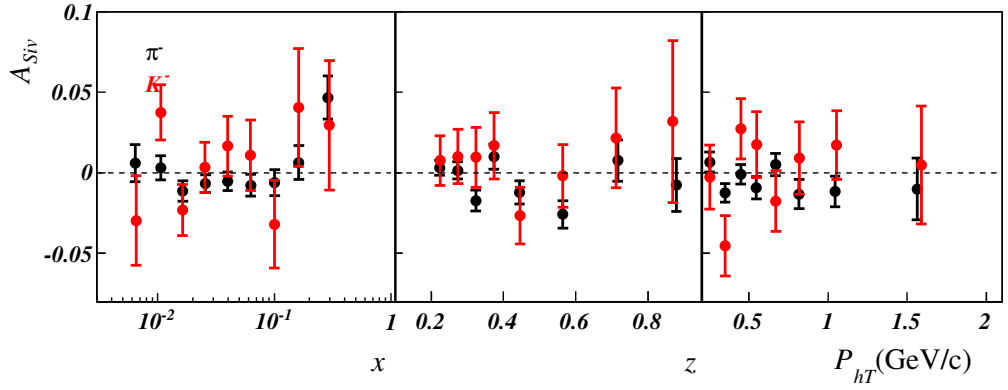

Figure 6.41: Sivers asymmetries for negative pions (black points) and negative kaons (red points) as function of x, z and P_{hT}. The error bars are the statistical errors.

6.4.2 Two-hadron asymmetries

The percentage of identified pairs obtained for all the possible combinations of oppositely charged identified hadrons is reported in table 6.2 for each period and for

the whole sample. The binning used for different combinations of oppositely charged hadron pairs is given in appendix B.

Table 6.2: Percentage of identified pairs obtained for all the possible combinations of oppositely charged identified hadrons for each period.

Period	K^+K^-	$K^+\pi^-$	π^+K^-	$\pi^+\pi^-$
1	1.75	4.41	3.22	60.50
2	1.81	4.56	3.26	60.76
3	1.80	4.56	3.28	60.52
4	1.79	4.54	3.24	60.88
5	1.70	4.34	3.13	60.60
6	1.80	4.57	3.28	60.77
7	1.80	4.57	3.30	60.77
8	1.79	4.57	3.29	60.88
9	1.78	4.55	3.27	60.83
10	1.78	4.54	3.27	61.00
11	1.77	4.57	3.24	61.30
12	1.77	4.54	3.27	61.14
Total	1.78	4.53	3.26	60.89

These values have been compared with the statistics from LEPTO events obtained considering 5000000 simulated events. All the cuts applied in the selection of the two-hadron pairs have been applied also to the simulated events. The main goal of this comparison is to investigate how much the identification efficiency depends on the type and charge of the identified particles for the event selection used in the analysis. The percentage of identified pairs obtained for the whole data sample, the same quantities obtained by the LEPTO simulation and the ratio between these values are reported in table 6.3.

Table 6.3: Percentage of identified pairs obtained for all the possible combinations of oppositely charged identified hadrons in the real case, for the whole data sample, for simulated events generated by LEPTO, and ratio between them.

Period	K^+K^-	$K^+\pi^-$	π^+K^-	$\pi^+\pi^-$
Real	1.78	4.53	3.26	60.89
LEPTO	2.5	5.6	4.8	64.2
LEPTO/Real	0.72	0.80	0.68	0.95

The ratio between the percentage of expected and reconstructed $\pi^+\pi^-$ pairs is close to 1, while this is not the case for the other combinations. This confirms that the efficiency depends on the type of particle. The percentage of real and simulated data depends also on the charge of the identified kaons, since the ratio between the percentage of expected and real $K^+\pi^-$ pairs is larger than the value obtained for π^+K^- pairs. From this result it seems that the identification efficiency is larger for positive kaons than for negative kaons. The invariant mass distributions from the LEPTO events obtained for all the combinations of oppositely charged pions and kaons are compared with the distributions obtained for real data in figs. 6.42, 6.43,

6.44 and 6.45. The peak in the $\pi^+\pi^-$ invariant mass distribution is due to the K^0 particles.

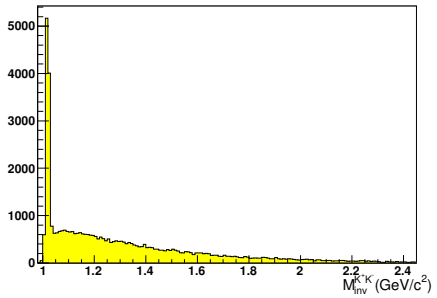

(a) Invariant mass distribution for K^+K^- pairs for the simulated data .

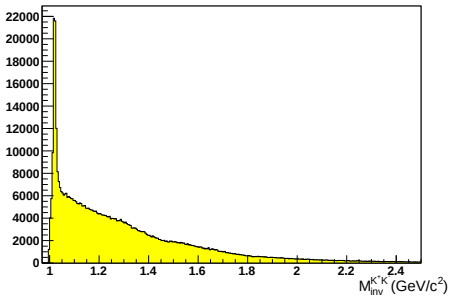

(b) Invariant mass distribution for K^+K^- pairs for the real data.

Figure 6.42: The invariant mass distributions for K^+K^- for the simulated, (a), and real, (b), data.

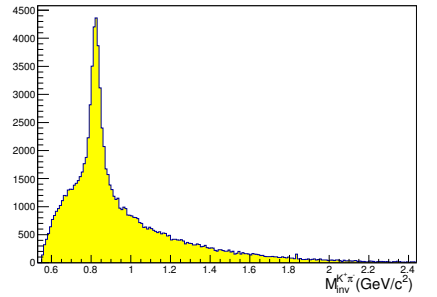

(a) Invariant mass distribution for $K^+\pi^-$ pairs for the simulated data.

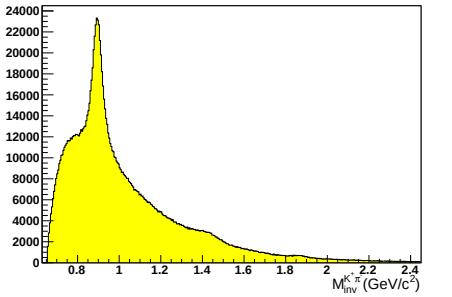

(b) Invariant mass distribution for $K^+\pi^-$ pairs for the real data.

Figure 6.43: The invariant mass distributions for $K^+\pi^-$ for the simulated, (a), and real, (b), data.

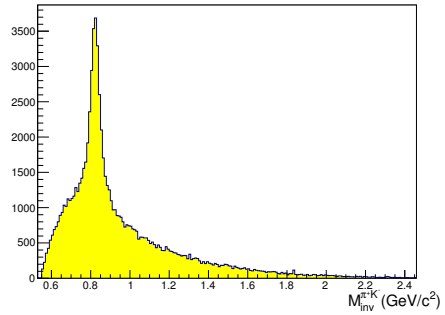

(a) Invariant mass distribution for π^+K^- pairs for the simulated data.

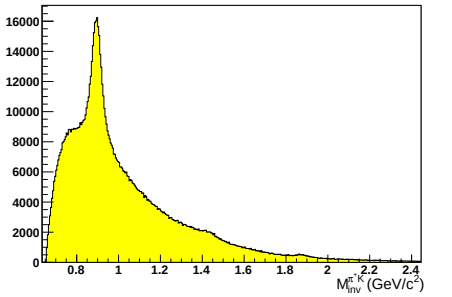

(b) Invariant mass distribution for π^+K^- pairs for the real data.

Figure 6.44: The invariant mass distributions for π^+K^- for the simulated, (a), and real, (b), data.

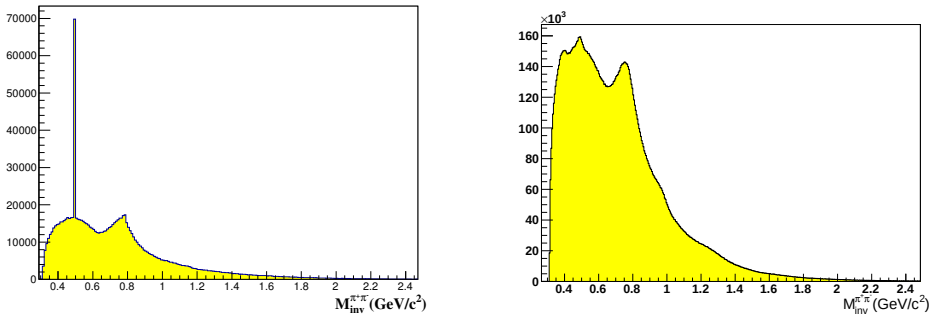

(a) Invariant mass distribution for $\pi^+\pi^-$ pairs for the simulated data.

(b) Invariant mass distribution for $\pi^+\pi^-$ pairs for the real data.

Figure 6.45: The invariant mass distributions for $\pi^+\pi^-$ for the simulated, (a), and real, (b), data.

The two-hadron asymmetries for identified $\pi^+\pi^-$ pairs as function of x, z and M_{inv} are shown in fig. 6.46. These results are very similar to those obtained for unidentified particles as expected because the major part of unidentified hadrons are pions. The comparison with the asymmetries obtained for unidentified particles is shown in fig. 6.47.

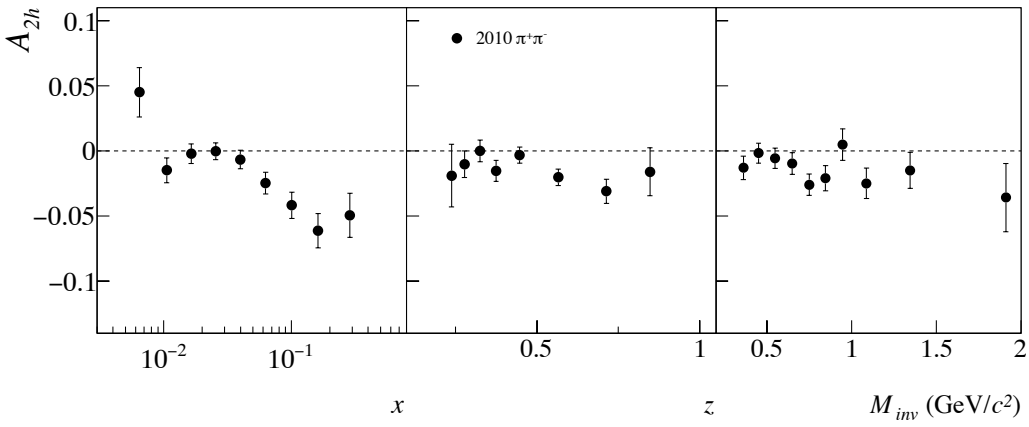

Figure 6.46: Two-hadron asymmetries from 2010 proton data for $\pi^+\pi^-$ pairs as a function of x,z and M_{inv}. The error bars are the statistical errors.

The two-hadron asymmetries for identified π^+K^- pairs and for $K^+\pi^-$ pairs as function of x, z and M_{inv} are shown in figs. 6.48 and 6.49, respectevely.

The small statistic does not allow to notice any particular dependence in x, z and M_{inv}. One can only remark that in the mean π^+K^- case the asymmetry is compatible with zero while in the $K^+\pi^-$ case the mean asymmetry as function of x seems to be different from zero. In the framework of the Artru model the two cases differ for the flavour of the struck quark, as shown in fig. 6.50 and in fig. 6.51, in the $K^+\pi^-$ case it is possible that the struck quark is a valence quark. Finally the asymmetries for identified K^+K^- pairs are shown in fig. 6.52.

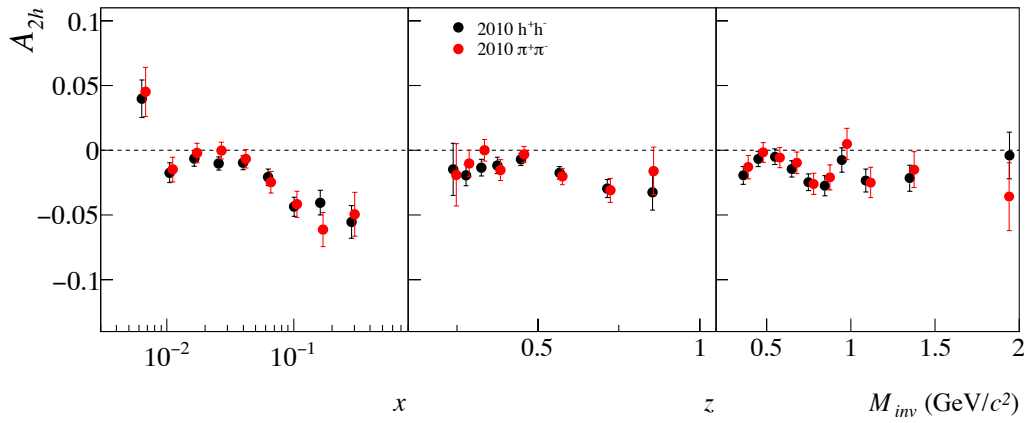

Figure 6.47: Two-hadron asymmetries from 2010 proton data for $\pi^+\pi^-$ as a function of x,z and M_{inv} (red points) compared with the results obtained for unidentified particles (black points). The error bars are the statistical errors.

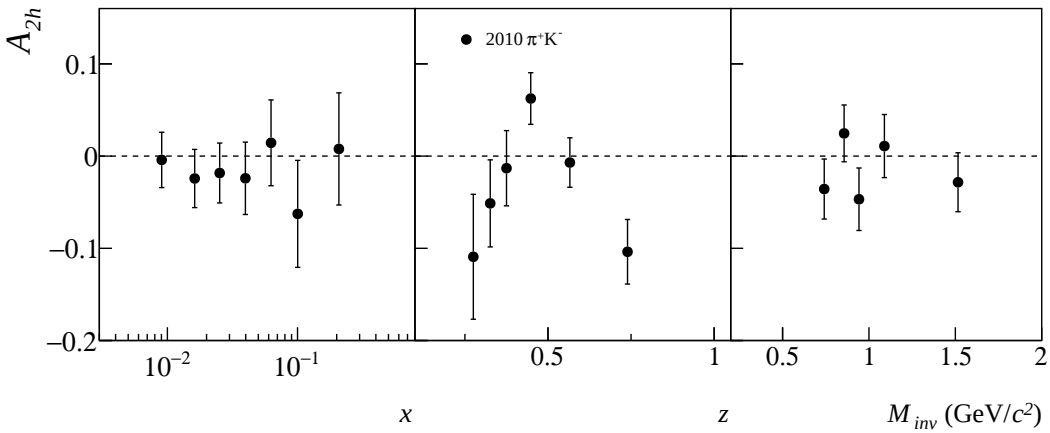

Figure 6.48: Two-hadron asymmetries from 2010 proton data for π^+K^- as a function of x,z and M_{inv}. The error bars are the statistical errors.

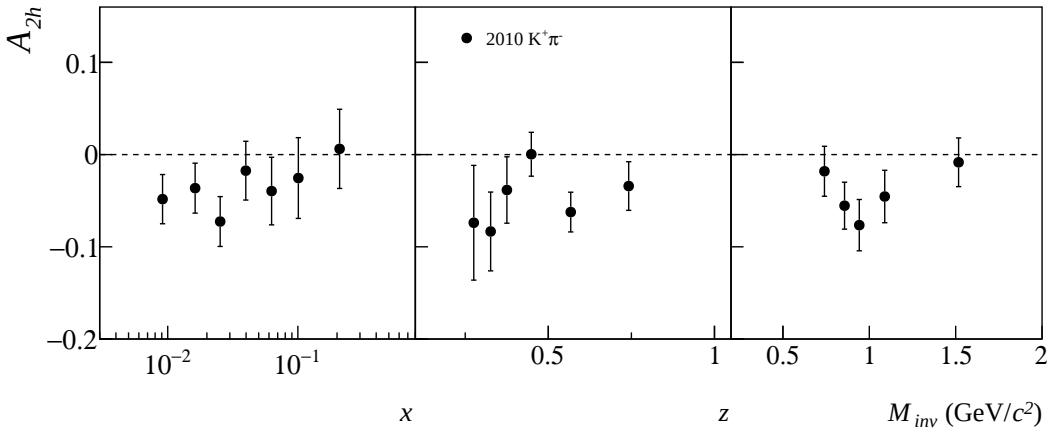

Figure 6.49: Two-hadron asymmetries from 2010 proton data for $K^+\pi^-$ as a function of x,z and M_{inv}. The error bars are the statistical errors.

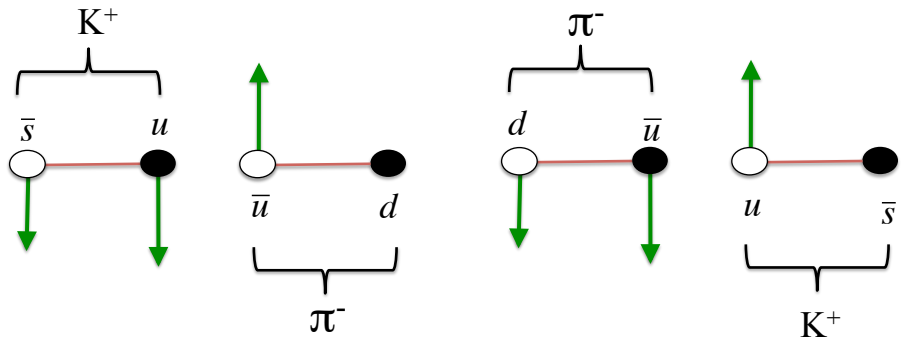

Figure 6.50: Interpretation of the two-hadron asymmetries from 2010 proton data for $K^+\pi^-$ in the framework of the Artru model.

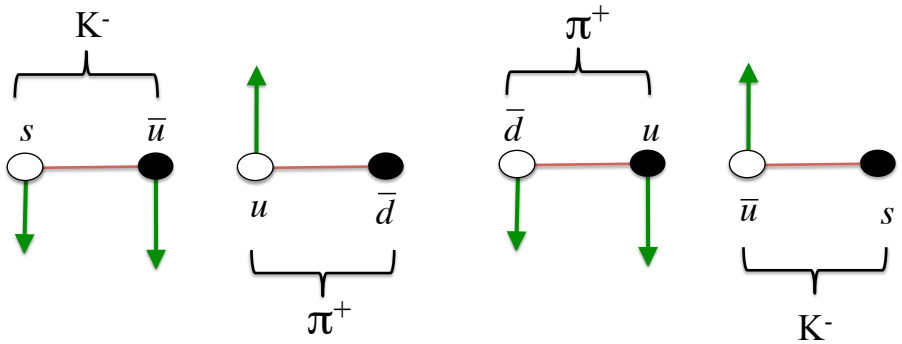

Figure 6.51: Interpretation of the two-hadron asymmetries from 2010 proton data for π^+K^- in the framework of the Artru model.

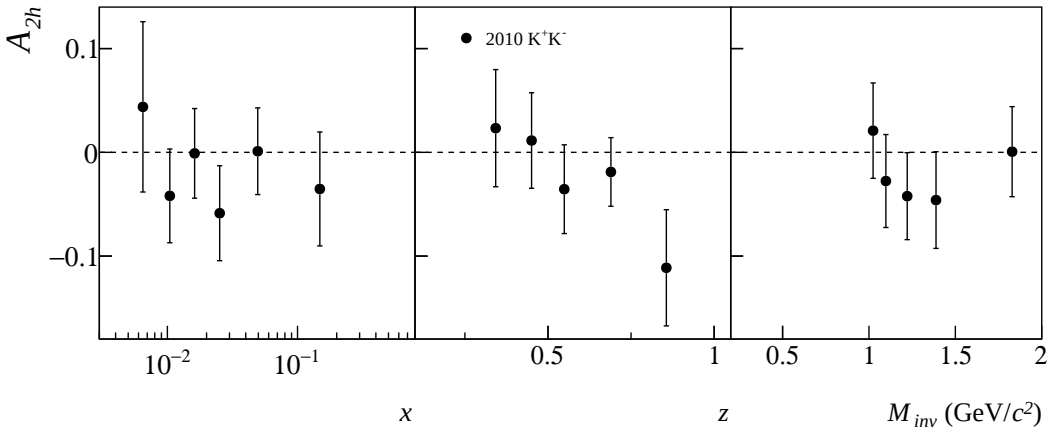

Figure 6.52: Two-hadron asymmetries from 2010 proton data for K^+K^- as a function of x,z and M_{inv}. The error bars are the statistical errors.

6.5 First extraction of the u and d transversity PDFs

A new method to access transversity from the two hadron asymmetries has been applied recently by Bacchetta and Radici to the HERMES data [61] and to the COMPASS [87] results from the 2007 proton data. The authors of [61] introduce the quantities:

$$n_q(Q^2) = \int dz dM_{inv}^2 D^{q\to\pi^+\pi^-}(z, M_{inv}^2, Q^2), \tag{6.2}$$

$$n^{\uparrow_q}(Q^2) = \int dz dM_{inv}^2 \frac{|R_T|}{M_{inv}} H_1^{\sphericalangle q\to\pi^+\pi^-}(z, M_{inv}^2, Q^2), \tag{6.3}$$

where the quantities R_T,$D^{q\to\pi^+\pi^-}(z, M_{inv}^2, Q^2)$ and $H_1^{\sphericalangle q\to\pi^+\pi^-}(z, M_{inv}^2, Q^2)$ have been defined in sec. 3.2 and use the Belle data to evaluate their ratio.

They find:

$$n^{\uparrow_q}(Q^2)/n_q(Q^2) = -0.273 \pm 0.007\,(\text{exp.}) \pm 0.009\,(\text{th.}), \tag{6.4}$$

at BELLE mean $\langle Q^2\rangle$ value (100 (GeV/c)^2). Further the authors evolved down the the Di-hadron FF to the HERMES mean $\langle Q^2\rangle$ value (2.5 (GeV/c)^2) obtaining a value about 10 % smaller in absolute value :

$$n^{\uparrow_q}(Q^2)/n_q(Q^2) = -0.251 \pm 0.006\,(\text{exp.}) \pm 0.023\,(\text{th.}). \tag{6.5}$$

If one replaces in eq. (3.11) the definitions given in eq. (6.2) and eq. (6.3) the two hadron asymmetry on proton can be written as

$$A_{2h} = \frac{\sum_q e_q^2 h_1^q(x) n_q^{\uparrow}(Q^2)}{\sum_q e_q^2 f_1^q(x) n_q(Q^2)} \tag{6.6}$$

or

$$\sum_q e_q^2 h_1^q(x) n_q^{\uparrow}(Q^2) = A_{2h} \sum_q e_q^2 f_1^q(x) n_q(Q^2). \tag{6.7}$$

In the case of transversely polarized proton target one obtains:

$$\begin{aligned} &\frac{4}{9}x(h_1^u n_u^{\uparrow} + h_1^{\overline{u}} n_{\overline{u}}^{\uparrow}) + \frac{1}{9}x(h_1^d n_d^{\uparrow} + h_1^{\overline{d}} n_{\overline{d}}^{\uparrow} + h_1^s n_s^{\uparrow} + h_1^{\overline{s}} n_{\overline{s}}^{\uparrow}) \\ &= A_{2h}\left(\frac{4}{9}x(f_1^u n_u + f_1^{\overline{u}} n_{\overline{u}}) + \frac{1}{9}x(f_1^d n_d + f_1^{\overline{d}} n_{\overline{d}}) + \frac{1}{9}x(f_1^s n_s + f_1^{\overline{s}} n_{\overline{s}})\right) \end{aligned} \tag{6.8}$$

where the $c(\overline{c})$ contribution has been neglected. On the basis of isospin symmetries and charge conjugation the following assumptions are made:

$$\begin{aligned} D_1^u &= D_1^d = D_1^{\overline{u}} = D_1^{\overline{d}}, \\ D_1^s &= D_1^{\overline{s}}, D_1^c = D_1^{\overline{c}}, \\ H_1^{\sphericalangle u} &= -H_1^{\sphericalangle d} = -H_1^{\sphericalangle \overline{u}} = H_1^{\sphericalangle \overline{d}}, \\ H_1^{\sphericalangle s} &= -H_1^{\sphericalangle \overline{s}} = H_1^{\sphericalangle c} = -H_1^{\sphericalangle \overline{c}} = 0, \end{aligned} \tag{6.9}$$

which imply:

$$n_u^{\uparrow} = -n_d^{\uparrow} = -n_{\overline{u}}^{\uparrow} = n_{\overline{d}}^{\uparrow}, \tag{6.10}$$

$$\begin{aligned} n_u = n_d = n_{\overline{u}} = n_{\overline{d}}, \\ n_s = n_{\overline{s}}. \end{aligned} \tag{6.11}$$

In one of the two scenarios proposed in [61] in which it is assumed $n_s = n_{\overline{s}} = n_u = n_d = n_{\overline{u}} = n_{\overline{d}}$, and taking into account the eq. 6.11 and eq. 6.10, from eq. 6.8 we obtain:

$$xh_1^{u_v}(x) - \frac{1}{4}xh_1^{d_v}(x) = A_{2h}\frac{n_u(Q^2)}{n_u^{\uparrow}(Q^2)}x(f_1^u(x) + f_1^{\overline{u}}(x) + \frac{1}{4}(f_1^d(x) + f_1^{\overline{d}}(x) + f_1^s(x) + f_1^{\overline{s}}(x)). \tag{6.12}$$

The method thus allows to extract a combination of the transversity PDFs in an almost model-independent way, using only the two-hadron asymmetry and the Belle data and does not involve convolutions on the intrinsic momentum, and the Belle data.

The $f_1^q(x)$ quantities on the left hand of the eq. 6.12 can be obtained from the MSTW08LO PDF set [88] shown in fig. 6.53.

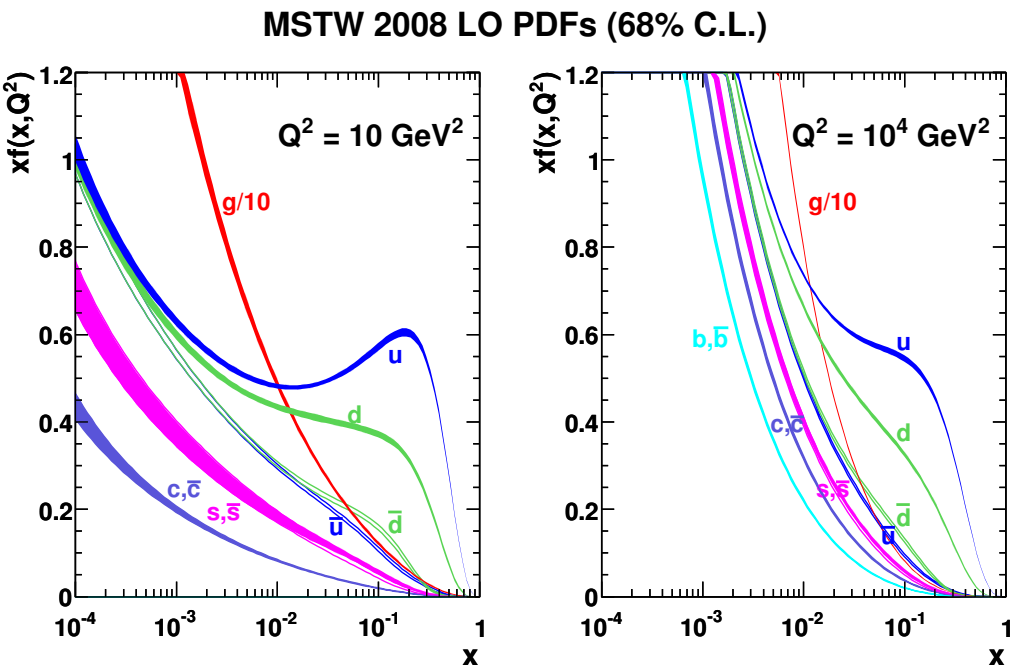

Figure 6.53: The unpolarized PDF f_1 from the MSTW08LO PDF parametrization [88] at $\langle Q^2 \rangle = 10$ (GeV/c)^2 (left panel) and $\langle Q^2 \rangle = 10^4$ (GeV/c)^2 (right panel).

Here we have used this method to evaluate the quantity $xh_1^{u_v}(x) - \frac{1}{4}xh_1^{d_v}(x)$ from the two-hadron asymmetry measured from the 2010 transverse proton data

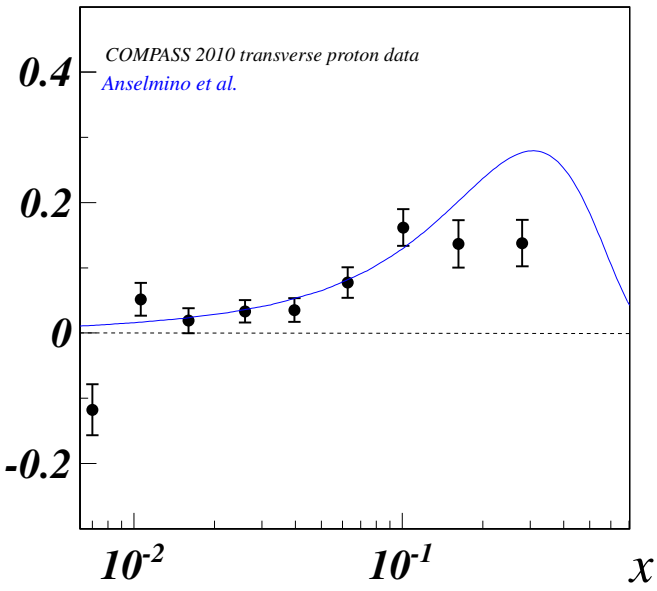

Figure 6.54: $xh_1^{u_v}(x) - \frac{1}{4}xh_1^{d_v}(x)$ function from the two-hadron asymmetries from the COMPASS ($\langle Q^2\rangle = 3.8$ (GeV/c)^2) 2010 transverse proton data.The curve shows the same combination of the transversity PDFs obtained from the global fit of the Torino group at $\langle Q^2\rangle = 2.4$ (GeV/c)^2 [53].

and the results are shown in fig. 6.54. The curve shows the same combination of the transversity PDFs obtained from the global fit of the Torino group [53]. As can be seen the agreement is rather good. Taking advantage of the COMPASS deuteron data, it is possible to disantangle the u and d transversity PDFs. For neutrons eq. 6.7 becomes:

$$\begin{aligned} &\frac{4}{9}x(h_{1N}^{u}n_u^{\uparrow} + h_{1N}^{\overline{u}}n_{\overline{u}}^{\uparrow}) + \frac{1}{9}x(h_{1N}^{d}n_d^{\uparrow} + h_{1N}^{\overline{d}}n_{\overline{d}}^{\uparrow} + h_{1N}^{s}n_s^{\uparrow} + h_{1N}^{\overline{s}}n_{\overline{s}}^{\uparrow}) \\ &= A_{2h}\left(\frac{4}{9}x(f_{1N}^{u}n_u + f_{1N}^{\overline{u}}n_{\overline{u}}) + \frac{1}{9}x(f_{1N}^{d}n_d + f_{1N}^{\overline{d}}n_{\overline{d}}) + \frac{1}{9}x(f_{1N}^{s}n_s + f_{1N}^{\overline{s}}n_{\overline{s}})\right), \end{aligned} \tag{6.13}$$

where f_{1N}^q and h_{1N}^q are the neutron PDFs which are related to the proton PDFs by the relations:

$$\begin{aligned} h_{1N}^{u(\overline{u})} = h_1^{d(\overline{d})}, h_{1N}^{d(\overline{d})} = h_1^{u(\overline{u})}, h_{1N}^{s(\overline{s})} = h_1^{s(\overline{s})} \\ f_{1N}^{u} = f_1^{d}, f_{1N}^{d} = f_1^{u}, f_{1N}^{s} = f_1^{s}. \end{aligned} \tag{6.14}$$

If we replace eq. 6.14 in eq. 6.13 and take into account eq. 6.11 and eq. 6.10, we obtain for the deuteron:

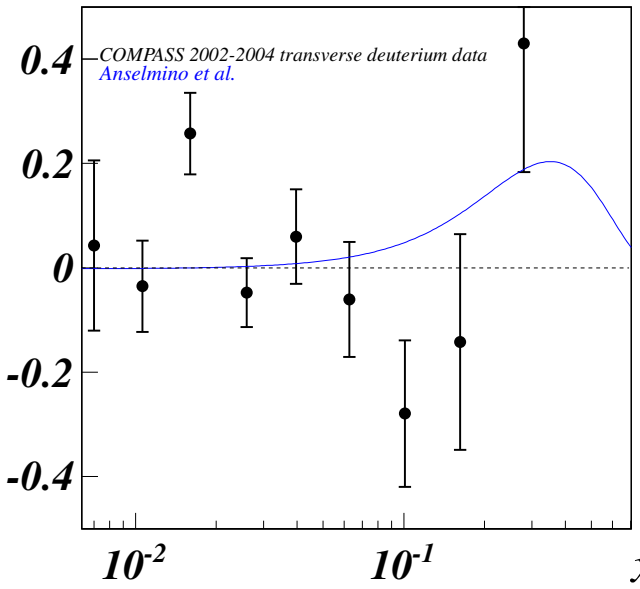

Figure 6.55: $xh_1^{u_v}(x)+xh_1^{d_v}(x)$ function from the two-hadron asymmetries from the COMPASS ($\langle Q^2\rangle = 3.8$ (GeV/c)^2) transverse deuteron data.The curve shows the same combination of the transversity PDFs obtained from the global fit of the Torino group at $\langle Q^2\rangle = 2.4$ (GeV/c)^2 [53].

$$\begin{aligned}&\frac{3}{9}(xh_1^{u_v}(x)+xh_1^{d_v}(x))\\&=\frac{5}{9}A_{2h}\frac{n_u(Q^2)}{n_u^{\uparrow}(Q^2)}x(f_1^u(x)+f_1^{\overline{u}}(x)+f_1^d(x)+f_1^{\overline{d}}(x)+\frac{2}{5}(f_1^s(x)+f_1^{\overline{s}}(x))).\end{aligned}\tag{6.15}$$

It is interesting to note that on the left side the transversity functions of the $u-$ and $d-$quark have the same weight (at variance with the proton case, eq. 6.12). This is due to the isoscalar nature of the deuteron target. In fig. 6.55 the quantity $xh_1^{u_v}(x)+xh_1^{d_v}(x)$ is compared with the same combination of the transversity PDFs obtained from the global fit of the Torino group [53]. The $xh_1^{u_v}(x)+xh_1^{d_v}(x)$ curve evaluated from the 2002-2004 COMPASS deuteron data is not in agreement with the function obtained by the global fit [53].

Using the proton and the deuteron COMPASS asymmetries, which are measured at the same x and $\langle Q^2\rangle$ values, one can obtain, in a straightforward way, h_1^u and h_1^d. The results we have obtained for h_1^u of are shown in fig. 6.56. The h_1^u results from the 2010 COMPASS data are in agreement with the results obtained by the global fit in particular at small x. Since h_1 has been extracted in two totally different methods this result is very important and constitutes a strong argoment to support these recent theoretical developments. For $x > 0.05$ the results of COMPASS seem to be systematically smaller than the global fit results [53]. Since in the evaluation of the $n^{\uparrow_q}(Q^2)/n_q(Q^2)$ ratio in [87] the authors have considered only the M_{inv} HERMES

range (0.5 GeV/c^2< M_{inv}<1.1 GeV/c^2), we have verified if this difference is due to the different COMPASS invariant mass range. We have evaluated the analysing power in COMPASS M_{inv} range and in the HERMES M_{inv} range, finding that their difference cannot explain the observed discrepancy. The results for h_1^d are shown in fig. 6.57 where they are compared with the corresponding transversity PDF extracted with the global fit by the Torino group [53]. In spite of the large error bars, due to the poor statistics of the deuteron data, this result is important. In first place, this is the first extraction of the transversity PDF for the different quark flavours from the two-hadron asymmetry measured at COMPASS. Secondly, it allows to evaluate the kind of precision which is necessary to measure the d-quark transversity. From eq. 6.15 it is clear that from a good measurement of SIDIS on deuteron the d-quark transversity can be as precise as the u-quark transversity. Taking into account the better figure-of-merit of the deuteron (^{6}LiD) target with respect to the proton (NH_3) target, a full year measurement of SIDIS on a transversely polarized deuteron target would make a major contribution to the field.

Due to the large statistical error in the h_1^d results from the 2010 COMPASS data it is only possible to conclude that there is a qualitative agreement with the global fit of the Torino group [53].

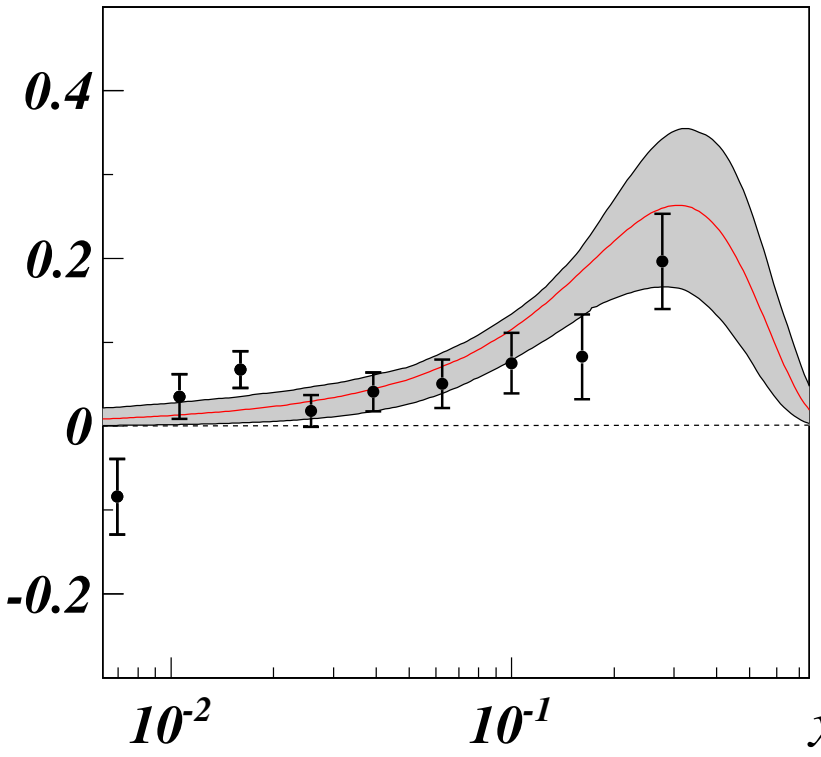

Figure 6.56: $xh_1^u(x)$ function obtained combining the results from the two-hadron asymmetries from the COMPASS ($\langle Q^2 \rangle = 3.8$ (GeV/c)^2) 2010 transverse proton data and the 2002-2004 transverse deuteron data.The curve shows the $xh_1^u(x)$ transversity PDFs obtained from the global fit of the Torino group at $\langle Q^2 \rangle = 2.4$ (GeV/c)^2 [53].

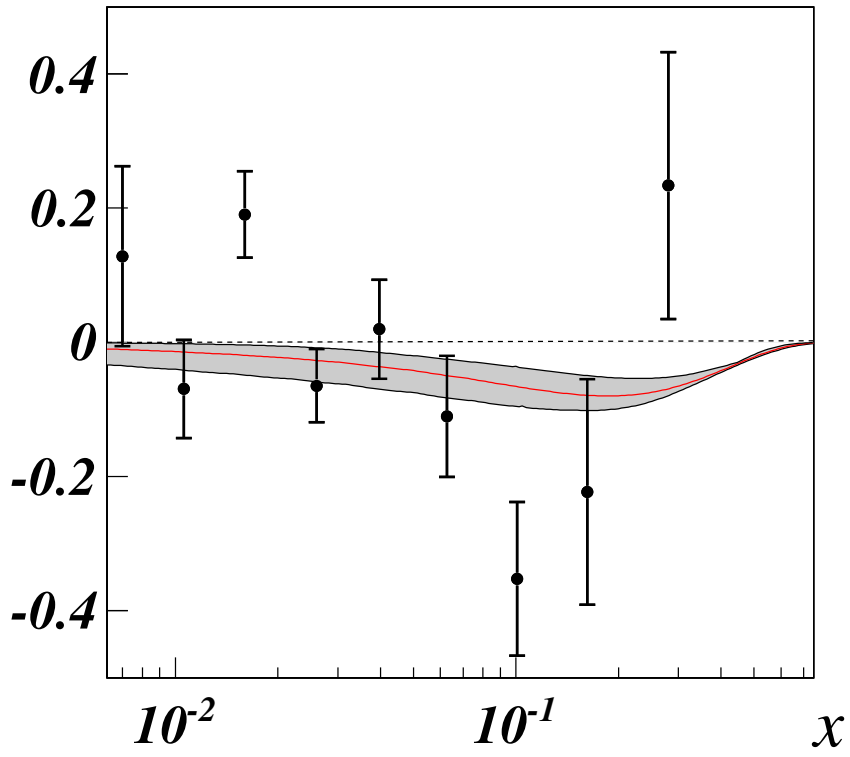

Figure 6.57: $xh_1^d(x)$ function obtained combining the results from the two-hadron asymmetries from the COMPASS ($\langle Q^2 \rangle = 3.8$ (GeV/c)^2) 2010 transverse proton data and the 2002-2004 transverse deuteron data.The curve shows the $xh_1^d(x)$ transversity PDFs obtained from the global fit of the Torino group at $\langle Q^2 \rangle = 2.4$ (GeV/c)^2 [53].

Chapter 7

Conclusions and outlook

COMPASS has contributed and is contributing considerably to the study of the spin structure of the nucleon, covering both longitudinal- and transverse-spin phenomena. In particular, COMPASS is a pioneer experiment in the investigation of the role of transverse-spin effects and transverse momentum of the nucleon constituents giving a fundamental contribution to the knowledge of the transversity PDF. The 2002-2004 COMPASS deuteron results together with the results obtained by HERMES (on protons), and Belle, allowed the first extraction of the transversity PDF. These important measurement provided convincing evidence that the transversity can be definitively considered different from zero. At the time transversity was extracted from the measurement of the Collins fragmentation function at Belle and from the measurement of the Collins asymmetries in SIDIS. Still, a different channel was available to access transversity: the two-hadron production in SIDIS and the production of two pairs of hadrons in e^+e^- annihilation. The importance of this channel is due to the fact that the PDF and the FF in two-hadron production cross-section are not convoluted, but enter with a simple product simplifying the extrapolation. In this case transversity can be measured without introducing hypothesis on the dependence of the PDF and FF on the transverse momentum of the struck quark. The disadvantage of this measurement is related to the necessity to have a large number of events with at least two hadrons in the final state, which can be obtained only with high energy beam experiment. Up to 2005 the only two-hadron asymmetry results available were those measured by COMPASS on the deuteron, compatible with zero, and that measured by HERMES on proton target, but the low statistic of HERMES did not allow to perform the extraction of transversity from this channel. The 2007 COMPASS data gave a clear signal in this channel and allowed to have a more precise estimation of the two-hadron asymmetry with respect to the HERMES measurement. The measurement of a non zero two-hadron asymmetry with an amplitude comparable with that obtained for the Collins effect has confirmed all the theoretical suggestions about a new way to access transversity. The 2010 COMPASS run has been fully dedicated to the aim of improving the statistical error by a factor two and performing a more precise measurement. This goal has been achieved. The 2010 data have an excellent quality, the analysis has progressed quick rapidly and the results have confirmed the previous results and clarified several open points, for instance the interesting two-hadron asymmetry dependence on the invariant mass of the hadron pair. Of the greatest

importance is the confirmation of the size of the Sivers asymmetry, which is a direct evidence of non-zero orbital angular momentum of the quarks. The results of 2010 have been presented at Transversity 2011 conference (Veli Lošinj, Croatia) and at DSPIN2011 (Dubna, Russia). These new data together with the Belle measurement of the di-hadron fragmentation function and the COMPASS deuteron data allowed for the first time the extraction of the h_1^d and h_1^u PDFs from two-hadron asymmetry. This extraction has been done for the first time, and the results will be published.

This measurement has allowed to extract the transversity PDF in a totally different method, and represents the most important aspect of my thesis work because it is the beginning of a new way to access transversity.

Of course the low statistics in the COMPASS deuteron data do not allow to perform a precise measurement of the h_1 of the d-quark and a new data taking with polarized deuteron target would allow to improve considerably the measurement of the transversity. Further contributions will come from the JLab experiments after the 2015 upgrade but in a Q^2 range smaller with respect to the COMPASS range. In this thesis I present also new results on the Collins, Sivers and two-hadron asymmetries for identified hadrons, namely pions and kaons. These results, not yet shown at conferences, are very important to investigate the flavour dependence of the various PDF.

In any case the investigation on transverse-spin effects in SIDIS has given very successful results improving considerably the knowledge of the spin structure.

Appendix A

The light cone coordinates

If we consider a 4-vector x^μ we define the light-con components x^+ and x^- as:

$$\begin{aligned} x^+ &= \frac{x^0 + x^3}{\sqrt{2}}, \\ x^- &= \frac{x^0 - x^3}{\sqrt{2}}. \end{aligned} \tag{A.1}$$

The coordinates x^1 and x^2 remain the same so the x^μ 4-vector in the light-cone coordinates become:

$$x^\mu = (x^+, x^-, x^1, x^2) = (x^+, x^-, \boldsymbol{x}_T) \tag{A.2}$$

The scalar product between two vectors in light-cone coordinates is given by:

$$x \cdot y = x^- y^+ + x^+ y^- - x^1 y^1 - x^2 y^2 \tag{A.3}$$

The x^μ can be written in terms of the Sudakov vectors n_+ and n_- (with n_+ =(1,0,0,0) and n_- =(0,1,0,0)) as:

$$x^\mu = x^+ n_+ + x^- n_- + x_T. \tag{A.4}$$

Considering the 4-momentum $P^\mu = (P^0, P^1, P^2, P^3)$ in the collinear frame (in which only the 1 and 2 components are zero) we obtain $P^\mu = (P^0, 0, 0, P^3)$ and $P^\mu P_\mu = M^2 = (P^0)^2 - (P^3)^2 = (P^0 - P^3)(P^0 + P^3)$

From this result we obtain that P^μ in light-cone coordinates and in the collinear case can become:

$$P^\mu = \left(\frac{P^0 + P^3}{\sqrt{2}}, \frac{P^0 - P^3}{\sqrt{2}}, 0, 0 \right) = \left(P^+, \frac{2M^2}{P^+}, 0, 0 \right). \tag{A.5}$$

In this expression it is clear that in DIS regime the dominant component is the "plus" component and so (in DIS processes) the light-cone reference frame allows to take into account only the plus component with obvious advantages.

Appendix B

Binning for two hadron analysis

Table B.1: Binning used in the two-hadron asymmetries extraction for sample with $x > 0.032$.

bin	x	z	M_{inv} (GeV/c^2)
1	$[0.032 - 0.050]$	$[0.20 - 0.25]$	$[0.0 - 0.4]$
2	$[0.050 - 0.080]$	$[0.25 - 0.30]$	$[0.4 - 0.5]$
3	$[0.080 - 0.130]$	$[0.30 - 0.35]$	$[0.5 - 0.6]$
4	$[0.130 - 0.210]$	$[0.35 - 0.40]$	$[0.6 - 0.7]$
5	$[0.210 - 0.700]$	$[0.40 - 0.50]$	$[0.7 - 0.8]$
6		$[0.50 - 0.65]$	$[0.8 - 0.9]$
7		$[0.65 - 0.80]$	$[0.9 - 1.0]$
8		$[0.80 - 1.00]$	$[1.0 - 1.2]$
9			$[1.2 - 1.6]$
10			$[1.6 - 100]$

Table B.2: Binning used in the two-hadron asymmetries extraction for identified $\pi^+\pi^-$ pairs.

bin	x	z	M_{inv} (GeV/c^2)
1	$[0.003 - 0.008]$	$[0.20 - 0.25]$	$[0.0 - 0.4]$
2	$[0.008 - 0.013]$	$[0.25 - 0.30]$	$[0.4 - 0.5]$
3	$[0.013 - 0.020]$	$[0.30 - 0.35]$	$[0.5 - 0.6]$
4	$[0.020 - 0.032]$	$[0.35 - 0.40]$	$[0.6 - 0.7]$
5	$[0.032 - 0.050]$	$[0.40 - 0.50]$	$[0.7 - 0.8]$
6	$[0.050 - 0.080]$	$[0.50 - 0.65]$	$[0.8 - 0.9]$
7	$[0.080 - 0.130]$	$[0.65 - 0.80]$	$[0.9 - 1.0]$
8	$[0.130 - 0.210]$	$[0.80 - 1.00]$	$[1.0 - 1.2]$
9	$[0.210 - 0.700]$		$[1.2 - 1.6]$
10			$[1.6 - 100]$

Table B.3: Binning used in the two-hadron asymmetries extraction for identified π^+K^- and $K^+\pi^-$ pairs.

bin	x	z	M_{inv} (GeV/c^2)
1	$[0.003 - 0.013]$	$[0.20 - 0.30]$	$[0.0 - 0.8]$
2	$[0.013 - 0.020]$	$[0.30 - 0.40]$	$[0.8 - 0.9$
3	$[0.020 - 0.032]$	$[0.40 - 0.50]$	$[0.9 - 1.0]$
4	$[0.032 - 0.050]$	$[0.50 - 0.65]$	$[1.2 - 100]$
5	$[0.080 - 0.130]$	$[0.65 - 1.00]$	
6	$[0.130 - 0.700]$		

Table B.4: Binning used in the two-hadron asymmetries extraction for identified K^+K^- pairs.

bin	x	z	M_{inv} (GeV/c^2)
1	$[0.003 - 0.008]$	$[0.20 - 0.40]$	$[0.9 - 0.8]$
2	$[0.008 - 0.013]$	$[0.40 - 0.50]$	$[0.8 - 0.9$
3	$[0.020 - 0.032]$	$[0.50 - 0.60]$	$[0.9 - 1.0]$
4	$[0.032 - 0.050]$	$[0.60 - 0.80]$	$[1.2 - 100]$
5	$[0.080 - 1.00]$	$[0.80 - 1.00]$	

Appendix C

Asymmetries and mean values for standard samples

Table C.1: Value of the two-hadron asymmetries and mean value of the fundamental kinematical variables in x bins (1/2).

x bin	A	stat	sys	$< x >$	$< Q^2$ (GeV/c)$^2 >$
1	0.040	0.014	0.011	0.006	1.267
2	-0.017	0.008	0.006	0.011	1.558
3	-0.006	0.006	0.005	0.016	1.878
4	-0.010	0.005	0.004	0.026	2.303
5	-0.010	0.005	0.004	0.040	3.113
6	-0.021	0.006	0.005	0.063	4.796
7	-0.044	0.007	0.005	0.101	7.496
8	-0.040	0.010	0.008	0.162	11.885
9	-0.055	0.013	0.010	0.285	23.014

Table C.2: Value of the two-hadron asymmetries and mean value of the fundamental kinematical variables in x bins (2/2).

x bin	$< y >$	$< z >$	$< W >$	$< M_{inv}$(GeV/c$^2) >$	$< D_{NN} >$
1	0.646	0.446	14.192	0.783	0.563
2	0.474	0.453	12.088	0.763	0.770
3	0.360	0.462	10.504	0.744	0.869
4	0.277	0.472	9.169	0.726	0.908
5	0.237	0.477	8.394	0.706	0.928
6	0.233	0.478	8.120	0.700	0.933
7	0.229	0.479	7.945	0.694	0.937
8	0.223	0.481	7.623	0.685	0.939
9	0.256	0.485	7.321	0.678	0.931

Table C.3: Value of the two-hadron asymmetries and mean value of the fundamental kinematical variables in z bins (1/2).

z bin	A	stat	sys	$< x >$	$< Q^2$ (GeV/c)$^2 >$
1	-0.015	0.020	0.015	0.238	3.968
2	-0.019	0.008	0.006	0.278	3.902
3	-0.013	0.007	0.005	0.326	3.875
4	-0.012	0.006	0.005	0.375	3.865
5	-0.007	0.005	0.004	0.448	3.860
6	-0.017	0.005	0.004	0.567	3.837
7	-0.029	0.007	0.005	0.714	3.740
8	-0.033	0.014	0.011	0.854	2.930

Table C.4: Value of the two-hadron asymmetries and mean value of the fundamental kinematical variables in z bins (2/2).

z bin	$< y >$	$< z >$	$< W >$	$< M_{inv}$(GeV/c$^2) >$	$< D_{NN} >$
1	0.481	0.032	11.604	0.513	0.766
2	0.406	0.039	10.539	0.583	0.828
3	0.369	0.043	9.995	0.636	0.854
4	0.351	0.045	9.708	0.677	0.867
5	0.335	0.048	9.460	0.724	0.878
6	0.319	0.050	9.207	0.789	0.889
7	0.306	0.051	9.015	0.862	0.897
8	0.336	0.035	0.810	0.732	0.873

Table C.5: Value of the two-hadron asymmetries and mean value of the fundamental kinematical variables in M_{inv} bins (1/2).

M_{inv} bin	A	stat	sys	$< M_{inv}(\mathrm{GeV/c^2}) >$	$< Q^2\ (\mathrm{GeV/c})^2 >$
1	-0.019	0.007	0.005	0.361	3.863
2	-0.007	0.006	0.005	0.451	3.848
3	-0.005	0.006	0.005	0.549	3.846
4	-0.014	0.006	0.005	0.650	3.839
5	-0.025	0.006	0.005	0.749	3.785
6	-0.027	0.008	0.006	0.846	3.821
7	-0.008	0.009	0.007	0.947	3.866
8	-0.023	0.009	0.007	1.090	3.844
9	-0.021	0.010	0.008	1.350	3.839
10	-0.004	0.018	0.014	1.942	3.889

Table C.6: Value of the two-hadron asymmetries and mean value of the fundamental kinematical variables in M_{inv} bins (2/2).

M_{inv} bin	A	stat	sys	$< M_{inv}(\mathrm{GeV/c^2} >$	$< Q^2\ (\mathrm{GeV/c})^2 >$
1	-0.019	0.007	0.005	0.361	3.863
2	-0.007	0.006	0.005	0.451	3.848
3	-0.005	0.006	0.005	0.549	3.846
4	-0.014	0.006	0.005	0.650	3.839
5	-0.025	0.006	0.005	0.749	3.785
6	-0.027	0.008	0.006	0.846	3.821
7	-0.008	0.009	0.007	0.947	3.866
8	-0.023	0.009	0.007	1.090	3.844
9	-0.021	0.010	0.008	1.350	3.839
10	-0.004	0.018	0.014	1.942	3.889

List of Tables

List of Figures

Bibliography

[1] J. D. Bjorken, Phys. Rev. **179** (1969) 1547.

[2] M. J. Alguard *et al.*, Phys. Rev. Lett. **41** (1978) 70.

[3] J. Ashman *et al.* [European Muon Collaboration], Phys. Lett. B **206** (1988) 364.

[4] D. Adams *et al.* [Spin Muon Collaboration (SMC)], Phys. Rev. D **56** (1997) 5330

[5] M. Alekseev *et al.* [COMPASS Collaboration], Phys. Lett. B **676** (2009) 31

[6] J. P. Ralston and D. E. Soper, Nucl. Phys. B **152** (1979) 109.

[7] V. Barone, A. Drago and P. G. Ratcliffe, Phys. Rept. **359**, 1 (2002)

[8] A. Bacchetta, arXiv:hep-ph/0212025.

[9] V. Barone, F. Bradamante and A. Martin, Prog. Part. Nucl. Phys. **65** (2010) 267

[10] T. Muta, World Sci. Lect. Notes Phys. **57** (1998) 1.

[11] R. L. Jaffe, arXiv:hep-ph/9602236.

[12] C. Amsler *et al.* [Particle Data Group], Phys. Lett. B **667** (2008) 1.

[13] A. Bacchetta, arXiv:1111.6642 [hep-ph].

[14] M. Anselmino *et al.*, arXiv:0807.0173 [hep-ph].

[15] J. Soffer, M. Stratmann and W. Vogelsang, Phys. Rev. D **65** (2002) 114024

[16] V. A. Korotkov, W. D. Nowak and K. A. Oganesian, Eur. Phys. J. C **18** (2001) 639

[17] P. Schweitzer, D. Urbano, M. V. Polyakov, C. Weiss, P. V. Pobylitsa and K. Goeke, Phys. Rev. D **64** (2001) 034013

[18] M. Wakamatsu, Phys. Lett. B **653** (2007) 398

[19] B. Pasquini, M. Pincetti and S. Boffi, Phys. Rev. D **72** (2005) 094029

[20] I. C. Cloet, W. Bentz and A. W. Thomas, Phys. Lett. B **659** (2008) 214

[21] A. Bacchetta, F. Conti and M. Radici, Phys. Rev. D **78** (2008) 074010

[22] A. Kotzinian, Nucl. Phys. B **441** (1995) 234

[23] D. Boer and P. J. Mulders, Phys. Rev. D **57** (1998) 5780

[24] P. J. Mulders and R. D. Tangerman, Nucl. Phys. B **461** (1996) 197 [Erratum-ibid. B **484** (1997) 538]

[25] J. C. Collins and D. E. Soper, Nucl. Phys. B **194** (1982) 445 .

[26] A. Bacchetta, M. Diehl, K. Goeke, A. Metz, P. J. Mulders and M. Schlegel, JHEP **0702** (2007) 093

[27] J. C. Collins, Nucl. Phys. B **396** (1993) 161

[28] A. V. Efremov, L. Mankiewicz and N. A. Tornqvist, Phys. Lett. B **284** (1992) 394 .

[29] X. Artru and J. C. Collins, Z. Phys. C **69** (1996) 277

[30] X. Artru, arXiv:hep-ph/0207309.

[31] A. Bianconi, S. Boffi, R. Jakob and M. Radici, Phys. Rev. D **62** (2000) 034008

[32] M. Anselmino, M. Boglione, U. D'Alesio, E. Leader and F. Murgia, Phys. Lett. B **509** (2001) 246

[33] J. L. Cortes, B. Pire and J. P. Ralston, Z. Phys. C **55** (1992) 409.

[34] R. L. Jaffe and X. D. Ji, Phys. Rev. Lett. **67** (1991) 552.

[35] V. Barone *et al.* [PAX Collaboration], arXiv:hep-ex/0505054.

[36] V. Abazov *et al.* [ASSIA Collaboration], arXiv:hep-ex/0507077.

[37] X. M. Feng and B. W. Zhang, Chin. Phys. C **35** (2011) 829.

[38] C. Perkins, arXiv:1109.0650 [nucl-ex].

[39] M. Radici, "Phenomenology of TMD's", Ferrara International School Niccolò Cabeo, 2010.

[40] R. Seidl *et al.* [Belle Collaboration], Phys. Rev. D **78** (2008) 032011

[41] R. L. Jaffe, X. m. Jin and J. Tang, Phys. Rev. Lett. **80** (1998) 1166

[42] A. Bacchetta and M. Radici, Phys. Rev. D **67** (2003) 094002

[43] A. Bacchetta and M. Radici, Phys. Rev. D **74** (2006) 114007

[44] A. Bacchetta, F. A. Ceccopieri, A. Mukherjee and M. Radici, Phys. Rev. D **79** (2009) 034029

[45] X. Artru, arXiv:hep-ph/9310323.

[46] X. Artru, J. Czyzewski and H. Yabuki, Z. Phys. C **73** (1997) 527

[47] X. Artru, arXiv:1001.1061 [hep-ph].

[48] A. Airapetian *et al.* [HERMES Collaboration], Phys. Rev. Lett. **94** (2005) 012002

[49] A. Airapetian *et al.* [HERMES Collaboration], Phys. Lett. B **693** (2010) 11

[50] V. Y. Alexakhin *et al.* [COMPASS Collaboration], Phys. Rev. Lett. **94** (2005) 202002

[51] E. S. Ageev *et al.* [COMPASS Collaboration], Nucl. Phys. B **765** (2007) 31

[52] M. Alekseev *et al.* [COMPASS Collaboration], Phys. Lett. B **673** (2009) 127

[53] M. Anselmino, M. Boglione, U. D'Alesio, A. Kotzinian, F. Murgia, A. Prokudin and C. Turk, Phys. Rev. D **75** (2007) 054032

[54] A. V. Efremov, K. Goeke and P. Schweitzer, Phys. Rev. D **73** (2006) 094025

[55] W. Vogelsang and F. Yuan, Phys. Rev. D **72**, 054028 (2005)

[56] J. Soffer, Phys. Rev. Lett. **74** (1995) 1292

[57] M. G. Alekseev *et al.* [COMPASS Collaboration], Phys. Lett. B **692** (2010) 240

[58] F. Bradamante [COMPASS Collaboration], arXiv:1111.0869 [hep-ex].

[59] X. Qian *et al.* [The Jefferson Lab Hall A Collaboration], Phys. Rev. Lett. **107** (2011) 072003

[60] A. Airapetian *et al.* [HERMES Collaboration], JHEP **0806** (2008) 017

[61] A. Bacchetta, A. Courtoy and M. Radici, Phys. Rev. Lett. **107** (2011) 012001

[62] F. Massmann, Eur. Phys. J. ST **162** (2008) 85.

[63] H. Wollny, DIS2009, Conf. Proc. (2009)

[64] A. Vossen *et al.* [Belle Collaboration], Phys. Rev. Lett. **107** (2011) 072004

[65] G. Baum *et al.* [COMPASS Collaboration], "COMPASS: A Proposal for a Common Muon and Proton Apparatus for Structure and Spectroscopy,"

[66] P. Abbon *et al.* [COMPASS Collaboration], Nucl. Instrum. Meth. A **577** (2007) 455

[67] A. Abragam, The Principles of Nuclear Magnetism, The Clarendon Press, Oxford,1961.

[68] J. Kyynaeraeinen, Nucl. Instrum. Meth. A **356** (1995) 47.

[69] E. Albrecht *et al.*, Nucl. Instrum. Meth. A **504** (2003) 354.

[70] E. Albrecht *et al.*, Nucl. Instrum. Meth. A **502** (2003) 266.

[71] E. Albrecht *et al.*, Nucl. Instrum. Meth. A **502** (2003) 236.

[72] http//coral.web.cern.ch/coral/.

[73] R. Brun and F. Rademakers, Nucl. Instrum. Meth. A **389** (1997) 81. web site http://root.cern.ch

[74] http//ges.web.cern.ch/ges/phast/.

[75] P. Abbon *et al.*, Nucl. Instrum. Meth. A **631** (2011) 26.

[76] T. Ypsilantis and J. Seguinot, Nucl. Instrum. Meth. A **343** (1994) 30.

[77] R. J. Barlow, Nucl. Instrum. Meth. A **297** (1990) 496.

[78] F. Sozzi, Measurement of transverse spin effects in COMPASS, PhD. thesis, Trieste University (2007)

[79] G. Pesaro, Measurement at COMPASS of transverse spin effects on identified hadrons on a transversely polarised proton target, PhD. thesis, Trieste University (2010)

[80] A. Martin, G.Pesaro, P. Schiavon, F. Sozzi, H. Wollny, On the role of the acceptance in the unbinned likelihood method, Tech. Rep. COMPASS-2009-13 (2009)

[81] C. Braun New measurement of transverse-spin asymmetries in two-hadron inclusive production, Transversity 2011: Third International Workshop on "Transverse polarization phenomena in Hard scattering", Veli Lošinj, Croatia

[82] C. Elia Measurement of two-hadron asymmetries at COMPASS, DSPIN-2011 : XIV Workshop on "High energy spin physics", Dubna , Russia

[83] S. M. Aybat, A. Prokudin and T. C. Rogers, arXiv:1112.4423 [hep-ph].

[84] A. Bianconi, S. Boffi, R. Jakob and M. Radici, Phys. Rev. D **62** (2000) 034009

[85] B.-Q. Ma , V. Barone,J. S. Huang and Y. Huang, Phys. Rev. **D77** (2008) 014035.

[86] A.Bacchetta, M.Radici, private comunication.

[87] M. Radici Review talk on models for unpolarized and polarized FFs, Transversity 2011 : Third International Workshop on "Transverse polarization phenomena in Hard scattering", Veli Lošinj, Croatia

[88] A. D. Martin, W. J. Stirling, R. S. Thorne and G. Watt, Eur. Phys. J. C 63 (2009) 189-285

RINGRAZIAMENTI

Desidero ringraziare la professoressa Anna Martin che ha rappresentato in questi anni un solido punto di riferimento ed una inesauribile fonte di conoscenza; il professor Franco Bradamante che ha coordinato con saggezza e autoriá, ma allo stesso tempo con grande cordialitá, tutta la fase di presa dati ed analisi dei dati 2010, oggetto di questa tesi; Andrea Bressan, per la sua capacitá di rispondere con umiltá e disponibilitá ad ogni richiesta.

Rivolgo un grande ringraziamento al professore Paolo Schiavon, al professore Marcello Giorgi ed alla professoressa Silvia Dalla Torre per il sostegno incondizionato ed i preziosi consigli di cui mi hanno onorato.

Ringrazio Christopher Braun e Christoph Adolph con i quali é stato un piacere confrontarsi ottenendo, alla fine, sempre una assoluta convergenza di opinioni e di risultati.

Ringrazio Barbara Pasquini e Patrizia Rossi per i commenti ed i suggerimenti che hanno perfezionato il lavoro di tesi. A loro rivolgo un grande ringraziamento per il tempo dedicatomi nonostante gli impegni lavorativi.

Un grazie di cuore ad Alessandro Bacchetta e Marco Radici, che hanno contribuito, con i loro lavori, a chiarire il "senso" delle misure fatte ed hanno dato strumenti essenziali per la fase conclusiva del mio lavoro di dottorato.

Un saluto particolare va agli scienziati della stanza 216. A loro devo innanzitutto dire "grazie" per avermi accolto ed aver chiarito gli innumerevoli dubbi che agli inizi (e non solo) del dottorato erano il mio, ma soprattutto il loro incubo peggiore. Ringrazio Federica per avermi sostenuto come nessun altro nei momenti difficili, un suo sorriso ha spesso significato piú di mille parole; ringrazio Vinicio che, come in una lunga milonga, ha guidato me, ballerino piú che inesperto, nel mondo della programmazione, se oggi ho prodotto qualche migliaio di righe di codice lo devo soprattutto alla sua infinita pazienza; ringrazio la saggia Giulia per aver trovato la soluzione di problemi irrisolvibile per chiunque altro, ha rappresentato una inesauribile fonte di conoscenza, ma soprattutto una splendida compagna di viaggio; ringrazio Giulio che mi ha sempre supportato, non solo su argomentazioni scientifiche, ma anche su tutto l' iter burocratico necessario per il conseguimento del "titolo"; con gli incredibili racconti del maestro di "sudoku" ha colorito i caffé pomeridiani; ringrazio Stafano, insostituibile compagno di lunghe trasferte al CERN. Un saluto va ad Andrea e Luisa, splendide persone a cui un destino beffardo ha dato in sposi due fisici.

Un doveroso saluto va a "quelli dell'aperitivo" Antonella, Stefania e Giampaolo, che hanno reso piú gradevole la mia trasferta triestina.

Infine ringrazio la cittá di Trieste che con il suo mare, i suo profumi ed i suoi splendidi vicoli ha reso piú sopportabile la lontananza da casa.